

This item was submitted to [Loughborough's Research Repository](#) by the author.  
Items in Figshare are protected by copyright, with all rights reserved, unless otherwise indicated.

## Synchronverter-based control for wind power

PLEASE CITE THE PUBLISHED VERSION

PUBLISHER

© Zhenyu Ma

LICENCE

CC BY-NC-ND 4.0

REPOSITORY RECORD

Ma, Zhenyu. 2012. "Synchronverter-based Control for Wind Power". figshare.  
<https://hdl.handle.net/2134/10866>.

This item was submitted to Loughborough University as a PhD thesis by the author and is made available in the Institutional Repository (<https://dspace.lboro.ac.uk/>) under the following Creative Commons Licence conditions.



For the full text of this licence, please go to:  
<http://creativecommons.org/licenses/by-nc-nd/2.5/>

# **Synchronverter-based Control for Wind Power**

by

Zhenyu Ma

A Doctoral thesis

submitted in partial fulfilment of the requirements for the award of

Doctor of Philosophy

of Loughborough University

July 2012

© by Zhenyu Ma 2012

## Abstract

More and more attention has been paid to the energy crisis due to the increasing energy demand from industrial and commercial applications. The utilisation of wind power, which is considered as one of the most promising renewable energy sources, has grown rapidly in the last three decades. In recent years, many power converter techniques have been developed to integrate wind power with the electrical grid. The use of power electronic converters allows for variable speed operation of wind turbines, and enhanced power extraction. This work, which is supported by EPSRC (Engineering and Physical Sciences Research Council) and Nheolis under the DHPA (Dorothy Hodgkin Postgraduate Awards) scheme, focuses on the design and analysis of control systems for wind power.

In this work, two of the most popular AC-DC-AC topologies with PMSG (Permanent Magnet Synchronous Generators) have been developed. One consists of an uncontrollable rectifier, a boost converter and an inverter and a current control scheme is proposed to achieve the MPPT (Maximum Power Point Tracking). In the control strategy, the output current of the uncontrollable rectifier is controlled by a boost converter according to the current reference, which is determined by a climbing algorithm, to achieve MPPT. The synchronverter technology has been applied to control the inverter for the grid-connection. An experimental setup based on DSP (Digital Signal Processing) has been designed to implement all the above mentioned experiments. In addition, a synchronverter-based parallel control strategy, which consists of a frequency droop loop and a voltage droop loop to achieve accurate sharing of real power and reactive power respectively, has been further studied. Moreover, a control strategy based on the synchronverter has been presented to force the inverter to have capacitive output impedance, so that the quality of the output voltage is improved.

The other topology consists of a full-scale back-to-back converter, of which the rectifier is controllable. Two control strategies have been proposed to operate a three-phase rectifier to mimic a synchronous motor, following the idea of synchronverters to operate inverters to mimic synchronous generators. In the proposed schemes, the real power extracted from the source and the output voltage are the control variables, respectively, hence they can be employed in different applications. Furthermore, improved control strategies are proposed to self-synchronise with the grid. This does not only improve the performance of the system but also considerably reduces the complexity of

the overall controller. All experiments have been implemented on a test rig based on dSPACE to demonstrate the excellent performance of the proposed control strategies with unity power factor, sinusoidal currents and good dynamics. Finally, an original control strategy based on the synchronverter technology has been proposed for back-to-back converters in wind power applications to make the whole system behave as a generator-motor-generator system.

## Acknowledgements

This work has been carried out at the Department of Aeronautical and Automotive Engineering at Loughborough University and the Department of Electrical Engineering and Electronics at the University of Liverpool. The financial support provided by the Engineering and Physical Sciences Research Council (EPSRC) and the company Nheolis under the Dorothy Hodgkin Postgraduate Awards (DHPA) scheme is gratefully acknowledged.

I would like to express my deep gratitude to Prof. Qing-Chang Zhong and Prof. Wen-Hua Chen for their supervision, valuable discussions and never-ending encouragement, patience and support. This work would not be what it is without their help.

Moreover, I would like to thank Dr. Tomas Hornik for his help in this project, in particular, on building up the experimental setup. I would also like to thank visiting scholars and my fellow PhD students: Prof. Fan, Dr. Wang, Dr. Zhang, Dr. Cao, Long, Shamsul, Max and Olivia for help and discussions regarding my project. And many thanks to all my colleagues and the staff at the Department of Aeronautical and Automotive Engineering for the good working atmosphere.

Finally, I would like to thank my family for their support and encouragement throughout my PhD.

# Contents

<b>1</b>	<b>Introduction</b>	<b>1</b>
1.1	Motivation . . . . .	1
1.2	Outline of the Thesis . . . . .	2
1.3	Major Contributions . . . . .	3
1.3.1	Current control for maximum power point tracking . . . . .	3
1.3.2	Rectifier control based on synchronverters . . . . .	3
1.3.3	Synchronverter-based control in wind power . . . . .	4
1.4	List of Publications . . . . .	4
<b>2</b>	<b>Wind Energy Conversion Systems</b>	<b>6</b>
2.1	Wind Turbines . . . . .	7
2.2	Generators . . . . .	10
2.2.1	Squirrel-cage induction generators . . . . .	11
2.2.2	Doubly fed induction generators . . . . .	11
2.2.3	Permanent magnet synchronous generators . . . . .	12
2.3	Power Converter Topologies . . . . .	13
2.4	Control Objectives . . . . .	14
2.4.1	Energy capture . . . . .	16
2.4.2	Mechanical loads . . . . .	17
2.4.3	Power quality . . . . .	18
<b>3</b>	<b>Experimental Setup</b>	<b>19</b>
3.1	Hardware Design . . . . .	19
3.1.1	Power circuits . . . . .	19
3.1.1.1	Semistack IGBT . . . . .	19
3.1.1.2	Boost converter . . . . .	21

3.1.1.3	LCL filter . . . . .	22
3.1.2	Control circuits . . . . .	22
3.1.2.1	Measurement transducers board . . . . .	23
3.1.2.2	Control board . . . . .	24
3.2	Software Environment . . . . .	27
3.2.1	Matlab/Simulink . . . . .	28
3.2.2	Code composer studio . . . . .	28
3.2.3	Communication between host and target . . . . .	28
3.2.3.1	Real time data exchange . . . . .	29
3.2.3.2	Matlab GUI program . . . . .	32
<b>4</b>	<b>Maximum Power Point Tracking</b>	<b>33</b>
4.1	System Configurations . . . . .	34
4.2	MPPT Control Strategy . . . . .	35
4.2.1	Permanent magnet synchronous generator . . . . .	35
4.2.2	Uncontrollable rectifier . . . . .	36
4.3	Simulation Results . . . . .	39
4.3.1	Model of a wind turbine . . . . .	39
4.3.2	Model of a permanent magnet synchronous generator . . . . .	41
4.3.3	Simulation of MPPT . . . . .	43
4.4	Experimental Results . . . . .	44
4.5	Conclusions . . . . .	45
<b>5</b>	<b>Overview of the Synchronverter Technology</b>	<b>47</b>
5.1	Synchronverter Technology . . . . .	49
5.2	Simulation Results . . . . .	52
5.3	Experimental Results . . . . .	53
5.4	Conclusions . . . . .	56
<b>6</b>	<b>Synchronverters in Parallel Operation</b>	<b>57</b>
6.1	Description of the Control Scheme . . . . .	58
6.2	Simulation Results . . . . .	59
6.2.1	With a linear load . . . . .	59
6.2.2	With a nonlinear load . . . . .	61
6.2.3	Master-slave mode with a linear load . . . . .	61



6.2.4	Master-slave mode with a nonlinear load . . . . .	64
6.3	Conclusions . . . . .	65
<b>7</b>	<b>Synchronverters with Capacitive Output Impedances</b>	<b>66</b>
7.1	Capacitive Output Impedances . . . . .	67
7.2	Simulation Results . . . . .	69
7.2.1	The case with $L = 0.6mH$ . . . . .	70
7.2.2	The case with $L = 0.15mH$ . . . . .	70
7.3	Experimental Results . . . . .	72
7.3.1	The case with $L = 0.6mH$ . . . . .	72
7.3.2	The case with $L = 0.15mH$ . . . . .	72
7.4	Conclusions . . . . .	74
<b>8</b>	<b>Synchronverters Operated as Rectifiers</b>	<b>77</b>
8.1	Direct Power Control . . . . .	78
8.2	Modeling of a Synchronous Motor . . . . .	80
8.3	Proposed Strategy . . . . .	83
8.3.1	STA . . . . .	83
8.3.2	Proposed strategy to control power . . . . .	85
8.3.3	Proposed strategy to control the output voltage . . . . .	86
8.3.4	Applications of the two proposed strategies . . . . .	87
8.4	Simulation Results . . . . .	87
8.4.1	DPC . . . . .	88
8.4.2	Regulation of the output voltage . . . . .	89
8.5	Experiment Results . . . . .	90
8.5.1	DPC . . . . .	91
8.5.2	Regulation of the output voltage . . . . .	93
8.6	Conclusions . . . . .	94
<b>9</b>	<b>Synchronverters Operated as Rectifiers without a PLL</b>	<b>95</b>
9.1	Proposed Control Strategies . . . . .	97
9.1.1	Regulation of the output voltage . . . . .	97
9.1.1.1	Uncontrolled mode . . . . .	98
9.1.1.2	PWM-controlled mode . . . . .	99
9.1.2	Regulation of the power . . . . .	99

9.2	Simulation Results . . . . .	100
9.2.1	Regulation of the output voltage . . . . .	101
9.2.2	Regulation of the power . . . . .	103
9.3	Experimental Results . . . . .	104
9.3.1	Regulation of the output voltage . . . . .	104
9.3.2	Regulation of the power . . . . .	106
9.4	Conclusions . . . . .	107
<b>10</b>	<b>Synchronverter-based Back-to-back Converter for Wind Power</b>	<b>109</b>
10.1	Control of the Rotor-side Converter . . . . .	111
10.2	Control of the Grid-side Converter . . . . .	113
10.3	Simulation Results . . . . .	115
10.3.1	Under the normal grid condition . . . . .	116
10.3.1.1	Performance of the rotor-side converter . . . . .	117
10.3.1.2	Performance of the grid-side converter . . . . .	117
10.3.2	Under grid voltage sags . . . . .	118
10.4	Conclusions . . . . .	120
<b>11</b>	<b>Conclusions and Further Work</b>	<b>121</b>
11.1	Conclusions . . . . .	121
11.1.1	Uncontrollable rectifier + boost converter + inverter . . . . .	121
11.1.2	Back-to-back converter . . . . .	122
11.2	Further Work . . . . .	122
<b>A</b>	<b>PCB Layout</b>	<b>139</b>
<b>B</b>	<b>Schematics</b>	<b>142</b>
<b>C</b>	<b>Matlab Code</b>	<b>144</b>

# List of Figures

2.1	Main turbine types. (Grid integration of wind energy conversion systems (second edition), Fig.2.12 Main turbine types, pp.47') . . . . .	8
2.2	Diagram of a typical wind turbine. (Grid integration of wind energy conversion systems (second edition), Figure 2.50 Hydraulic blade pitch-regulation system with positioning cylinder and lever transmission (WKA 60, MAN) pp.85') . . . . .	9
2.3	Power efficiency $C_p$ curves. . . . .	10
2.4	Power converter topologies. . . . .	15
2.5	Mechanical power curves of turbine speed for various wind speeds. . . .	17
3.1	Nheolis's wind turbine. . . . .	20
3.2	Topology of main circuit. . . . .	20
3.3	Semistack IGBT device. . . . .	21
3.4	Boost converter board. . . . .	22
3.5	LCL filter. . . . .	23
3.6	Measurement transducers board. . . . .	24
3.7	Control board. . . . .	26
3.8	Control strategy in Simulink. . . . .	27
3.9	Code Composer Studio's work space. . . . .	29
3.10	RTDX diagram. . . . .	30
3.11	The eZdsp F28335 and the XDS560 emulator. . . . .	30
3.12	GUI for RTDX. . . . .	31
4.1	Topology of the system. . . . .	34
4.2	Equivalent circuit for each phase of PMSG. . . . .	35
4.3	Connection of a diode rectifier to the generator. . . . .	36

4.4	Power versus output current of a rectifier for three different wind speeds.	39
4.5	Control strategy. . . . .	40
4.6	Wind turbine model. . . . .	40
4.7	Simulation results. . . . .	43
4.8	Experimental setup. . . . .	44
4.9	The experimental topology for MPPT. . . . .	45
4.10	Experimental results: for the case with 300rpm (left column) and 150rpm (right column). . . . .	46
5.1	The power part of a synchronverter, modified from [1, Figure 2] . . . . .	49
5.2	The electronic part (controller) of a synchronverter, modified from [1, Figure 3] . . . . .	50
5.3	Structure of an idealized three-phase round-rotor synchronous generator, modified from [1, Figure 1] . . . . .	51
5.4	Simulation results . . . . .	53
5.5	Grid voltage and control signal . . . . .	54
5.6	2.5kW experimental results . . . . .	55
5.7	Error between output voltage and grid voltage . . . . .	56
6.1	Proposed control scheme for parallel operation . . . . .	58
6.2	Simulation results with a linear load . . . . .	60
6.3	Simulation results with a nonlinear load . . . . .	62
6.4	Simulation results in the master-slave mode with a linear load . . . . .	63
6.5	Current of inverter1, inverter2 and load . . . . .	63
6.6	Simulation results in the master-slave mode with a nonlinear load . . . . .	64
6.7	Current of inverter1, inverter2 and load . . . . .	65
7.1	A descriptive circuit of a three-phase inverter. . . . .	67
7.2	Single phase of LC filter. . . . .	67
7.3	Control strategy based on synchronverters. . . . .	68
7.4	Simulation results for the case with $L=0.6$ mH: output voltage, current, and THD of the output voltage. . . . .	71
7.5	Simulation results for the case with $L=0.15$ mH: output voltage, current and THD of the output voltage. . . . .	73
7.6	The experimental setup . . . . .	74

7.7	Experimental results for the case with $L=0.6\text{mH}$ : output voltage, current and THD of the output voltage. . . . .	75
7.8	Experimental results for the case with $L=0.15\text{mH}$ : output voltage, current and THD of the output voltage. . . . .	76
8.1	Representation of three-phase voltage source PWM rectifier. . . . .	78
8.2	Conventional DPC. . . . .	79
8.3	PWM rectifier treated as a virtual synchronous motor. . . . .	81
8.4	Structure of an idealized three-phase round-rotor synchronous motor. . .	82
8.5	The model of a synchronous motor. . . . .	83
8.6	Sinusoid-tracking algorithm. . . . .	85
8.7	Proposed DPC. . . . .	86
8.8	Proposed control strategy to maintain the DC bus voltage. . . . .	86
8.9	Simulation results with the nominal grid frequency. . . . .	88
8.10	Simulation results when maintaining DC bus voltage. . . . .	89
8.11	Experimental topology. . . . .	90
8.12	Experimental setup. . . . .	91
8.13	Experimental results of DPC. . . . .	92
8.14	Experimental results with maintained the DC bus voltage. . . . .	93
9.1	A three-phase PWM-controlled rectifier. . . . .	96
9.2	Control strategy to regulate the output voltage. . . . .	97
9.3	Control strategy to regulate the power. . . . .	100
9.4	Simulation results when regulating the output voltage. . . . .	101
9.5	Grid voltage and control signal. . . . .	102
9.6	Input voltage and current. . . . .	102
9.7	Simulation results when regulating the power. . . . .	104
9.8	Experimental topology. . . . .	105
9.9	Experimental results when regulating the output voltage. . . . .	106
9.10	Experimental results when regulating the power. . . . .	108
10.1	Connection of wind power generation system to the grid through back-to-back converters. . . . .	110
10.2	Control structure for the rotor-side converter. . . . .	112
10.3	Control structure for the grid-side converter. . . . .	113

10.4	Performance of the rotor-side converter. . . . .	116
10.5	Performance of the grid-side converter. . . . .	118
10.6	System responses during grid voltage sags. . . . .	119
A.1	The PCB layout of measurement transducers board . . . . .	140
A.2	The PCB layout of control board . . . . .	141
B.1	Schematics . . . . .	143

# List of Tables

3.1	Semistack specification. . . . .	21
3.2	ADC list. . . . .	25
3.3	ePWM list . . . . .	25
3.4	GPIO list . . . . .	25
4.1	Parameters of the PMSG. . . . .	42
4.2	Parameters of the boost converter. . . . .	43
5.1	The parameters of an inverter. . . . .	52
5.2	The parameters of control strategy. . . . .	52
6.1	The parameters used in the simulation. . . . .	59
7.1	Steady-state performance of the inverter with $L=0.6\text{mH}$ . . . . .	69
7.2	Steady-state performance of the inverter with $L=0.15\text{mH}$ . . . . .	70
8.1	Parameters used in the simulation. . . . .	87
9.1	Parameters of the system for simulations . . . . .	100
9.2	Parameters of the controller. . . . .	101
9.3	Control parameters for regulating the power. . . . .	103
10.1	Parameters of the system. . . . .	114
10.2	Control parameters for the rotor-side converter. . . . .	115
10.3	Control parameters for the grid-side converter. . . . .	115

# Nomenclature

$\beta$	Pitch angle
$\Delta\dot{\theta}$	Difference in angular frequency
$\Delta Q$	Difference of reactive power
$\Delta T$	Difference in the total torque acting on the imaginary rotor
$\Delta v$	Difference of voltage
$\delta$	Phase difference
$\dot{\theta}$	Virtual angular speed
$\dot{\theta}_g$	Grid angular frequency reference
$\dot{\theta}_n$	Nominal angular frequency of the grid
$\dot{\theta}_r$	Angular frequency reference
$\gamma_{\psi L}$	Flux vector position
$\lambda$	Tip-speed ratio
$\lambda_0$	Amplitude of the flux
$\lambda_{opt}$	Optimal value of power coefficient
$\omega$	Rotation speed of the rotor
$\omega^*$	Rated frequency
$\omega_g$	Mechanical angular velocity
$\omega_r$	Angular velocity of the rotor



$\vec{E}$	Electromotive force vector
$\vec{I}_a$	Line current vector
$\vec{V}_g$	Terminal voltage vector
$\Phi$	Flux vector
$\phi$	Field magnetic flux
$\rho$	Density of air
$\theta$	Phase angle
$A$	Area swept by a wind turbine
$C_0$	Virtual capacitor
$C_p$	Power coefficient
$D_{mp}$	Frequency droop coefficient
$D_p$	Frequency drooping coefficient
$D_q$	Voltage droop coefficient
$E$	Electromotive force
$e$	Control signal
$e_a$	Control signal of phase A
$H_p$ and $H_q$	Hysteresis bands
$i$	Current vector
$I^*$	Reference current
$I_a$	Line current of the generator
$I_d$	$d$ axis currents
$I_o$	Output current of an uncontrollable rectifier
$I_q$	$q$ axis currents

$i_r$	Output current of the wind-turbine generator
$i_s$	Virtual current
$J$	Moment of inertia of all the parts rotating with the rotor
$k$	Constant of the generator
$K_i$	Integral gains
$K_p$	Proportional gains
$L$	Self-inductance
$L_d$	$d$ axis inductances
$L_q$	$q$ axis inductances
$M$	Mutual inductance
$m$	Mass of air
$M_{fi}$	Field excitation
$P$	Real power
$p$	Number of pole pairs
$P_m$	Mechanical Power
$P_{ref}$	Real power reference
$P_w$	Wind power
$Q$	Reactive power
$Q_{ref}$	Reactive power reference
$R$	Resistance of the stator windings
$R_s$	Resistance of the stator windings
$S_p$ and $S_q$	Digitised variables
$T_e$	Electromagnetic torque

$T_{me}$	Electromagnetic torque
$T_{mm}$	Mechanical torque
$T_m$	Mechanical torque
$v$	Phase terminal voltages
$v_a$	Grid voltage of phase A
$V_d$	$d$ axis voltages
$V_g$	Terminal voltage
$v_g$	Grid voltage
$V_o$	Output voltage of an uncontrollable rectifier
$V_q$	$q$ axis voltages
$V_{ref}$	Output voltage reference
$v_r$	Output voltage of the wind-turbine generator
$v_w$	Wind speed
$X_s$	Inductance of the stator windings
$Z_o(s)$	Output impedance
ASD	Adjustable Speed Drive
CCS	Code Composer Studio
DFIG	Doubly Fed Induction Generators
DPC	Direct Power Control
DPGS	Distributed Power Generation Systems
DSP	Digital Signal Processor
EMF	ElectroMotive Force
GUI	Graphical User Interface

HCS Hill-Climbing Search  
 HVDC High Voltage Direct Current Transmission  
 IGBT Insulated Gate Bipolar Translator  
 MMI Man-Machine Interface  
 MPPT Maximum Power Point Tracking  
 PCB Printed Circuit Board  
 PLL Phase-Locked Loop  
 PMSG Permanent Magnet Synchronous Generators  
 PSF Power Signal Feedback  
 PWM Pulse-Width Modulation  
 RTDX Real Time Data eXchange  
 SCIG Squirrel-Cage Induction Generators  
 SG Synchronous Generators  
 SM Synchronous Motors  
 STA Sinusoid-Tracking Algorithm  
 STATCOM Static Synchronous Compensator  
 SWT Small Wind Turbines  
 THD Total Harmonic Distortion  
 TSR Tip Speed Ratio  
 UPS Uninterruptible Power Supplies  
 VOC Voltage Oriented Control  
 VSG Virtual Synchronous Generators  
 WECS Wind Energy Conversion System

# Chapter 1

## Introduction

### 1.1 Motivation

Wind power has been regarded as one of the main alternative renewable power sources to fossil fuels. Many countries have set strategic plans to develop technology for utilising wind power and a lot of researchers have shifted into this area. During the last decade, more and more attention has been paid to utilising renewable energy sources to tackle the energy crisis we are facing. Wind power has attracted most of the attention and many countries have launched various initiatives to increase the share of wind power in electricity generation. The UK government has set the 2020 plan, i.e. the share of renewable energy will be increased to 20% by the year 2020. It is believed that wind power will be the largest contributor. The technology for wind power generation is somewhat mature. However, the efficiency is still not high, with a common efficiency of about 40%.

An SME in France, Nheolis, has recently invented and patented a new type of wind turbine, Aero-Turbo-Generator, to improve the efficiency. Nheolis was incorporated in France in early 2006 for commercialising an advanced, innovative technology in wind power generation, with initial applications in the form of SWT. The turbine is a cylindrical, horizontal wind power generator that uses the laws of fluid mechanics. The air passing through the blades gets accelerated and pressurised and hence the turbine can extract much more power than conventional wind turbines. Initial wind-tunnel experiments showed a great improvement in efficiency. Because of the different blade type, the conventional control system for wind turbines needs to be re-designed, in particular,

an appropriate strategy to control the power needs to be investigated and implemented for the new turbine.

## 1.2 Outline of the Thesis

The thesis is organised as follows. In Chapter 2, the concept of WECS is briefly introduced. The classic types of wind turbines, generators and power converter topologies are described. Finally, the control objectives are presented.

In order to carry out experiments with the new type of wind turbine which is donated by Nheolis, an experimental setup has been designed and built. Both hardware design and software design are briefly described in Chapter 3.

In Chapter 4, a simple control method for MPPT in a variable speed wind turbine, which uses a boost converter to control the DC bus current without mechanical sensors, is proposed. The output current of an uncontrollable rectifier will be controlled by a boost converter according to the current reference, which is obtained from a climbing algorithm, to achieve MPPT.

The synchronverter technology is introduced in Chapter 5. Both the power part and the electronic part are described. The real power and the reactive power can be easily controlled by frequency loop and voltage loop, respectively. It is an ideal solution for microgrids or smart grids.

In Chapter 6, a controller based on synchronverters for parallel inverters in stand-alone mode has been proposed. Based on the droop method, the controller avoids the use of communication signals among the units. The control strategy consists of a frequency droop loop and a voltage droop loop, and allows the sharing of the real power and reactive power, respectively.

In Chapter 7, an inductor current feedback is introduced to force the output impedance of synchronverters to be capacitive so that the THD of the inverter output voltage will be decreased. Simulation and experimental results are presented to validate the proposed technique.

Two novel control strategies are proposed to operate a rectifier to mimic a synchronous motor in Chapter 8. One is to directly control the power extracted from the source and the other is to control the output voltage. The reactive power can be easily

controlled to obtain the unity power factor. Control schemes are verified through Matlab simulation. It is implemented on a dSPACE-based digital controller and tested on a prototype.

In Chapter 9, a strategy is proposed to control the output voltage of a three-phase PWM-controlled rectifier, based on the synchronverter technology that operates PWM converters to mimic synchronous machines. Such a PWM-controlled rectifier is able to track the grid frequency and phase so that an extra synchronisation unit, e.g. a PLL, is not needed any more, which considerably reduces the computational burden of the controller.

A control strategy based on the synchronverter technology is proposed for back-to-back PWM converters in Chapter 10. Both converters are run as synchronverters, which are mathematically equivalent to the conventional synchronous generators. The rotor-side converter is responsible for maintaining the DC bus voltage and the grid-side converter is responsible for MPPT. Simulation results show that the proposed method operates properly, even in the situation of grid voltage sags.

Finally, the main conclusions of the thesis are summarised and further research is proposed in Chapter 11.

## **1.3 Major Contributions**

### **1.3.1 Current control for maximum power point tracking**

As is well known, the rotating speed of a generator is proportional to the peak output voltage with constant excitation, meanwhile the torque of the machine is proportional to the peak output current with constant excitation. In this control strategy, the current reference of the input current of the boost converter is determined from the climbing algorithm according to the speed of the generator. The input current of the boost converter will be controlled to follow the current reference by PI control. As a result, the wind turbine can generate the maximum output power in different wind speeds.

### **1.3.2 Rectifier control based on synchronverters**

Two control strategies are proposed to operate a rectifier to mimic a synchronous motor, following the idea of operating inverters to mimic synchronous generators. The controllers have two channels: one for the real power and the other for the reactive

power. The real power is controlled by a frequency control loop, which is implemented by comparing the virtual angular speed  $\dot{\theta}$  with the grid angular frequency reference  $\dot{\theta}_g$ , and adding this difference, multiplied with a gain, to the active mechanical torque  $T_m$ . This loop regulates the virtual angular speed  $\dot{\theta}$  of the synchronous motor and creates the phase angle  $\theta$  for the control signal  $e$ . Meanwhile, the reactive power is regulated by a voltage control loop. This loop regulates the field excitation  $M_{fi}$ , which is proportional to the amplitude of the control signal  $e$ . As a result, the reactive power can be easily controlled to be zero in the steady state so that the unity power factor is obtained. Furthermore, the line currents can be made sinusoidal and good dynamics can be achieved.

Moreover, improved control strategies that are able to self-synchronise with the grid are presented. As a result, an extra synchronisation unit, e.g. a PLL, is no longer needed for three-phase rectifiers. Proposed control schemes can automatically synchronise themselves with the grid before connection and track the grid frequency after connection. It considerably reduces the computational burden of the controller.

### 1.3.3 Synchronverter-based control in wind power

Back-to-back converters are the most popular topologies in wind power applications. Most of the control strategies are mainly based on the vector control approach in the d-q reference frame to control the direct component and quadrature component, respectively. In this work, an original control strategy based on the synchronverter technology, which is to operate a converter to mimic a synchronous machine, is proposed for back-to-back converters in wind power applications. The rotor-side converter is run as a synchronous motor and the grid-side converter is run as a synchronous generator. As a consequence, the whole system behaves as a generator-motor-generator system.

## 1.4 List of Publications

1. Z. Ma. A sensorless control method for maximum power point tracking of wind turbine generators. In proceedings of the 14th European Conference on Power Electronics and Applications (EPE2011). Birmingham, September, 2011.
2. Z. Ma, Q.-C. Zhong and J. Yan. Synchronverter-based control strategies for three-phase PWM rectifiers. In proceedings of the 7th IEEE Conference on Industrial



Electronics and Applications (ICIEA2012), Singapore, July, 2012.

3. Z. Ma and Q.-C. Zhong. Synchronverter-based control strategy for back-to-back converters for wind power applications. In proceedings of the 8th Power Plant and Power System Control Symposium (PPPSC2012), Toulouse, September, 2012.
4. Q.-C. Zhong, Z. Ma and P.-L. Nguyen. PWM -controlled Rectifiers without the Need of an Extra Synchronisation Unit. In proceedings of the 38th Annual Conference of the IEEE Industrial Electronics Society (IECON2012), Montreal, October, 2012.
5. Q.-C. Zhong, Z. Ma and J. Yan. Synchronverter-based control strategies for three-phase PWM rectifiers. submitted to IEEE Trans on Power Electronics.
6. Q.-C. Zhong and Z. Ma. Synchronverter-based control strategy for back-to-back converters for wind power applications. submitted to IEEE transactions on Energy Conversion.
7. Q.-C. Zhong, P.-L. Nguyen and Z. Ma. Self-synchronised Synchronverters, IEEE Trans on Power Electronics, under review.
8. Q.-C. Zhong, G. Weiss, P.-L. Nguyen and Z. Ma. Synchronverters: Operating Power Converters as Synchronous Machines. IEEE Transactions on Industrial Electronics, invited paper.

## Chapter 2

# Wind Energy Conversion Systems

Wind energy has been regarded as an environmentally friendly, logistically feasible and economically responsible alternative energy resource. Many countries have set strategic plans to develop technology for utilising wind power and a lot of researchers have shifted into this area. During the last decade, more and more attention has been paid to utilising renewable energy sources to tackle the energy crisis we are facing. Wind power has attracted most of the attention and many countries have launched various initiatives to increase the share of wind power in electricity generation [2, 3].

Wind energy conversion is a complex process. The blades of a wind turbine rotor extract some of the flow energy from air in motion, convert it into rotational energy, then deliver it via a mechanical drive unit (shafts, clutches and gears) to the rotor of a generator and thence to the stator of the same by mechanical-electrical conversion. The electrical energy from the generator is fed via a system of switching and protection devices, leads and any necessary transformers to the mains, to the end user or to some means of storage or utility power grid. During the past 30 years, wind energy conversion has become a reliable and competitive means for electric power generation. The life span of modern wind turbines is now 20-25 years, which is comparable to many other conventional power generation technologies. The cost of wind power has continued to decline through technological development, increased production level, and the use of larger turbines [4].

The major components of a typical wind energy conversion system include a wind turbine, a generator, interconnection apparatus, and control systems. At the present time and for the near future, generators for wind turbines will be synchronous generators, permanent magnet synchronous generators, and induction generators, including

the squirrel-cage type and wound rotor type. For small to medium power wind turbines, permanent magnet generators and squirrel-cage induction generators are often used because of their reliability and cost advantages. Induction generators, permanent magnet synchronous generators, and wound field synchronous generators are currently used in various high power wind turbines.

Interconnection apparatuses are devices to achieve power control, soft start, and interconnection functions. Very often, power electronic converters are used as such devices. Most modern turbine inverters are forced commutated PWM inverters which provide a fixed voltage and fixed frequency output with a high power quality. Both voltage source voltage controlled inverters and voltage source current controlled inverters have been applied in wind turbines. For certain high power wind turbines, the effective power control can be achieved with double PWM converters, which provide a bidirectional power flow between the turbine generator and the utility grid.

## 2.1 Wind Turbines

A wind turbine is a device that captures the kinetic energy of wind. Historically, a wind turbine was frequently used as a mechanical device with a number of blades to drive machinery. Nowadays, it is often used to drive a generator so that the kinetic energy is converted to electricity. The main types of wind turbines are shown in Figure 2.1 [5]. Most modern wind turbines use a horizontal axis configuration with two or three blades, operating either downwind or upwind [6]. The typical structure of a horizontal axis wind turbine is shown in Fig 2.2. The major components include blades, a rotor hub, drivetrain (bearing and gears etc), a generator and the associated control system.

Wind turbines can be used for stand-alone applications, or they can be connected to a utility power grid, or even combined with a photovoltaic system, batteries, and diesel generators, called hybrid systems. Stand-alone turbines are typically used for water pumping or communications. However, homeowners and farmers in windy areas can also use turbines to generate electricity. For utility-scale sources of wind energy, a large number of turbines are usually built close together to form a wind farm.

Assume that the wind speed is  $v_w$  m/s and the area swept by a wind turbine is  $A$  m<sup>2</sup>. Then the volume of air swept through in unit time is  $Av_w$ . If the density of air is  $\rho$  kg/m<sup>3</sup>, then the mass of air  $m$  passing through the area in unit time is  $\rho Av_w$  kg. The

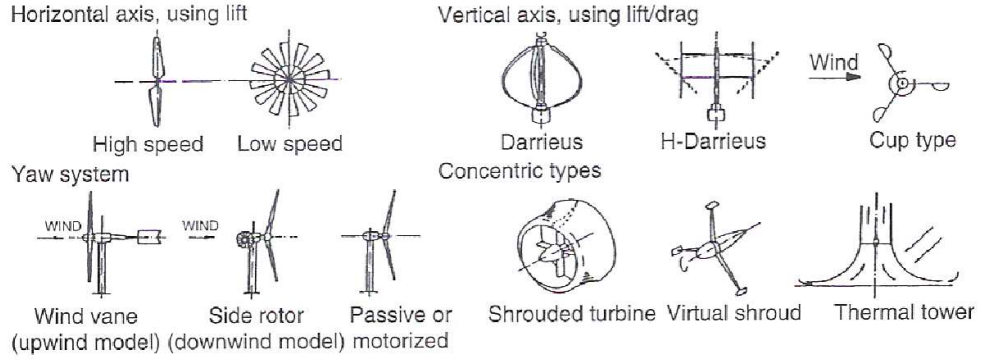


Figure 2.1: Main turbine types. (Grid integration of wind energy conversion systems (second edition), Fig.2.12 Main turbine types, pp.47')

kinetic energy of this mass of air moving at velocity  $v_w$  in unit time is

$$\frac{1}{2}mv_w^2 = \frac{1}{2}\rho Av_w^3.$$

This is actually the same as the power carried by the wind motion. For a wind turbine with rotor blades of  $R$  m long, the area swept is  $A = \pi R^2$  and hence the wind power available is

$$P_w = \frac{1}{2}\rho\pi R^2 v_w^3.$$

In reality, it is impossible to convert all the energy into electricity. The actual power produced by a wind turbine can be calculated as

$$P_m = 0.5\pi\rho C_p(\lambda, \beta) R^2 v_w^3, \quad (2.1)$$

where  $C_p(\lambda, \beta)$  is the power coefficient dependent on the turbine design, the pitch angle  $\beta$  and the tip-speed ratio  $\lambda$  defined as

$$\lambda = \omega_r R / v_w, \quad (2.2)$$

where  $\omega_r$  is the angular speed of the wind turbine. The tip-speed ratio plays a vital role in extracting power from wind. If the rotor turns too slowly, most of the wind passes through the gap between the rotor blades without doing any work; if the rotor turns too quickly, the blurring blades blocks the wind like a solid wall. Therefore, wind turbines are designed to run at optimal tip-speed ratios so that as much power as possible can be extracted from the wind.

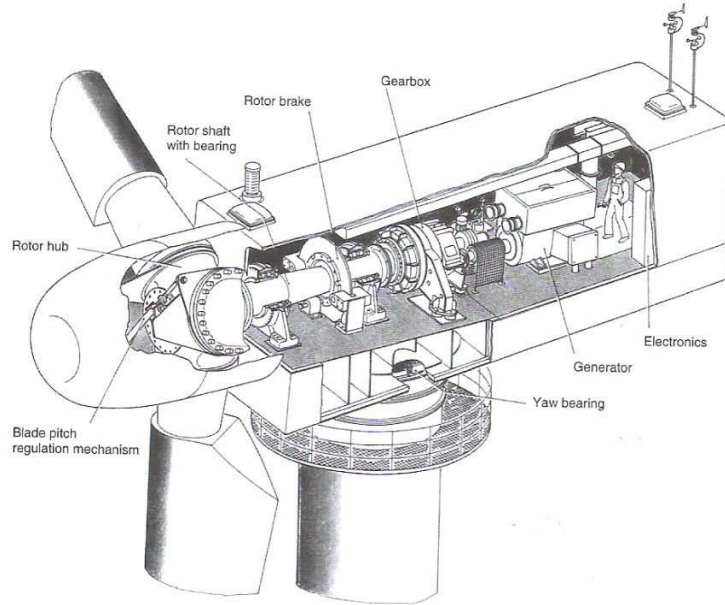
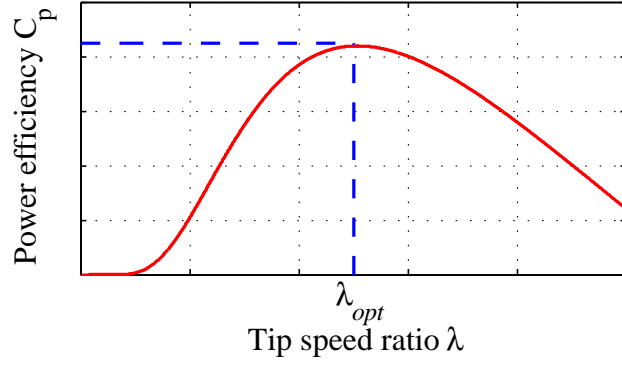


Figure 2.2: Diagram of a typical wind turbine. (Grid integration of wind energy conversion systems (second edition), Figure 2.50 Hydraulic blade pitch-regulation system with positioning cylinder and lever transmission (WKA 60, MAN) pp.85')

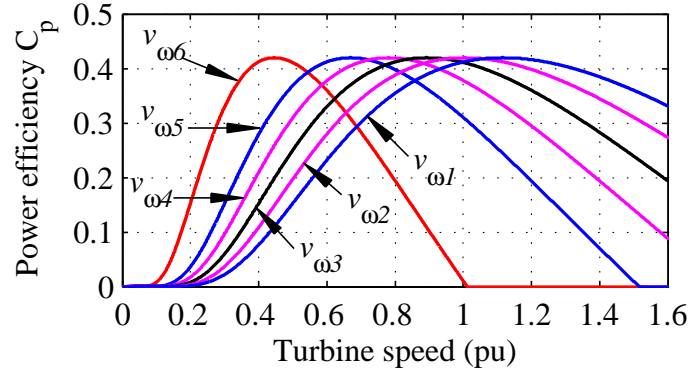
In Equation 2.1,  $C_p$  is a highly nonlinear power function of  $\lambda$  and  $\beta$ . Normally, the pitch has a fixed angular position on the hub of the wind turbine. As a result, the pitch angle is constant. With a fixed  $\beta$ , the relationship between power efficiency  $C_p$  and the tip speed ratio  $\lambda$  can be depicted as shown in Figure 2.3(a). At the point  $\lambda_{opt}$ , the power efficiency will reach its maximum point. Moreover, based on Equation 2.2, the curves of  $C_p$  against various wind speeds should have similar shapes but vary in specific values as indicated in Figure 2.3(b), in which six curves of  $C_p$  are shown according to different wind speeds  $v_{w1}$ ,  $v_{w2}$ ,  $v_{w3}$ ,  $v_{w4}$ ,  $v_{w5}$ , and  $v_{w6}$ . Therefore, the operation points of the wind turbine for various wind speeds are different, which are determined by the point  $\lambda_{opt}$ , see more details in [5]. It is worth noting that the power coefficient  $C_p$  of a wind turbine is limited by  $\frac{16}{27} \approx 0.593$ , according to the Betz law<sup>1</sup>.

A wind turbine can be designed for a fixed-speed or variable-speed operation. Variable-speed wind turbines can produce 8% to 15% more energy output as compared to their fixed-speed counterparts; however, they necessitate power electronic converters to provide a fixed frequency and fixed voltage power to their loads. Most turbine manufacturers have opted for reduction gears between the low speed turbine rotor and the high

<sup>1</sup>[http://en.wikipedia.org/wiki/Betz%27\\_law](http://en.wikipedia.org/wiki/Betz%27_law)



(a)  $C_p$  as a function of tip speed ratio  $\lambda$ .



(b)  $C_p$  as a function of turbine speed for various wind speeds.

Figure 2.3: Power coefficient  $C_p$  curves.

speed three-phase generators. Direct drive configuration, where a generator is coupled to the rotor of a wind turbine directly, offers high reliability, low maintenance, and possibly low cost for certain turbines.

## 2.2 Generators

In electricity generation, an electric generator is a device that converts mechanical energy to electrical energy. A generator forces electric charge to flow through an external electrical circuit. The fixed-speed wind turbines were mostly manufactured with a squirrel-cage induction generator (SCIG) and a multiple-stage gearbox during the 1980's and 1990's. Since the late 1990's, most wind turbines, whose power level was increased above 1.5MW, have been changed to the variable-speed control because of the grid requirement for good power quality. Generator systems of variable speed wind turbines

mostly consist of a doubly-fed induction generator (DFIG), a multiple-stage gearbox and a power electronic converter. Since 1991, permanent magnet synchronous generators (PMSG) have been built to reduce failures in the gearbox and to lower maintenance problems [7].

### **2.2.1 Squirrel-cage induction generators**

An SCIG is a device that converts the mechanical energy of rotation into electricity based on electromagnetic induction. An electric voltage (electromotive force) is induced in a conducting loop (or coil) when there is a change in the number of magnetic field lines (or magnetic flux) passing through the loop. When the loop is closed by connecting the ends through an external load, the induced voltage will cause an electric current to flow through the loop and load. Thus rotational energy is converted into electrical energy. In general, the pole pair number is mostly equal to 2 or 3 in this type of commercial fixed-speed wind turbine with SCIG, so that the synchronous speed in a 50Hz-grid is equal to 1000 or 1500rpm. Therefore, a three-stage gearbox in the drive train is usually required[7].

The advantages of SCIG are well-known and it is a robust technology; it is easy and relatively cheap mass production of the generator. In addition, there is no electrical connection between stator and rotor system. Furthermore, it enables stall regulated machines to operate at a fixed speed when it is connected to a large grid which provides a stable control frequency, which is the most common type of generator used for the grid connected wind turbines.

However, the SCIG has its own disadvantages. First of all, the speed is not controllable, and is variable only over a very narrow range. Secondly, a three-stage gearbox in the drive train is necessary. Gearboxes represent a large mass in the nacelle, and also a large fraction of the investment costs. They are relatively maintenance intensive and a possible source of failures. Moreover, it is necessary to obtain the excitation current from the stator terminals. This makes it impossible to support grid voltage control[4].

### **2.2.2 Doubly fed induction generators**

The fact that the rotor circuit of a SCIG is not accessible can be changed if the rotor circuit is wound and made accessible via slip rings, which offers the possibility of controlling the rotor circuit so that the operational speed range of the generator can

be increased in a controlled manner. The rotor circuit is often connected to back-to-back power electronic converters, which consists of a rotor-side converter and a grid-side converter sharing the same DC bus, so that the difference between the mechanical frequency and the electrical frequency can be compensated via injecting a current with a variable frequency into the rotor circuit. Hence, the operation during both normal and faulty conditions can be regulated via controlling the converters.

A DFIG can be excited by the rotor windings and does not have to be excited by the stator windings. If needed, the reactive power needed for the excitation from the stator windings can be generated by the grid-side converter. As a result, a wind power plant equipped with DFIGs can easily take part in the regulation of voltage. The stator always feeds real power to the grid but the real power in the rotor circuit can flow bidirectionally, from the grid to the rotor or from the rotor to the grid, depending on the operational condition. Ignoring the losses, the power handled by the rotor circuit is [8]

$$P_{\text{rotor}} = -s \cdot P_{\text{stator}}$$

and the power sent to the grid is

$$P_{\text{grid}} = P_{\text{rotor}} + P_{\text{stator}} = (1 - s)P_{\text{stator}},$$

where  $s$  is the slip. Since most of the power flows through the stator circuit, the power processed by the rotor circuit can be reduced to roughly 30%. This means that the great advantage of a sufficient range of operational speed can be achieved with a reasonably low cost[9].

### 2.2.3 Permanent magnet synchronous generators

A PMSG adopts a permanent magnet to generate the magnetic field needed for electricity generation and hence there is no need to provide an external power supply for excitation or to have a rotor circuit. This simplifies the structure and reduces the maintenance cost. PMSGs are more efficient than inductor generators and the power factor can be unity or even leading. Moreover, PMSGs have very high power density and the price of rare-earth magnets has reduced by more than an order of magnitude in the last 10 years. As a result, PMSGs are becoming increasingly popular for wind power applications. A PMSG runs at the synchronous speed, and the frequency of electricity generated is directly in proportion to the mechanical speed, and hence the slip is zero.



This could be used to eliminate the need for a mechanical sensor to measure the speed of the turbine. Compared to the DFIG this generator system has the following advantages [7]:

1. higher efficiency and energy yield,
2. no additional power supply for the magnet field excitation,
3. higher reliability due to the absence of mechanical components such as slip rings,
4. improvement in the thermal characteristics of the machine due to the absence of the field losses.

However, PMSG has disadvantages and these can be summarised as follows:

1. high cost,
2. difficulty to handle in manufacture,
3. demagnetisation of PM at high temperature.

## **2.3 Power Converter Topologies**

Various wind turbine topologies have been developed and built to maximise energy capture, minimise costs, provide consistent dynamic response, improve power quality, and ensure safety together with the growth of wind energy during last two decades.

The three main types of topologies for wind turbines are as detailed below [10]. The first type is a fixed-speed wind turbine system using a multi-stage gearbox and a standard squirrel-cage induction generator, directly connected to the grid through a transformer as shown in Fig 2.4(a). The rotor blades have a simple construction because the blade is directly fixed on the hub. The rotor blades of this type are adjusted only once when the turbine is erected. The power limitation over the rated wind speed is achieved by the stall effect of the rotor blades. The wind turbine with this topology is completely passive while the wind causes the power regulation by itself. Therefore, this topology is called a passive stall control, or briefly a stall control. In most cases, capacitors are grid-connected parallel to the generator to compensate for the reactive power consumption.

The second type is a variable speed wind turbine system with a multi-stage gearbox and a doubly fed induction generator. The power electronic converter feeding the rotor winding has a power rating of approximately 30% of the rated power; the stator winding of the DFIG is directly connected to the grid as shown in Fig 2.4(b). The stator is constructed in the same way with a SCIG. The rotor is equipped with a three-phase winding and connected to the grid through the power electronic converter. The basic operation principle is the same as a SCIG. However, the rotor active power can be controlled by the current of the rotor side converter. Typically, by controlling the rotor active power flow direction, a speed range  $\pm 30\%$  around the synchronous speed can be obtained. Instead of dissipating the rotor energy, it can be fed into the grid. The choice for the rated power of the rotor converter is a trade-off between costs and the speed range desired. Moreover, this converter performs reactive power compensation and smooth grid connection.

The third type is also a variable speed wind turbine, but it is a gearless wind turbine system with a permanent magnet synchronous generator. It uses a low-speed high-torque synchronous generator and an AC-DC-AC electronic converter for the grid connection as shown in Fig 2.4(c). A full-scale back-to-back converter can be used as AC-DC-AC converter. Another popular AC-DC-AC converter includes an uncontrollable rectifier, a DC-DC converter and an inverter.

## 2.4 Control Objectives

The need for control goes back to the origins of wind turbines. Wind turbines are complex, nonlinear, dynamic systems forced by gravity, stochastic wind disturbances, and gravitational, centrifugal, and gyroscopic loads. The aerodynamic behaviour of wind turbines is nonlinear, unsteady and complex. Designs of control algorithms for wind turbines must account for these complexities. The control strategies of the wind turbine can be classified into four categories, namely [4]:

1. Fixed-speed fixed-pitch: FS-FP is very simple and low-cost. But its performance is rather poor. In fact, no active control action can be done to alleviate mechanical loads and improve power quality. Further, the conversion efficiency is far from optimal.

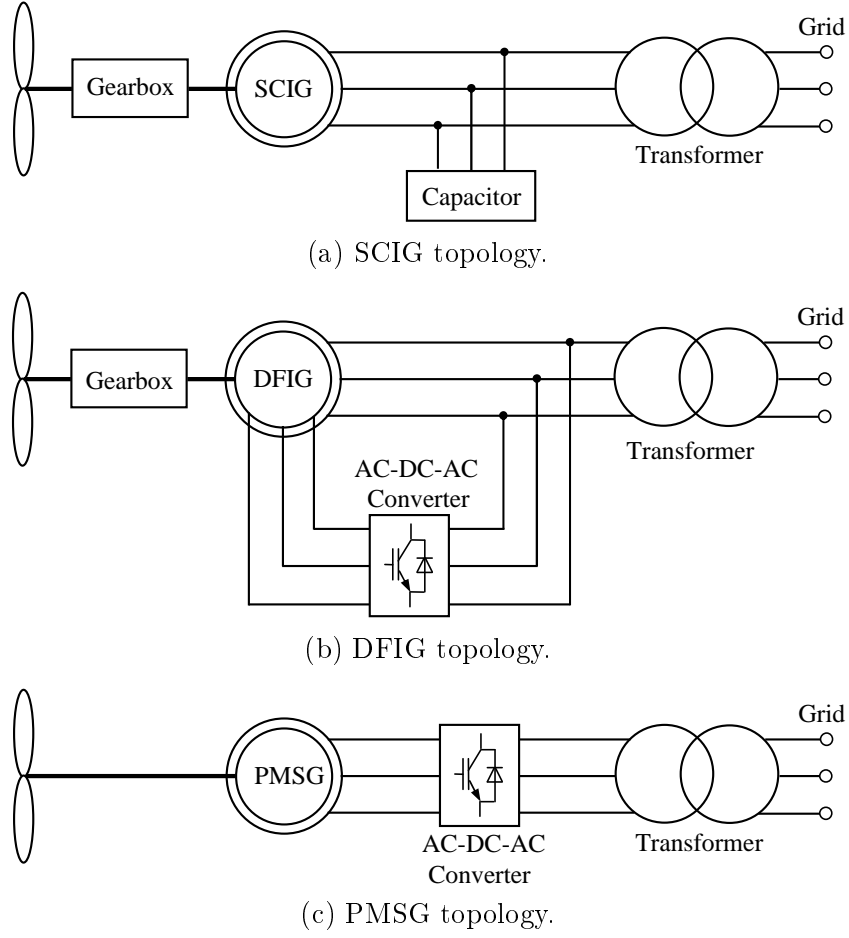


Figure 2.4: Power converter topologies.

2. Fixed-speed variable-pitch: This type can improve the power quality and the conversion efficiency in high wind speeds. The variable-pitch operation enables an efficient power regulation at higher than rated wind speeds.
3. Variable-speed fixed-pitch: This type can improve the power quality and the conversion efficiency in low wind speeds. The variable-speed operation increases the energy capture at low wind speeds.
4. Variable-speed variable-pitch: This control strategy is the best method for the wind turbine system, but it is also the most complicated one. It can improve the power quality and the conversion efficiency in any wind speed.

The main control goals were the limitation of power and speed below some specified values to prevent the turbine from unsafe operation under high wind conditions. Former

wind turbines included primitive mechanical devices to attain these objectives. As wind turbines augmented in size and power, control specifications became more demanding and regulation mechanisms more sophisticated. Increasingly, control systems have been expected not merely to keep the turbine within its safe operating region but also to improve efficiency and quality of power conversion. They gradually evolved as a consequence until playing today a decisive role in modern turbines. These goals can be arranged in the following topics: energy captures, mechanical loads and power quality [11].

### 2.4.1 Energy capture

For a wind turbine, the generation capacity specifies how much power can be extracted from the wind, taking into consideration both physical and economic constraints. Normally, wind generation systems can be divided into variable-speed generation systems and fixed-speed generation systems. Variable-speed generation systems are more attractive compared to fixed-speed ones. This is because the power efficiency  $C_p$  in variable-speed generation systems can be controlled to reach its maximum value and hence the mechanical power of a variable-speed wind turbine is commonly higher than that of a similar fixed-speed wind turbine for various wind speeds [5].

The target maximum power point of a wind turbine system can be written as

$$P_{max} = K_{opt}\omega_{ropt},$$

where

$$K_{opt} = \frac{0.5\pi\rho C_{pmax}R^5}{\lambda_{opt}^3},$$

$$\omega_{opt} = \frac{\lambda_{opt}v_\omega}{R}.$$

Hence, the maximum mechanical power for a certain wind speed can be obtained at a certain wind turbine speed known as the optimum wind turbine speed  $\omega_{opt}$ , which corresponds to a certain optimum tip speed ratio  $\lambda_{opt}$ . In order to extract the maximum power from the wind energy, the turbine should always be operated at  $\lambda_{opt}$  via controlling the turbine speed.

Figure 2.5 shows the turbine mechanical power against turbine speed for various wind speeds. An advanced technique should be applied to extract the maximum power from the wind turbine under all working conditions as indicated in Figure 2.5. Basically,

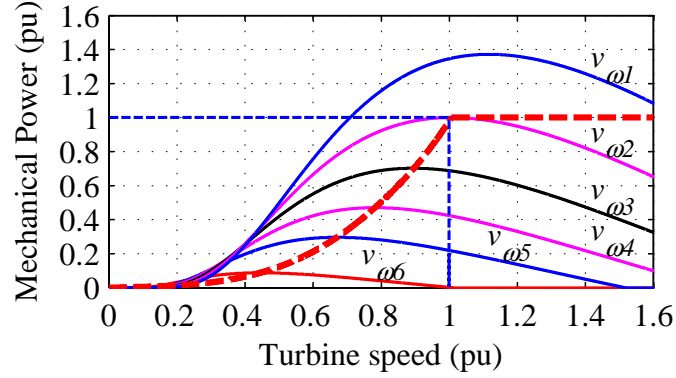


Figure 2.5: Mechanical power curves of turbine speed for various wind speeds.

the MPPT controllers can be classified into three types, e.g. TSR control, PSF control and HCS control. For TSR control, with the knowledge of the relationship between the tip speed ratio and the extracted power, both the wind speed and the turbine speed are measured or estimated to maintain the TSR at an optimum value and then extract the maximum possible power. In PSF control, the power is measured as a feedback to be controlled to reach the turbine's maximum power point. As a result, the power curve of the wind turbine is needed, which can be obtained through simulation or off-line experiments. Different from the previous two methods, in HCS control, the maximum power point is continuously searched depending on the current operating power point and the relationship between the changes in power and speed.

#### 2.4.2 Mechanical loads

Keeping in mind the minimisation of the energy cost, the control system should not be merely designed to track as tightly as possible the ideal power curve. In fact, the other control objectives should not be ignored. For instance, the mechanical loads that wind turbines are exposed to must be considered. Mechanical loads may cause fatigue damage on several devices, thereby reducing the useful life of the system.

There are basically two types of mechanical loads, namely static and dynamic ones [12]. Static loads result from the interaction of the turbine with the mean wind speed. Much more important from the control viewpoint are the dynamic loads, which are induced by the spatial and temporal distribution of the wind speed field over the area swept by the rotor. Dynamic loads comprise variations in the net aerodynamic torque

that propagate down the drive-train, and variations in the aerodynamic loads that impact on the mechanical structure [5].

### **2.4.3 Power quality**

Power quality affects the cost of energy in several ways. For instance, poor power quality may demand additional investments in power lines, or may impose limits to the power supplied to the grid. Because of the long-term and short-term variability of the energy resource and the interaction with the power network, wind generation facilities are conventionally considered as poor quality suppliers. Therefore, the control system design must also take power conditioning into account. This control requirement is more and more relevant as the power scale of wind generation facilities approaches the output rating of conventional power plants. Power quality is mainly assessed by the stability of the frequency and voltage at the point of connection to the grid and by the emission of flicker.

## Chapter 3

# Experimental Setup

In order to carry out real-time experiments with the wind turbine in Figure 3.1, which was donated by Nheolis SAS corporation, an experimental setup has been designed and built. It mainly consists of a power-processing device (including a rectifier, maximum power tracking system, an energy storage system and an inverter) and a braking system to safeguard the operation of the wind turbine. All these are controlled by a central controller eZdspF28335, which is from Texas Instruments. From this figure, the wind turbine has been installed on the roof of the department's building. All components should be placed in a control panel. A remote MMI is placed remotely to monitor the operation of the wind turbine, via communication. The supervisor computer has been set up in the G05 Lab. All components have been designed and made by the PHD researcher except a Semistack IGBT device which purchased from Semikron. In this chapter, the experimental system design and development are briefly described.

### 3.1 Hardware Design

#### 3.1.1 Power circuits

The topology of the main circuits is shown in Figure 3.2. For the wide range of variable speed operation, a DC-DC boost chopper is utilised between a 3-phase diode rectifier and the IGBT inverter.

##### 3.1.1.1 Semistack IGBT

The Semistack IGBT device, which is from Semikron, consists of a three-phase uncontrolled rectifier, some components on the DC bus and a three-phase inverter. The device



Figure 3.1: Nheolis's wind turbine.

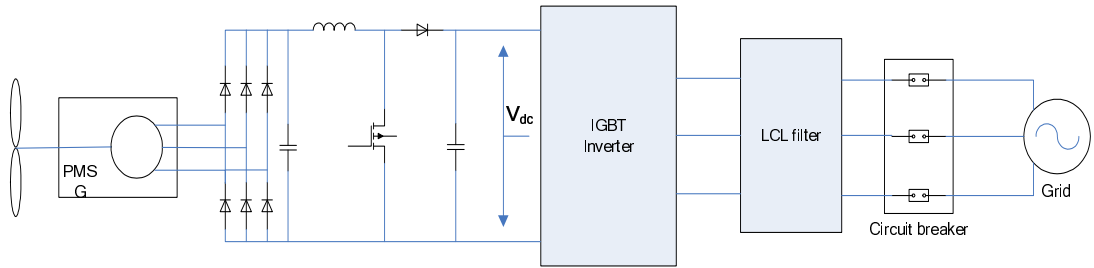


Figure 3.2: Topology of main circuit.

is equipped by IGBT drivers for the boost converter and three phase inverter. Moreover, there are two Hall-effect current sensors to measure the inverter output currents. As the voltage and frequency of the Semistack input can vary, the boost converter is to be utilised to control DC bus current to follow the optimised current reference for maximum power point operation. As an energy storage system is not to be included, the three-phase inverter is to be responsible for grid synchronisation and power flow control by regulating the DC bus voltage.

The Semistack specification is given in Table 3.1. The Semistack IGBT device is shown in Figure 3.3.



Table 3.1: Semistack specification.

Parameters	Values
Maximum rated r.m.s current of a complete AC controller connection	22 A
Rated r.m.s output voltage	380 V
Maximum rated DC bus voltage applied to the capacitor bank	800 V
Maximum collector-emitter DC bus voltage	1200 V
Maximum switching frequency	15 kHz

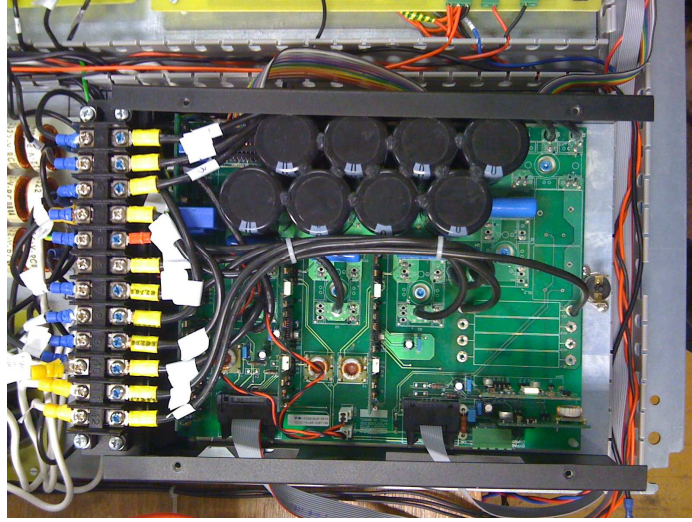


Figure 3.3: Semistack IGBT device.

#### 3.1.1.2 Boost converter

As the inductor for the boost converter and the capacitor bank between the rectifier and the boost converter are not part of the Semikron device, a bank of capacitors has been added (between 4 and 10 pin) behind the three-phase uncontrolled rectifier to smooth the DC bus voltage. A bank of inductors has been added (between 4 and 11 pin) to build a boost converter on the DC bus to satisfy the demand. The boost converter board, which consists of a bank of capacitors required behind the three-phase uncontrolled rectifier, a bank of inductors for the boost converter, and a capacitor charging circuit for the safe operation of the boost converter, is shown in Figure 3.4.

This converter divides the DC bus into two parts: DC bus voltage at the output terminals of the diode rectifier, which is a variable DC bus voltage, and the DC bus voltage at the input terminals of the voltage source inverter, which is fed from a fixed DC bus voltage. The output current of the generator-rectifier system can be controlled

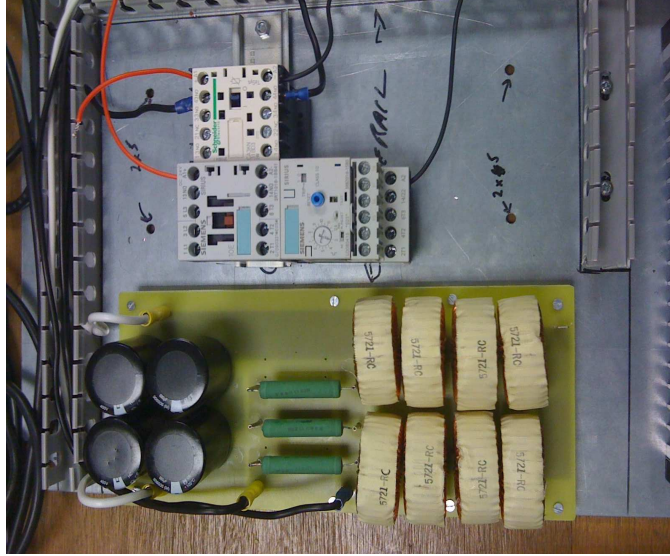


Figure 3.4: Boost converter board.

by changing the duty cycle of the switch. Its purpose is to control the rectifier output current so that the maximum power can be captured from the wind by the turbine.

#### 3.1.1.3 LCL filter

The high-frequency switching of a PWM converter may produce harmonics and inter-harmonics, which are in the range of some kilohertz. Due to the high frequency, the harmonics are relatively easy to remove by small-size filters. The filter board designed for the output of the inverter connects to pins 7,8 and 9. The LCL filter is connected in parallel as an interface between the inverter and the utility grid. The LCL filter board is equipped with a variety of measuring terminals to provide more freedom for control algorithm with different current feedback to be measured. This will allow, if necessary, multiloop control to be implemented, ensuring steady-state reference tracking performance and fast dynamic compensation for system disturbances (including sudden reference or load changes) and improving stability. The LCL filter board is shown in Figure 3.5.

#### 3.1.2 Control circuits

Control circuits include the measurement transducers board and the I/O conditioning board.

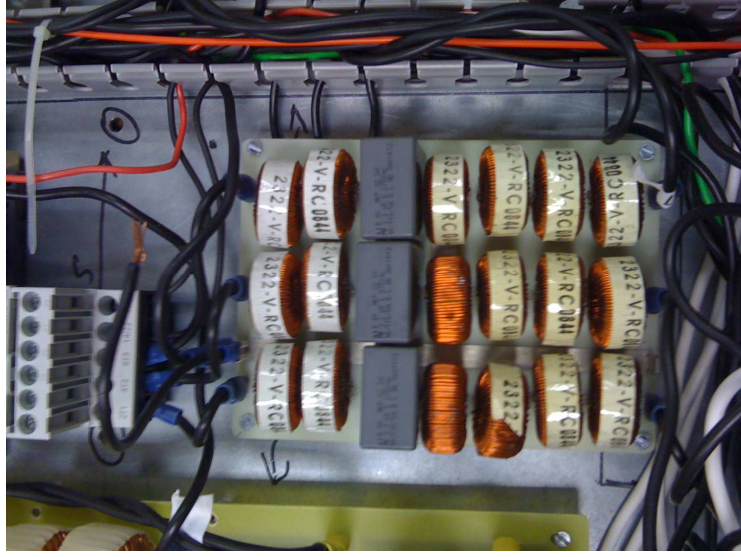


Figure 3.5: LCL filter.

#### 3.1.2.1 Measurement transducers board

The measurement transducers board, as shown in Figure 3.6, consists of 2 current (LA 25-NP) LEM transducers and 10 voltage (LV 25-P) LEM transducers with instantaneous current and voltage output respectively. The PCB layout of the measurement transducers board is given in Appendix A.

For the voltage transducers, the selection of the primary resistor is very important for the circuit design. As we know, the transducer's optimum accuracy is obtained at the nominal primary current. As far as possible, the primary resistor  $R_1$  (see Appendix A) should be calculated so that the nominal voltage to be measured corresponds to a primary current of 10mA.

For example, the measurement range of grid voltage of each phase is 325V. The primary nominal current is 10mA. The primary resistor  $R_1$  should be calculated in Equation 3.1. Moreover, the heat dissipation issues should be taken into account. Therefore, three 100W resistors in parallel have been used for these reasons.

$$R_1 = \frac{V_{grid}}{I_{pn}} = \frac{325}{0.01} = 32.5K\Omega \quad (3.1)$$

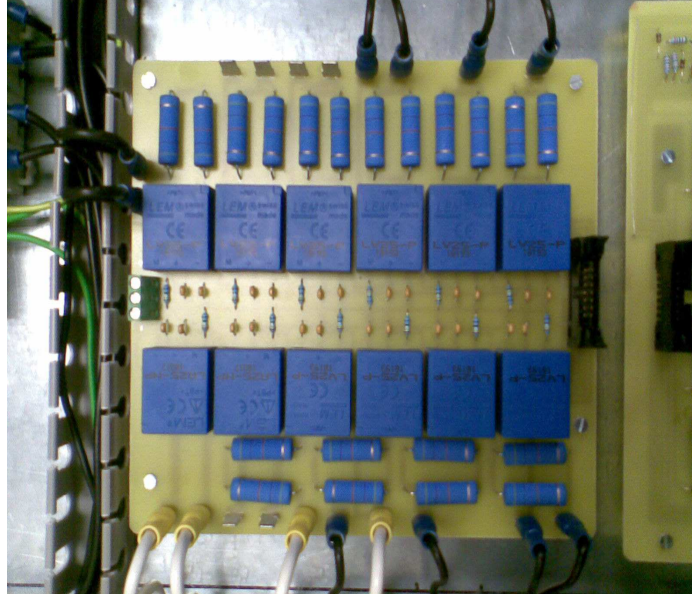


Figure 3.6: Measurement transducers board.

#### 3.1.2.2 Control board

F28335 digital signal controllers include multiple complex peripherals running at fairly high-clock frequencies. They are commonly connected to low-level analog signals using an onboard analog-to-digital converter. The control board has been designed to be employed like an interface between the power circuits and the TI DSP. The digital signal controller TMS320F28335 is a 32-bit floating-point digital signal controller DSP and is fixed on the top of the control board, as shown in Figure 3.7. The operating speed is 150 MHz (30 MHz input clock). The integrated peripherals of the TMS320F28335 device used in this project are shown as follows: 12 input channels with a 12-bit Analog to Digital Converter (ADC), 7 enhanced PWM modules (ePWM) and 4 digital general purpose I/O (GPIO). Table 3.2, 3.3 and 3.4 show the list of ADC, ePWM and GPIO channels.

The ADC module consists of a 12-bit ADC with a built-in sample-and-hold (S/H) circuit and provides a flexible interface to peripherals with a fast conversion rate of up to 80 ns at 25 MHz ADC clock. The ADC module has 16 channels, configurable as two independent 8-channel modules.

The ePWM peripheral performs a digital to analog (DAC) function, where the duty cycle is equivalent to a DAC analog value. The ePWM module represents one

Table 3.2: ADC list.

ADC (Analog Inputs)				
No.	Variable name	Voltage level	Range	Transducer
1	Gen.voltage phase A	$\pm 3\text{Vdc}$	230Vac	LV 25-P
2	Gen.voltage phase B	$\pm 3\text{Vdc}$	230Vac	LV 25-P
3	Gen.voltage phase C	$\pm 3\text{Vdc}$	230Vac	LV 25-P
4	Gen.current phase A	$\pm 3\text{Vdc}$	10A	LA 25-NP
5	Gen.current phase B	$\pm 3\text{Vdc}$	10A	LA 25-NP
6	Gen.current phase C	$\pm 3\text{Vdc}$	10A	LA 25-NP
7	Grid.voltage phase A	$\pm 3\text{Vdc}$	230Vac	LV 25-P
8	Grid.voltage phase B	$\pm 3\text{Vdc}$	230Vac	LV 25-P
9	Grid.voltage phase C	$\pm 3\text{Vdc}$	230Vac	LV 25-P
10	Idc	$\pm 3\text{Vdc}$	10A	LA 25-NP
11	Vdc	$\pm 3\text{Vdc}$	800Vdc	LV 25-P
12	Vin	$\pm 3\text{Vdc}$	400Vdc	LV 25-P

Table 3.3: ePWM list

ePWM			
No.	Variable name	Voltage level	Frequency
1	Inverter leg W-top switch	0/15V	10kHz
2	Inverter leg W-botton switch	0/15V	10kHz
3	Inverter leg U-top switch	0/15V	10kHz
4	Inverter leg U-botton switch	0/15V	10kHz
5	Inverter leg V-top switch	0/15V	10kHz
6	Inverter leg V-botton switch	0/15V	10kHz
7	Boost converter	0/15V	10kHz

Table 3.4: GPIO list

GPIO				
No.	Variable name	Voltage level	I/O	signal
1	Three phase circuit breaker	0/15V	Input	contact
2	Three phase circuit breaker	0/24V	Output	relay
3	Charging relay (Boost converter)	0/15V	Input	contact
4	Charging relay (Boost converter)	0/24V	Output	relay

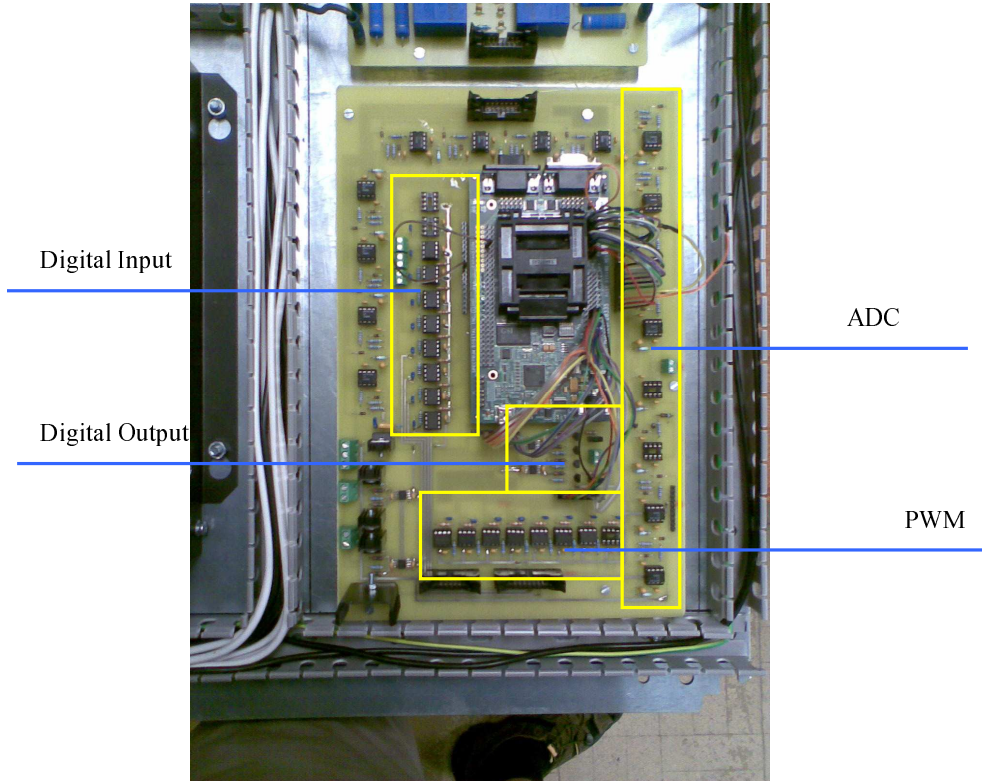


Figure 3.7: Control board.

complete PWM channel composed of two PWM outputs. The ePWM modules are chained together via a clock synchronisation scheme that allows them to operate as a single system when required. In the case of the three-phase inverter, six switching elements can be controlled using three ePWM modules, one for each leg of the inverter. Each leg must switch at the same frequency and all legs must be synchronised.

The GPIO multiplexing (MUX) registers are used to select the operation of shared pins. These pins can be individually selected to operate as digital I/O, referred to as GPIO, or connected to one of up to three peripheral I/O signals. If selected for digital I/O mode, registers are provided to configure the direction of the pin as either input or output.

The control board, which is shown in Figure 3.7, is employed like an interface between the power circuits and the TI DSP. As the TI DSP controller uses 3.3V voltage level signals, the ADC inputs must be adjusted from  $\pm 15V$  and PWM, DI and DO signals must be processed via optocouplers with 3.3V on the controller side and 15V on the opposite (15V CMOS signal are necessary to control the Semikron device). The



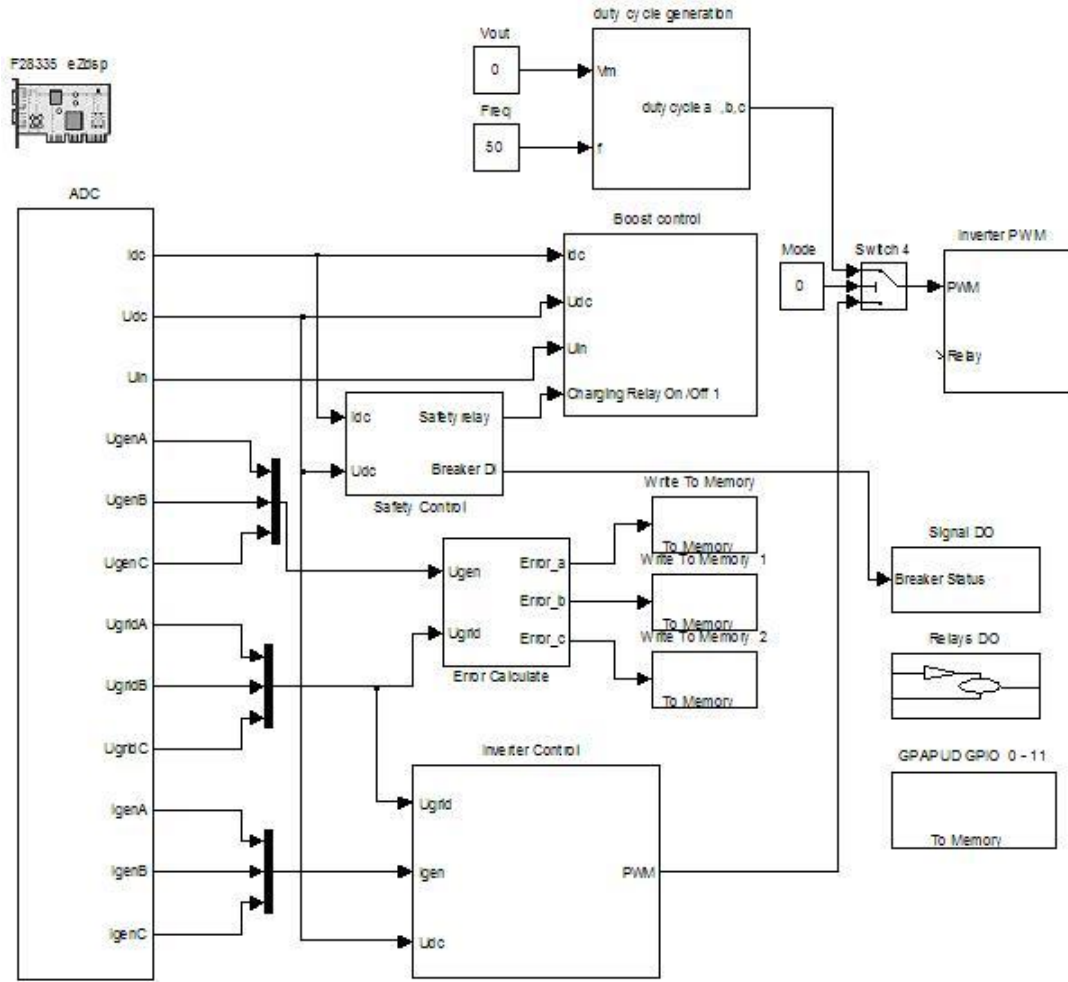


Figure 3.8: Control strategy in Simulink.

PCB layout of the control board is given in Appendix A. Specific schematics of ADC, DI, DO and PWM are shown in Appendix B.

## 3.2 Software Environment

Code Composer Studio v3.3 and Matlab2008a/Simulink have been used for the software design in this project. The Developer's Kit for Texas Instruments DSP unites Matlab, Simulink, and the code generation capabilities of Real-Time Workshop with TI's CCS to provide DSP software/systems architects with a unique suite of tools for every phase of the DSP development cycle. Code Composer Studio has been interfaced with the MATLAB environment through a set of link functions that provide direct communi-

cation between the two applications. The control strategy model has been built in Simulink (see Figure 3.8). The code will be generated automatically in CCS to debug the program.

### **3.2.1 Matlab/Simulink**

Matlab is a powerful and well-known tool for engineers and scientists. The Simulink, integrated with Matlab, is an environment for simulation and model-based design for dynamic and embedded systems. It provides an interactive graphical environment and a set of block libraries that allow design, simulation, implementation, and the ability to test a variety of time-varying systems, including apart from other digital signal processing and controls.

For TMS320F28335 programming, Target Support Package TC2 for Matlab is used. The TC 2 package integrates Matlab and Simulink with TI's eXpressDSP tools (Code Composer Studio). By using the TC2 package, a C-language real-time implementation of the Simulink model is generated and automatically compiled, and then the generated code is downloaded to DSP RAM or flash. Onboard DSP peripherals are directly supported. The Blackhawk USB560 JTAG emulator is used to communicate with the TI DSP.

### **3.2.2 Code composer studio**

Code Composer Studio is the integrated development environment for TI's DSPs, micro-controller and application processors. CCS includes a suite of tools used to develop and debug embedded applications. It includes compilers for each of the TI's device families, a source code editor, a project build environment, a debugger, a profiler, simulators and many other features. Figure 3.9 shows the CCS's work space.

### **3.2.3 Communication between host and target**

The graphical user interface for this project is designed in Matlab software. For the development of this GUI, it was necessary to build RTDX to understand the communication between the controller board and Matlab. This GUI is designed in order to keep a few things in mind, so that the user is able to diagnose and analyse the performance of the system by changing the controller parameters such as the type of controller or



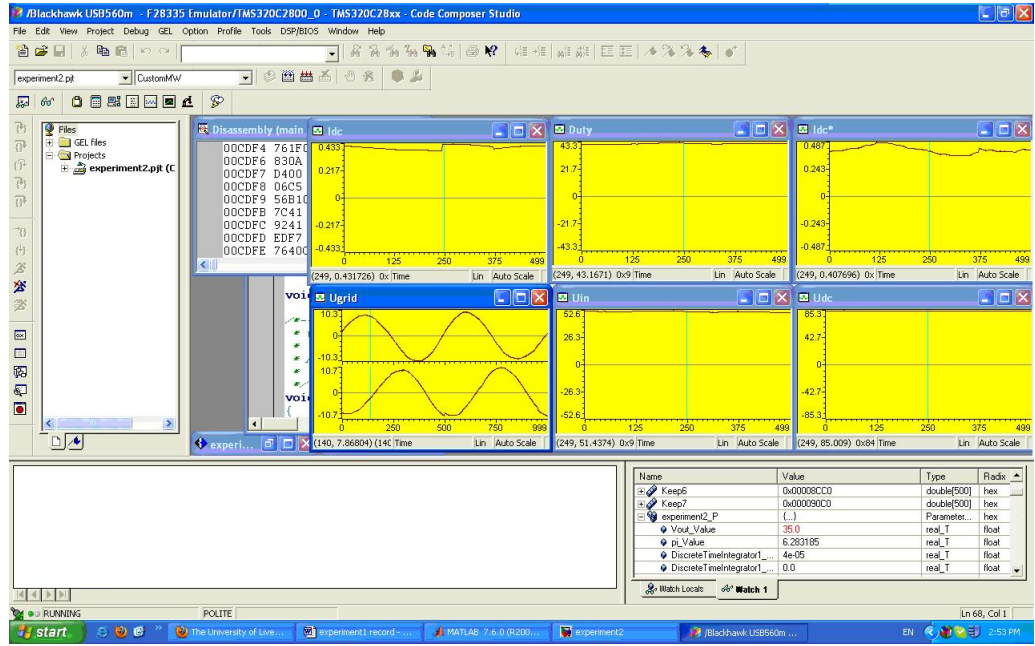


Figure 3.9: Code Composer Studio's work space.

the gains values. First of all, it is very important to understand that RTDX needs to be established between the controller and GUI.

### 3.2.3.1 Real time data exchange

Real time data exchange (RTDX) provides real-time, continuous visibility into the operations of target board applications. RTDX transfers data between a host computer and target devices without interfering with the target application. You may analyse and visualise the data on the host using the COM interface provided by RTDX. Clients such as Visual Basic, Visual C++, Excel, LabView, Matlab, and others may easily use the COM interface. This realistic representation of the system operation may shorten development time. RTDX forms a 2-way data pipe between a target application and a host client via a combination of hardware and software components, as shown in Figure 3.10.

Data can be sent from the target application to the host client and vice versa. We can visualise this pipe as a collection of one or more thinner channels through which the data travels. This tags the data as belonging to a particular channel to distinguish various data. These channels are unidirectional; the data flows from the target application to

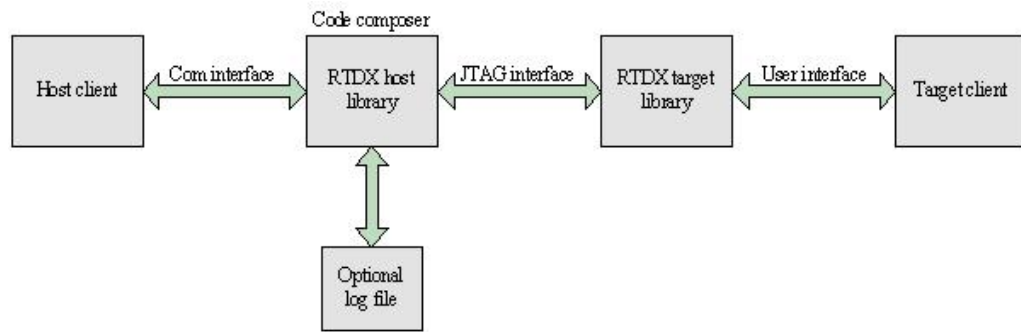


Figure 3.10: RTDX diagram.



Figure 3.11: The eZdsp F28335 and the XDS560 emulator.

the host client and vice-versa. Data can be input into a channel asynchronously at any time.

The target application sends data to the host by calling functions in the RTDX Target Library. These functions immediately buffer the data and then return. The RTDX Target Library then transmits the buffered data to the host without interfering in the target application. The host records the data into either a memory buffer or an RTDX log file, depending on the specified RTDX host-recording mode. The recorded data can be retrieved by any client host application of the RTDX host interface. Windows platform computers provide a COM interface for the RTDX host interface.

Similarly, a host client can send data to the target. The RTDX Host Library buffers

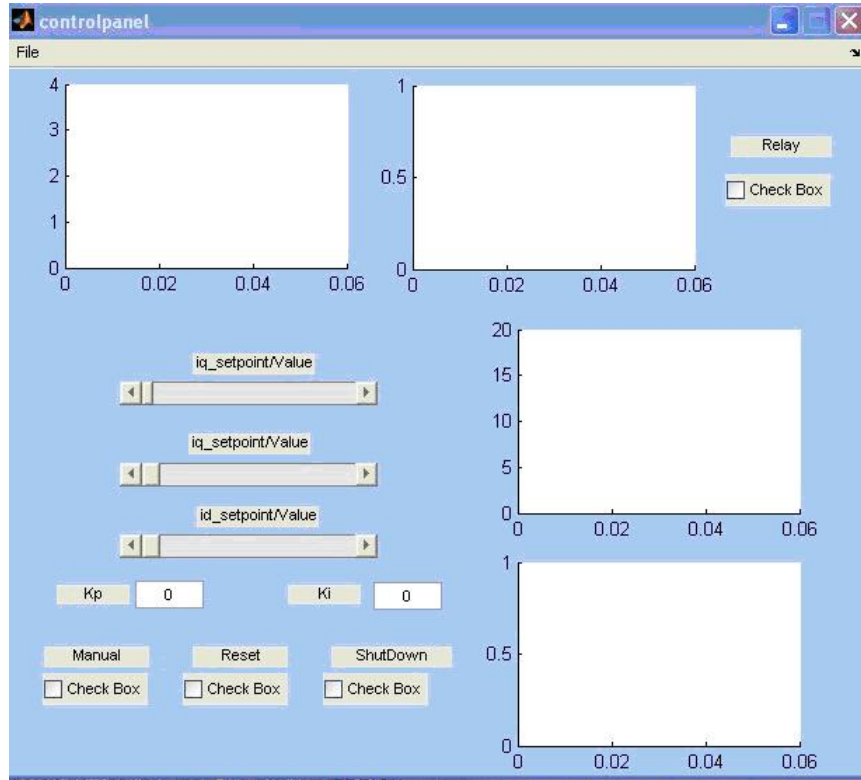


Figure 3.12: GUI for RTDX.

all data sent to the target. If the RTDX Host Library receives a data request from the target application with sufficient data in the host buffer to satisfy the request, it sends the data to the target. The data is written to the requested location without interfering with the target application. The host notifies the RTDX Target Library upon operation completion.

An XDS560 JTAG scan-based emulator, as shown in Figure 3.11, is a 3rd generation emulation controller supporting high-speed RTDX on enabled processors for real-time data rates of over 2 MB/second. It provides an unparalleled level of real-time visibility into an executing application and is extremely well-suited for debugging the demanding requirements of video and other high-speed DSP applications. The XDS560 can achieve code download speeds of over 500 Kbytes per second improving start-up times for larger applications and thus speeding development. The XDS560 also enables real-time non-intrusive Advanced Event Triggering capabilities, including event sequence detection, extended benchmarking capabilities, and program range breakpoints.

### **3.2.3.2 Matlab GUI program**

A graphical user interface (GUI) is a graphical display that contains devices, or components, that enable a user to perform interactive tasks. To perform these tasks, the user of the GUI does not have to create a script or type commands at the command line. Often, the user does not have to know the details of the task at hand.

The GUI components can be menus, toolbars, push buttons, radio buttons, list boxes, and sliders—just to name a few. In Matlab, a GUI can also display data in tabular form or as plots, and can group related components.

In order to test the peripheral auxiliary circuit of F28335 and the RTDX, some communication programs have been made in Matlab by using the graphical user interface. These programs have been developed for the testing of ADC, digital input, digital output and PWM, respectively. The interface of the control panel is shown in Figure 3.12 and the partial codes are clearly set out in Appendix C.

## Chapter 4

# Maximum Power Point Tracking

Wind power has been regarded as one of the main alternative renewable power sources to fossil fuels. Many countries have set strategic plans to develop technology for utilising wind power and a lot of researchers have shifted into this area. During the last decade, more and more attention has been paid to utilising renewable energy sources to tackle the energy crisis we are facing. Wind power has attracted most of the attention and many countries have launched various initiatives to increase the share of wind power in electricity generation.

Normally, wind generation systems can be divided into variable-speed generation systems and fixed-speed generation systems. Variable-speed generation systems are more attractive than fixed-speed systems due to improved wind energy production and reduction of the flicker problem. The efficiency of the wind turbine is higher than conventional ones. However, it does not mean that the actual efficiency is always high. It depends on the control algorithm used to extract the output power from the wind turbine. An advanced technique will be designed to extract the maximum power from the wind turbine under all working conditions. In variable-speed generation systems, the wind turbine can be operated at its maximum power operating point for various wind speeds by maintaining the tip speed ratio at the value that maximises aerodynamic efficiency. In order to achieve this ratio, the permanent magnet synchronous generator load line should be matched very closely to the maximum power line of the wind turbine generator. A variety of control schemes have been studied in order to produce as much power as possible from various wind speeds.

During the last few decades, many different maximum power point tracking control strategies have been developed. Among the MPPT methods, the hill-climbing method

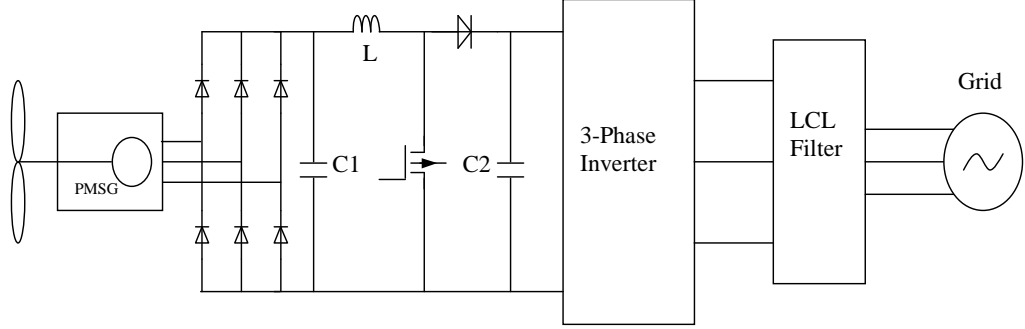


Figure 4.1: Topology of the system.

for comparing kW variation is the simplest but least efficient [13]. [14] developed a fuzzy controller for tracking the generator rotor velocity corresponding to the wind speed to extract the maximum power. Tan and Islam presented three sensorless control methods: wind prediction, the fixed voltage scheme for the inverter and current- controlled inverter [15]. An advanced hillclimb searching method, taking into account the wind-turbine inertia, was proposed in [16]. Datta and Ranganathan developed a generator velocity reference, which is dynamically modified in accordance with the magnitude and direction of change of active power [17]. [18] presented a method considering the duty cycle of the DC-DC buck-boost converter as a control variable. [19] presented a method of adjusting the duty cycle of the DC-DC buck-boost converter by using the gradient approximation algorithm. Many papers have adopted a boost converter to implement MPPT with different control strategies [20, 21].

## 4.1 System Configurations

The wind turbine system studied in this chapter is shown in Figure 4.1. It includes a wind turbine, a permanent magnet synchronous generator, a three-phase bridge rectifier, a boost DC-DC converter and a voltage source DC-AC inverter. In order to simplify the MPPT analysis, commonly used DC-AC inverters will not be considered, instead, a resistor is connected directly. The resistor provides a virtual load for consuming the real power generation.

The AC output from the PMSG is rectified into a DC signal by three-phase diode rectifier circuits. The boost converter comprises an inductor, an IGBT switch and a diode. This converter divides the DC bus into two parts: the DC bus voltage at the

output terminals of the diode rectifier, which is a variable DC bus voltage, and the DC bus voltage at the input terminals of the voltage source inverter, which is fed from a fixed DC bus voltage. The output current of the generator-rectifier system can be controlled by changing the duty cycle of the switch. Its purpose is to control the rectifier output current, and therefore the generator current and torque, so that the maximum power can be captured from the wind by the turbine. The duty cycle of the boost converter is the only control variable for achieving MPPT.

## 4.2 MPPT Control Strategy

As is well known, the rotating speed of a generator is proportional to the peak output voltage with constant excitation, meanwhile the torque of the machine is proportional to the peak output current with constant excitation. In this control strategy, the current reference of the input current of the boost converter is determined from the climbing algorithm according to the speed of generator. The input current of the boost converter will be controlled to follow the current reference by PI control. As a result, the wind turbine can generate the maximum output power. More details of the climbing algorithm are shown as follows.

### 4.2.1 Permanent magnet synchronous generator

Considering all the generators that are used in wind turbines, PMSG's have the highest advantages because they are more stable and secure during normal operation and they do not require an additional DC supply for the excitation circuit. The equivalent circuit for each phase [22] is shown in Figure 4.2.

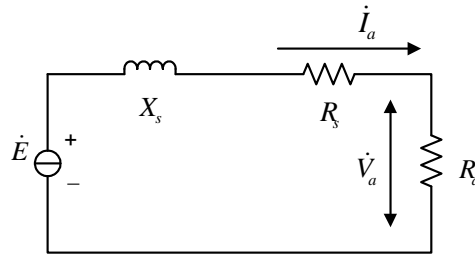


Figure 4.2: Equivalent circuit for each phase of PMSG.

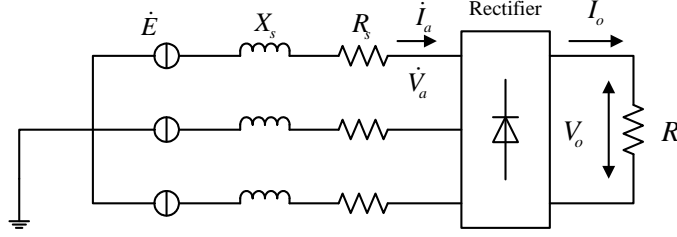


Figure 4.3: Connection of a diode rectifier to the generator.

The electromotive force  $E$  of the permanent magnet synchronous generator is shown as follow

$$E = k\phi\omega_g, \quad (4.1)$$

where  $k$  is the constant of the generator according to different types;  $\phi$  is a field magnetic flux by the permanent magnet; and  $\omega_g$  is the mechanical angular velocity.

The terminal voltage  $V_g$  of the generator is shown as follows

$$\vec{V}_g = \vec{E} - R_s \vec{I}_a - jX_s \vec{I}_a, \quad (4.2)$$

where  $I_a$  is the line current of the generator;  $R_s$  is the resistance of the stator windings; and  $X_s$  is the inductance of the stator windings.

The line current of the generator is shown like Equation (4.3) from Equation (4.2), and the amplitude of line current is expressed as Equation (4.4)

$$\vec{I}_a = \frac{\vec{E}}{(R_s + R_a) + jX_s}, \quad (4.3)$$

$$I_a = \frac{E}{\sqrt{(R_s + R_a)^2 + X_s^2}}. \quad (4.4)$$

#### 4.2.2 Uncontrollable rectifier

Three-phase diode rectifier circuits have the characteristics in which the phase of the largest line-to-line voltage is conducted. The current phase becomes always equal to the phase voltage, and the power factor of the fundamental wave approximates to one. The generator is connected with rectifier circuits as in Figure 4.3.



It is assumed that the AC power generated from the generator is converted into DC power through diode bridge rectifier circuits. Equation (4.5) will be obtained

$$3V_a I_a = V_o I_o, \quad (4.5)$$

where  $V_o$ ,  $I_o$  are the output voltage and the current of the rectifier, respectively.

The relationship between  $V_a$  and  $V_o$  can be expressed as follows

$$V_o = \frac{3\sqrt{6}}{\pi} V_a. \quad (4.6)$$

From Equation (4.5) and (4.6), the equation of  $I_a$  and  $I_o$  can be obtained

$$I_o = \frac{\pi}{\sqrt{6}} I_a. \quad (4.7)$$

Let  $R_a = \frac{V_a}{I_a}$  and  $R = \frac{V_o}{I_o}$ , then from Equation (4.6) and (4.7), the following equation is obtained

$$\frac{V_o}{I_o} = \frac{18}{\pi^2} \frac{V_a}{I_a} \Rightarrow R = \frac{18}{\pi^2} R_a. \quad (4.8)$$

From Equation (4.1), (4.4) and (4.8), the generated output power  $P$  can be calculated as a function of  $I_o$ ,  $V_o$  and angular velocity  $\omega_g$ ,

$$\begin{aligned} P &= 3V_a I_a \cos\varphi = 3R_a I_a^2 \\ &= \frac{\pi^2 V_o}{6I_o} \frac{(k\phi\omega_g)^2}{\left[\frac{\pi^2 V_o}{18I_o} + R_s\right]^2 + X_s^2}. \end{aligned} \quad (4.9)$$

The rotational speed of the generator always changes with the wind speed.  $I_o$  must be controlled effectively in order to obtain the electric power, while the maximum power point is captured. Based on Equation (4.9),  $I_o$ , in which the electric power becomes its maximum value, is deduced. It is defined as follows in order to simplify the calculation. Let

$$x = \frac{\pi^2}{18} \frac{V_o}{I_o}. \quad (4.10)$$

By substituting Equation (4.10) in (4.9),

$$P = \frac{3(k\phi\omega_g)^2 x}{(x + R_s)^2 + X_s^2}. \quad (4.11)$$

Calculating  $P$  on  $I_o$  partial derivatives,

$$\begin{aligned}
\frac{\partial P}{\partial I_o} &= \frac{\partial P}{\partial x} \frac{\partial x}{\partial I_o} = \frac{3(k\phi\omega_g)^2(R_s^2 + X_s^2 - x^2) - \pi^2 v_o}{[(x + R_s)^2 + X_s^2]^2} \frac{-\pi^2 v_o}{18I_o^2} \\
&= \frac{\pi^2(k\phi\omega_g)^2 V_o}{3I_o} \frac{x^2 - (R_s^2 + X_s^2)}{[(x + R_s)^2 + X_s^2]^2} \\
&= \frac{\pi^2(k\phi\omega_g)^2 V_o}{3I_o} \frac{[\frac{\pi^2}{18} \frac{V_o}{I_o}]^2 - (R_s^2 + X_s^2)}{[(\frac{\pi^2}{18} \frac{V_o}{I_o} + R_s)^2 + X_s^2]^2}. \tag{4.12}
\end{aligned}$$

This has the extreme value when Equation (4.12) becomes zero; the extreme points will be obtained. It is easy to know that

$$\frac{\pi^2(k\phi\omega_g)^2 V_o}{3I_o} \geq 0,$$

and

$$[(\frac{\pi^2}{18} \frac{V_o}{I_o} + R_s)^2 + X_s^2]^2 > 0.$$

Let

$$[\frac{\pi^2}{18} \frac{V_o}{I_o}]^2 - (R_s^2 + X_s^2) = 0,$$

then

$$I_o^* = \frac{\pi^2 V_o}{18} \frac{1}{\sqrt{R_s^2 + X_s^2}}, \tag{4.13}$$

when  $I_o \in (0, I_o^*)$ ,  $\frac{\partial P}{\partial I_o} > 0$ , it is a monotonic increasing function; when  $I_o \in (I_o^*, +\infty)$ ,  $\frac{\partial P}{\partial I_o} < 0$ , it is a monotonic decreasing function. Therefore, when  $I_o = I_o^*$ , the maximum power can be captured. Figure 4.4 illustrates the output power of a wind turbine versus the output current of the rectifier while the speed of wind is changed from  $V_1$  to  $V_3$ . ( $V_1 < V_2 < V_3$ )

As can be seen from Figure 4.4, for example, if the speed of the wind is  $V_1$ , the maximum power can be captured when the current is  $I_1$ . If the wind speed changes from  $V_1$  to  $V_2$  while the duty cycle is fixed at  $I_1$ , the operating point of the system is Point B which does not correspond to the maximum power tracking. The current should be decreased from  $I_1$  to  $I_2$  which results in the maximum power at operating Point C. In general, a climbing algorithm can be used to solve this kind of problem.

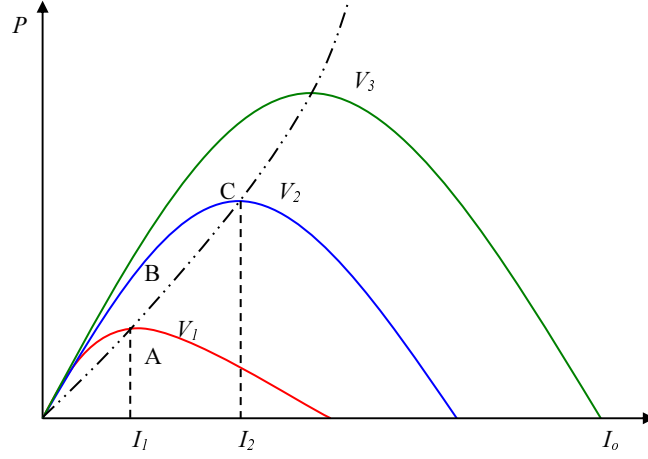


Figure 4.4: Power versus output current of a rectifier for three different wind speeds.

---

**Algorithm 4.1** Climbing algorithm (modified from [21])

---

- 1) Measure the output power  $P = VI$  and increase the reference current by one step
- 2) Measure the output power again.
- 3) Calculate  $\Delta P$  and  $\Delta I$ .
- 4)  $I^*(n) = I^*(n-1) + I_{step} \frac{\Delta P}{\Delta I}$ .
- 5) Repeat from Step 2 to reach to the optimum operating point.

Where  $V$ ,  $I$  are the output voltage and current of the rectifier, respectively.

---

This climbing algorithm, which adopts the different steps according to  $\frac{\Delta P}{\Delta I}$ , is shown in Algorithm 4.1. In this way, it will make the system respond quickly.

The output current of the rectifier should be controlled to track the reference current that is obtained from the climbing algorithm. As a result, the maximum power will be captured. The basic structure and control topology of the boost converter is shown in Figure 4.5. The transfer function of a PI controller is given by

$$C_{PI}(s) = K_p + \frac{K_i}{s}, \quad (4.14)$$

where  $K_p$  and  $K_i$  are proportional and integral gains respectively.

## 4.3 Simulation Results

### 4.3.1 Model of a wind turbine

The wind turbine model is shown in the following scheme (see Figure 4.6).

The tip speed ratio  $\lambda$  is calculated in the first subsystem using

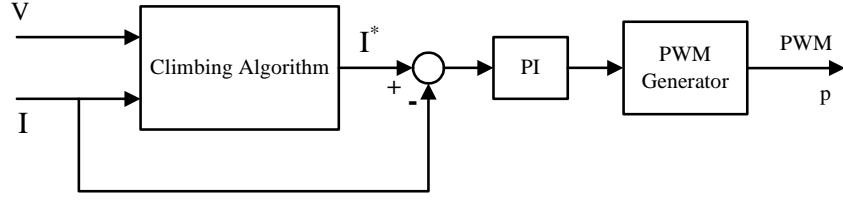


Figure 4.5: Control strategy.

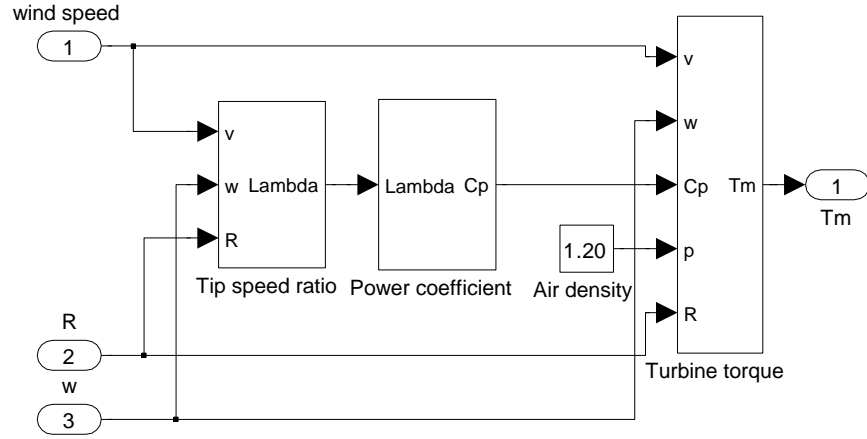


Figure 4.6: Wind turbine model.

$$\lambda = \frac{R\omega}{v}.$$

where  $R$  is the radius of the blades;  $v$  is the wind speed; and  $\omega$  is the rotation speed of the rotor.

The power coefficient  $C_p$  value is calculated in the next subsystem by using the following formulas [23]:

$$C_p(\beta, \theta) = 0.22 \left( \frac{116}{\beta} - 0.4\theta - 5 \right) e^{-\frac{12.5}{\beta}}$$

and

$$\beta = \frac{1}{\frac{1}{\lambda + 0.08\theta} - \frac{0.035}{\theta^3 + 1}}.$$

$C_p$  depends on the tip speed ratio  $\lambda$  of the wind turbine and the angle of blades  $\beta$ . The wind turbine extracts power from the wind and then converts it into mechanical

power. The amount of aerodynamic torque is related to the wind speed as follows:

$$T_m = \frac{P_m}{\omega} = \frac{1}{2} \rho \pi R^2 \frac{v^3}{\omega} C_p,$$

where  $\rho$  is the air density;  $R$  is the turbine radius;  $v$  is the wind speed; and  $\omega$  is the turbine rotor speed.

In our case, the angle of blades is constant. The turbine power coefficient  $C_p$  is a function only of the tip speed ratio. When  $\lambda$  takes the optimal value  $\lambda_{opt}$ , the power coefficient  $C_p$  becomes a maximum. When  $\lambda$  is controlled by the optimum value  $\lambda_{opt}$ , regardless of the wind speed, the maximum mechanical power is obtained from the wind energy.

#### 4.3.2 Model of a permanent magnet synchronous generator

One of the advantages of using a PMSG in wind power applications is its higher efficiency. The elimination of the gearbox, and the introduction of the variable speed control, would further increase the availability of the system, reduce its active weight and the need for maintenance.

The PMSG equations are expressed in the rotor reference frame ( $qd$  frame):

$$V_d = L_d \frac{dI_d}{dt} + R_s I_d - \omega_r L_q I_q,$$

$$V_q = L_q \frac{dI_q}{dt} + R_s I_q + \omega_r L_d I_d + \omega_r \lambda_0,$$

$$T_e = \frac{3}{2} \left( \frac{p}{2} \right) (\lambda_0 I_q + (L_d - L_q) I_d I_q),$$

$$\omega_r = \frac{p}{2} \omega,$$

$$\frac{d\omega}{dt} = \frac{1}{J} (T_m - T_e - F\omega),$$

$$\frac{d\theta}{dt} = \omega,$$

where,

Table 4.1: Parameters of the PMSG.

Parameters	Values	Parameters	Values
$Ld$	$0.975mH$	$Lq$	$0.975mH$
$Rs$	$0.0918\Omega$	Flux linkage	$0.1688V.s$
Inertial	$3.94e-3kg.m^2$	Friction	$4.924e-4N.m.s$
Pole pairs	4	$Ts$	$1e-6$

$L_q, L_d$ :  $q$  and  $d$  axis inductances

$R$ : Resistance of the stator windings

$I_q, I_d$ :  $q$  and  $d$  axis currents

$V_q, V_d$ :  $q$  and  $d$  axis voltages

$\omega_r$ : Angular velocity of the rotor

$\lambda_0$ : Amplitude of the flux induced by the permanent magnets of the rotor in the stator phases

$p$ : Number of pole pairs

$T_e$ : Electromagnetic torque

$\omega$ : Rotation speed of the rotating frame.

The Park transformation is commonly used in three-phase electric machine models. It transforms from a three-phase ( $abc$ ) reference frame to a  $dq0$  reference frame. The following transformations are used

$$I_d = \frac{2}{3}(I_a \cos\theta + I_b \cos(\theta - \frac{2}{3}\pi) + I_c \cos(\theta + \frac{2}{3}\pi)),$$

$$I_q = \frac{2}{3}(I_a \sin\theta + I_b \sin(\theta - \frac{2}{3}\pi) + I_c \sin(\theta + \frac{2}{3}\pi)).$$

The Clarke transformation transforms it from a  $dq0$  reference frame to a three-phase ( $abc$ ) reference frame. The following transformations are used

$$V_a = V_d \cos\theta - V_q \sin\theta,$$

$$V_b = V_d \cos(\theta - \frac{2}{3}\pi) - V_q \sin(\theta - \frac{2}{3}\pi),$$

$$V_c = V_d \cos(\theta + \frac{2}{3}\pi) - V_q \sin(\theta + \frac{2}{3}\pi),$$

Table 4.2: Parameters of the boost converter.

Parameters	Values	Parameters	Values
C1	$680\mu F$	C2	$1360\mu F$
L	$2mH$	R	$100\Omega$

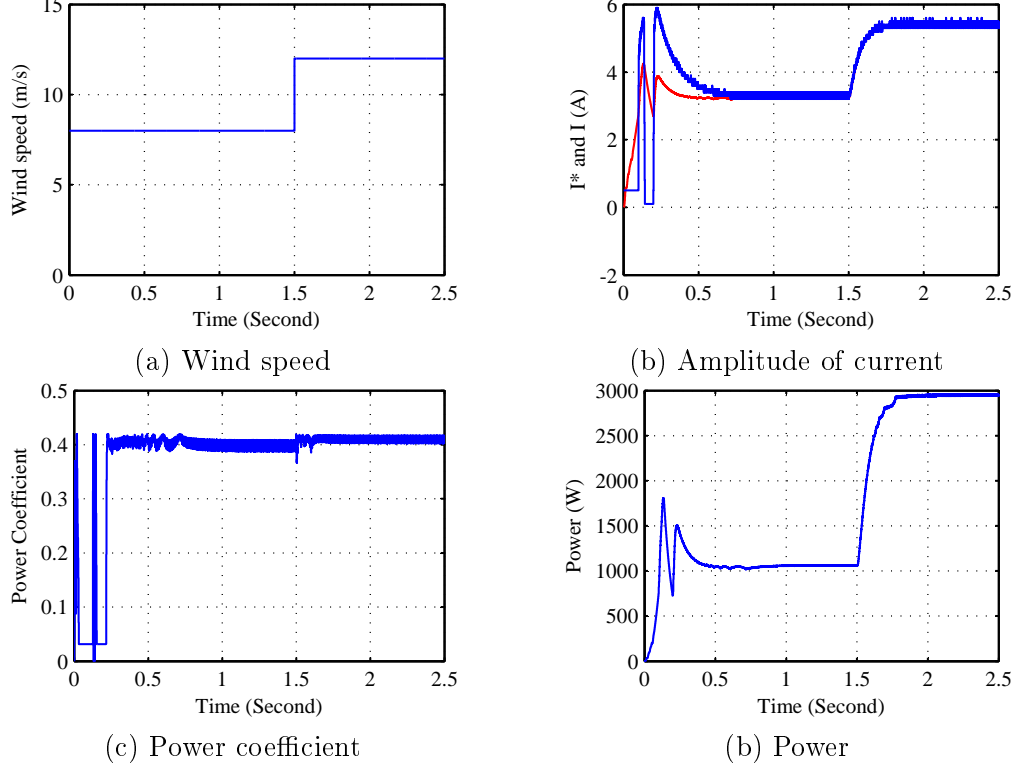


Figure 4.7: Simulation results.

$$\theta = \omega t.$$

The parameters of the generator used in the simulations are given in Table 4.1.

#### 4.3.3 Simulation of MPPT

This simulation has been made by using the blocks mentioned in MATLAB/ Simulink/ Sim-PowerSystems. The solver used in the simulations was ode23t with a relative tolerance of  $10^{-3}$  and the sampling time was  $10 \mu s$ . The AC power generated from the permanent magnet synchronous generator is converted into DC power through a diode bridge rectifier. The duty cycle of the boost converter is controlled to track the

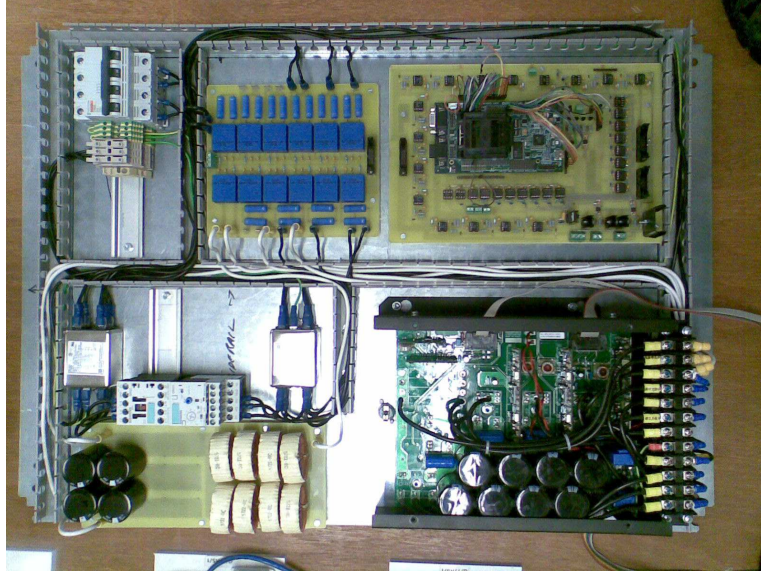


Figure 4.8: Experimental setup.

reference current generated by the climbing algorithm.

The parameters of the boost converter used in the simulations are given in Table 9.1.

The simulation was started at  $t = 0$ . The initial time is from  $t = 0$  to 0.2s, so the first 0.2 second is ignored in our analysis. The wind speed was changed from 8 to 12m/s at  $t = 1.5$ s. The simulations were carried out in Matlab7.6/Simulink. The solver used in the simulations was ode23t with a relative tolerance of  $10^{-3}$  and a maximum step size of  $10 \mu\text{s}$ .

The simulation results are shown in Figure 4.7. The output current of the rectifier  $I$  (blue line) tracked the reference current  $I^*$  (red line) very well in (b). The power coefficient  $C_p$  was at almost maximum all the time, regardless of the wind speed in (c). The system responses were stable and very quick. When the wind speed was changed from 8 to 12 m/s at  $t=1.5$ s, the power was increased from 1000 to 2900W in 0.3 second.

## 4.4 Experimental Results

The experimental setup, shown in Figure 4.8, consists of a I/O conditioning board, a measurement transducers board, a boost converter board, an LCL filter board, a Semistack IGBT device consisting of an uncontrollable rectifier and an inverter, a



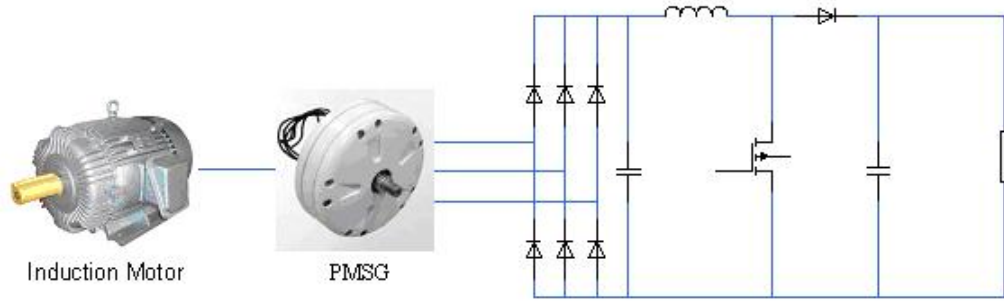


Figure 4.9: The experimental topology for MPPT.

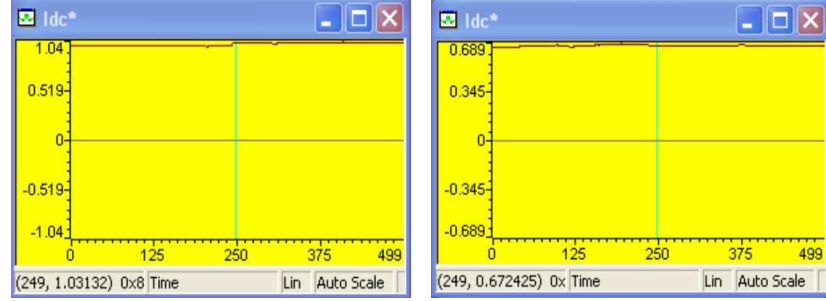
TMS320F28335 digital signal controller and a Code Composer Studio, and MATLAB Simulink/ SimPowerSystems Package and Target Support Package TC2.

The speed controllable induction motor has been used as a wind turbine in the initial experiments. The AC power generated from the permanent magnet synchronous generator is converted into DC power through the diode bridge rectifier. In the DC bus, a boost converter has been used to achieve maximum power point tracking. Because the duty cycle of the boost converter is the only control variable, and the real power measured at the converter output is considered, normally used inverters or energy storages will not take simplicity into account, so instead a resistor is connected directly. The resistor provides a virtual load for consuming the real power generation. The experimental topology is shown in Figure 4.9.

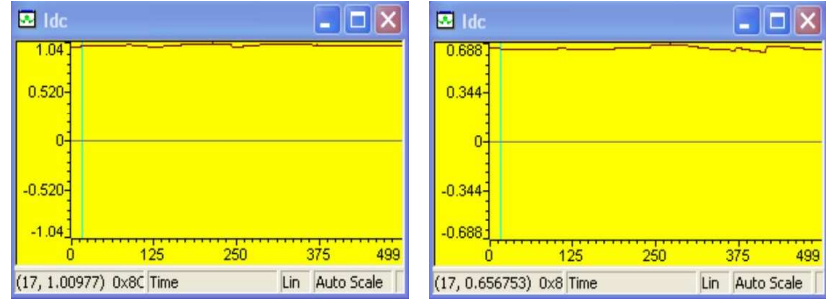
Experimental results (see Figure 4.10) have been obtained from Code Composer Studio 3.3 in real time mode. In Figure 4.10 the left column shows the experimental results when the induction motor was operated at 300rpm. The reference  $I^*$  and the actual  $I$  are around 1.04. The duty cycle  $D$  is around 29.6%. Reference  $I^*$ , actual  $I$  and duty cycle  $D$  were changed in Figure 4.10's right column when the induction motor was operated at 150rpm.

## 4.5 Conclusions

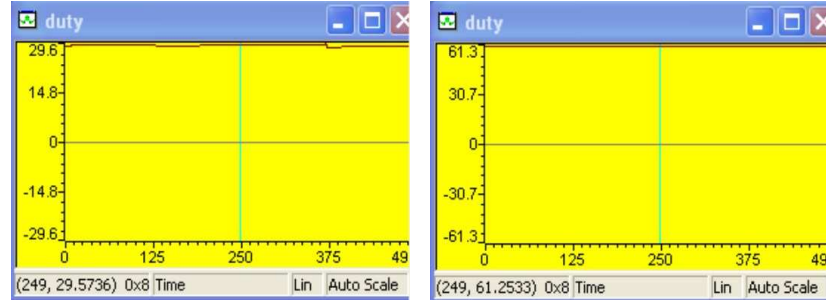
In this chapter, a simple MPPT control scheme is proposed for the wind turbine application without mechanical sensors by using a climbing algorithm and a PI controller. Both simulation and experimental results are provided to confirm that the control strategy works well to track the maximum power for different wind speeds.



(a) Reference current



(b) Inductor current



(c) Duty cycle

Figure 4.10: Experimental results: for the case with 300rpm (left column) and 150rpm (right column).

## Chapter 5

# Overview of the Synchronverter Technology

Power systems currently receive more and more contributions from distributed energy sources, in particular, from renewable energy sources. Renewable energy sources are uncontrollable and highly non-linear. If their share in a power system becomes significant, a modern control strategy is required not only to preserve, but also to improve the stability of the power system. It is one of the biggest challenges for all researchers working in this area to propose the most efficient way to send renewable power to the grid without degrading the system stability.

In general, the control schemes for sending power from a renewable energy source to the utility grid are quite similar and include two stages. In the first stage, the source power is converted into electrical power, often in the form of DC, using appropriate techniques. The second stage is to feed the electrical power to the utility grid, often via DC-AC converters, also called inverters. Various control strategies can be applied at this stage to control the power flowing into the grid from the DC bus. Different control strategies have different ways of feeding the power to the grid and therefore the impact on the stability of the power system is different.

Different control methods can be applied at the second stage to control grid-connected inverters. The two most-studied methods are power (torque) angle control and current vector control for voltage source inverters (VSI). Generally, the current vector control method aims at delivering current flows with low harmonic distortion to the grid while maintaining a stable DC bus voltage [24, 25, 26, 27]. Because the source model for the inverter in this method is a current source mode [28], maintaining the DC bus voltage

means transferring all the available power from the source to the grid to avoid fluctuations of the DC bus voltage. In most renewable energy systems, the power available on the DC bus is achieved from maximum power point tracking (MPPT) algorithms [29, 18] and, hence, the inverter simply feeds the maximum power available to the grid. Because of the fast response and the ability of limiting the currents within the control loops, this strategy is popular and is dominant in most grid-connected applications nowadays [30, 31].

The strategy for sending the maximum power extracted to the grid with current control methods is considered to be suitable as long as the share of the renewable source is not significant. In this case, the power surge from renewable sources would be compensated by large synchronous generators within the power system. In other words, the main large generators in the system are responsible for the whole system stability, taking care of any disturbances on the grid. When the share of renewable energy sources reach a certain level, the strategy to inject all maximum power from renewable sources to the grid is untenable and is very likely to cause instability to the whole power system.

The power (torque) angle control method is another control method. The real power flowing to the grid is controlled by the phase difference, called the power angle or torque angle, between the generated voltage and the grid voltage. The reactive power is controlled by regulating the amplitude of the generated voltage. This control method is in line with the behaviour of a synchronous generator connected to the grid [32] and has been proposed to control high power grid-connected inverters to improve system stability, such as the HVDC system [31] and STATCOM [33, 34]. The control strategy proposed in [31] is a variant of the power angle control method, taking into account the current control as an auxiliary function.

Several strategies are based on the operational principles of SG [32] from different angles. Since synchronous generators have been studied for more than 100 years and the technology has now reached high maturity, it makes sense to design a controller to mimic the behaviour of an SG connected to the grid. Implementations along this line include the virtual synchronous machine (VISMA) [35], the VSGs [36, 37, 38, 39] and the synchronverters [40, 1]. The synchronverter includes the mathematical model of a synchronous machine and behaves in the same way as a synchronous generator mathematically to provide a voltage supply. It can be operated in standalone mode or grid-connected mode and the transition between the modes is seamless. It can send a set power to the grid and is also able to take part in the regulation of the system

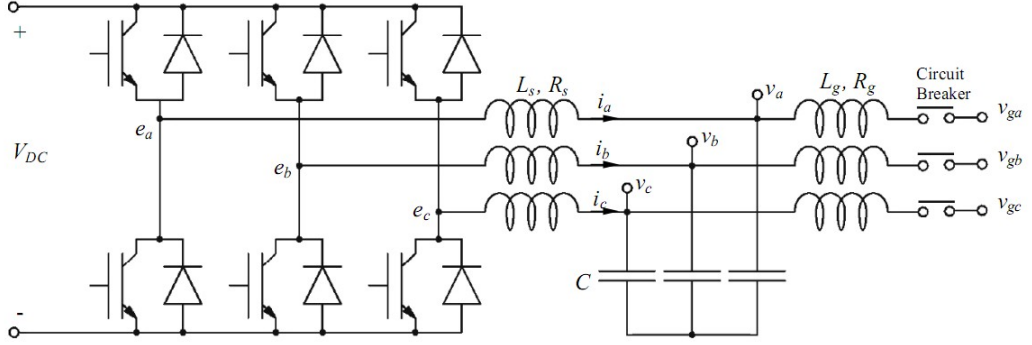


Figure 5.1: The power part of a synchronverter, modified from [1, Figure 2]

frequency and voltage. Moreover, it is able to be operated in parallel to share the real power and reactive power accurately. Because of the embedded mathematical model, a utility company is able to control a synchronverter in the same way as controlling a synchronous generator, which considerably facilitates the grid connection of renewable energy and smart grid integration.

## 5.1 Synchronverter Technology

A synchronverter is an inverter that mimics a synchronous generator [40, 1]. The core of the controller is the mathematical model of a synchronous generator, which is then wrapped with some functions to regulate the real power and reactive power, voltage and frequency. As a result, grid-connected renewable energy and distributed generation can easily take part in the regulation of the system frequency and voltage. A synchronverter consists of a power part, as shown in Figure 5.1, and an electronic part, as shown in Figure 5.2. The controller includes the mathematical model of a three-phase round-rotor synchronous generator described as follows.

The structure of an idealised three-phase round-rotor synchronous generator is shown in Figure 5.3. Assume that the three identical stator windings of a synchronous generator are distributed in slots around the periphery of the uniform air gap; the stator windings can be regarded as concentrated coils having self-inductance  $L$ , mutual inductance  $-M$  (with  $M > 0$ , the negative sign is due to the  $\frac{2\pi}{3}$  phase angle) and resistance  $R_s$ .

Denote the flux vector and the current vector as

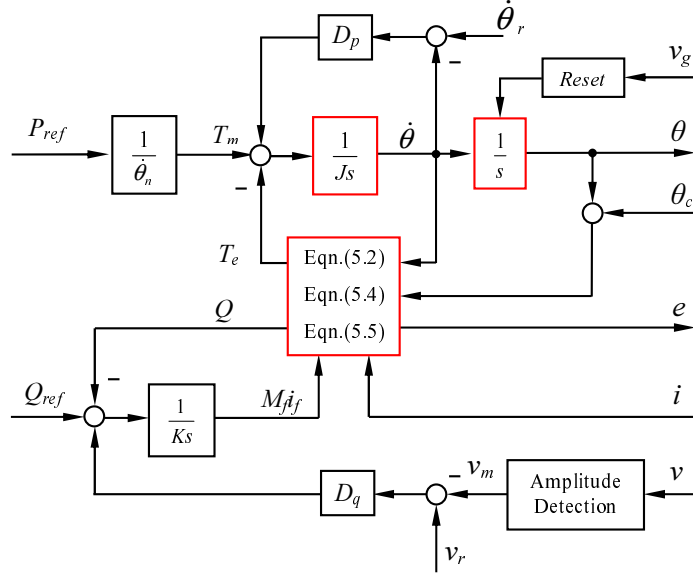


Figure 5.2: The electronic part (controller) of a synchronverter, modified from [1, Figure 3]

$$\Phi = \begin{bmatrix} \Phi_a \\ \Phi_b \\ \Phi_c \end{bmatrix}, \quad i = \begin{bmatrix} i_a \\ i_b \\ i_c \end{bmatrix},$$

respectively, and the vectors

$$\widetilde{\cos\theta} = \begin{bmatrix} \cos\theta \\ \cos(\theta - \frac{2\pi}{3}) \\ \cos(\theta - \frac{4\pi}{3}) \end{bmatrix}, \quad \widetilde{\sin\theta} = \begin{bmatrix} \sin\theta \\ \sin(\theta - \frac{2\pi}{3}) \\ \sin(\theta - \frac{4\pi}{3}) \end{bmatrix},$$

where  $\theta$  is the rotor angle with respect to the Phase A winding. Then the phase terminal voltages  $v = [v_a \ v_b \ v_c]^T$  of a generator can be written as

$$v = e - R_s i - L_s \frac{di}{dt}, \quad (5.1)$$

where  $L_s = L + M$  and  $e = [e_a \ e_b \ e_c]^T$  is the back EMF due to the rotor movement given by

$$e = M_f i_f \dot{\theta} \widetilde{\sin\theta} - M_f \frac{di_f}{dt} \widetilde{\cos\theta}. \quad (5.2)$$

The mechanical part of the generator is governed by

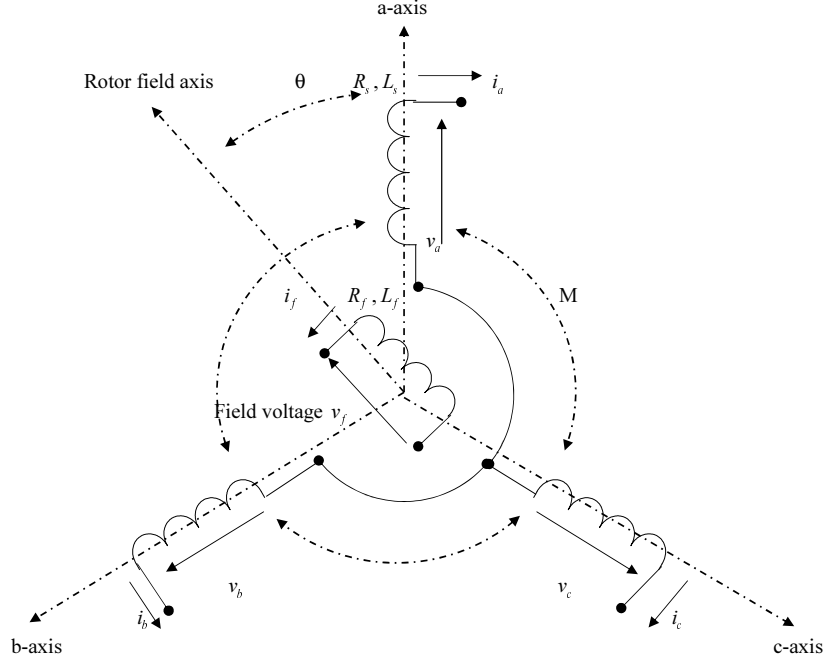


Figure 5.3: Structure of an idealized three-phase round-rotor synchronous generator, modified from [1, Figure 1]

$$\ddot{\theta} = \frac{1}{J}(T_m - T_e - D_p \dot{\theta}_g), \quad (5.3)$$

where  $J$  is the moment of inertia of all the parts rotating with the rotor;  $D_p$  is a damping factor;  $T_m$  is the mechanical torque and  $T_e$  is the electromagnetic torque

$$T_e = M_f i_f \langle i, \widetilde{\sin \theta} \rangle, \quad (5.4)$$

where  $\langle \cdot, \cdot \rangle$  denotes the conventional inner product in  $\mathbb{R}^3$ .

The real power and reactive power are, respectively,

$$\begin{aligned} P &= \dot{\theta} M f i_f \langle i, \widetilde{\sin \theta} \rangle, \\ Q &= -\dot{\theta} M f i_f \langle i, \widetilde{\cos \theta} \rangle. \end{aligned} \quad (5.5)$$

Similarly to the control of a synchronous generator, the controller of a synchronverter has two channels: one for the real power and the other for the reactive power. The real power is controlled by a frequency droop control loop, which is implemented in a synchronverter by comparing the virtual angular speed  $\dot{\theta}$  with the angular frequency

Table 5.1: The parameters of an inverter.

Parameters	Values	Parameters	Values
$L_f$	4 mH	$R_f$	0.1 $\Omega$
$L_g$	2 mH	$R_g$	0.1 $\Omega$
$C$	22 $\mu F$	Switching frequency	5 kHz
Nominal grid voltage	110 V <sub>rms</sub>	Nominal grid frequency	50 Hz

Table 5.2: The parameters of control strategy.

Paremeters	Values	Paremeters	Values
$D_p$	3.04	$D_q$	193.4
$J$	$6.08e^{-4}$	$K$	121.5

reference  $\dot{\theta}_r$  (which normally would be equal to the nominal angular frequency of the grid  $\dot{\theta}_n$ ), and adding this difference, multiplied with a gain, to the active mechanical torque  $T_m$ . The mechanical friction coefficient plus the frequency drooping coefficient is represented by  $D_p$ . This loop regulates the virtual angular speed  $\dot{\theta}$  of the synchronous generator and creates the phase angle  $\theta$  for the control signal  $e$ .

The regulation of reactive power flowing out of the synchronverter can be realised similarly. The reactive power is controlled by a voltage droop control loop, using the voltage droop coefficient  $D_q$ . This loop regulates the field excitation  $M_f i_f$ , which is proportional to the amplitude of the voltage generated.

## 5.2 Simulation Results

The synchronverter simulation was carried out in Matlab7.6/ Simulink/ SimpowerSystems. The solver used in the simulations was ode23t with a relative tolerance of  $10^{-3}$  and the sampling time was 10  $\mu s$ . The parameters of the inverter used in this simulation are given in Table 5.1 and the parameters of the control strategy are given in Table 5.2.

The simulation was started at  $t = 0$  s, with  $P_{ref} = 0$ ,  $Q_{ref} = 0$  and the PWM turned off. When  $t = 0.5$  s, the PWM was turned on. During this time, the synchronverter synchronised with the grid. At  $t = 1$  s, the circuit breaker was turned on. The real power reference was increased to  $P_{ref} = 2.5$  kW at  $t = 2$  s and the reactive power reference  $Q_{ref} = 500$  Var was applied at  $t = 4$  s. The grid frequency was set to be 49.9 Hz (i.e. decreased by 0.2%) at  $t = 6$  s and the simulation was stopped at  $t = 8$  s. The system responses are shown in Figure 5.4.



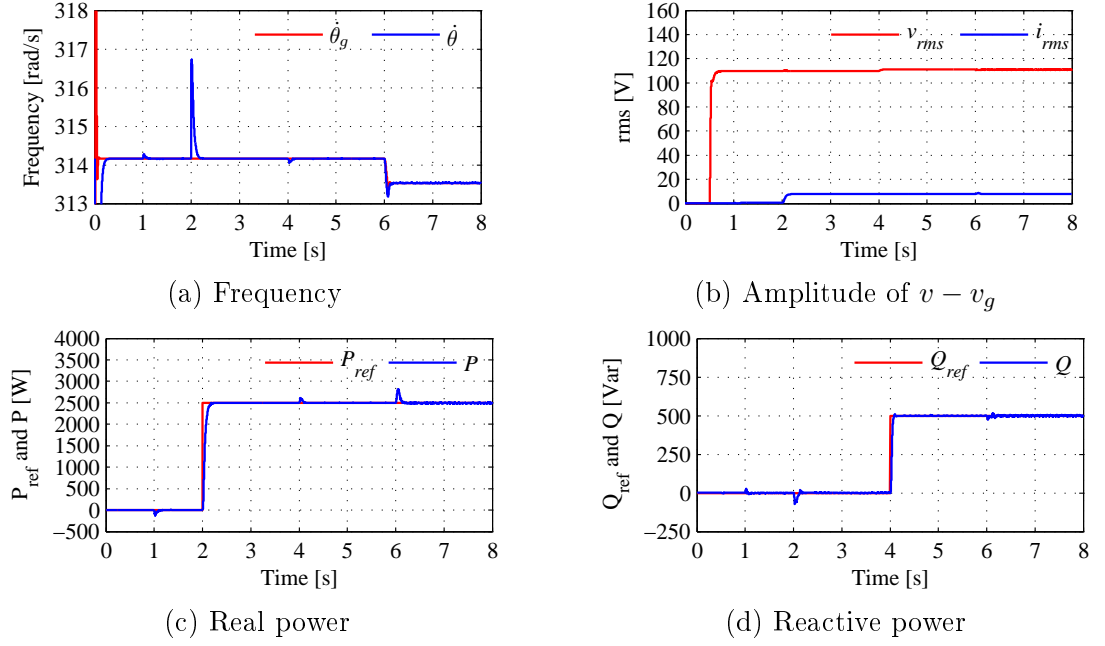


Figure 5.4: Simulation results

As shown in Figure 5.4(a), regardless of the reference  $P_{ref}$  and  $Q_{ref}$  applied, the synchronverter tracked the grid frequency very well, even when the frequency decreased by 0.1 Hz at  $t = 6$  s. Moreover, the real power and the reactive power tracked their references quickly and accurately under different operational conditions, as shown in Figure 5.4(c) and (d).

Figure 5.5 shows the grid voltage  $v_a$  and the control signal  $e_a$  in the different cases. Obviously, there were no big differences between the cases of before connection and after connection. The control signal  $e_a$  was synchronised with the grid voltage  $v_a$  (in terms of phase and frequency). When  $P_{ref} = 2.5$  kW, the control signal  $e_a$  had a small phase shift with the grid voltage  $v_a$  in Figure 5.5(c). Moreover, when  $Q_{ref} = 500$  Var, the control signal  $e_a$  increased slightly in Figure 5.5(d). It means that the real power and the reactive power are controlled by the frequency droop control loop and the voltage droop control loop, respectively.

### 5.3 Experimental Results

Experiments were also carried out on the experimental setup which is described in the previous chapter. The speed controllable induction motor was used to drive the per-

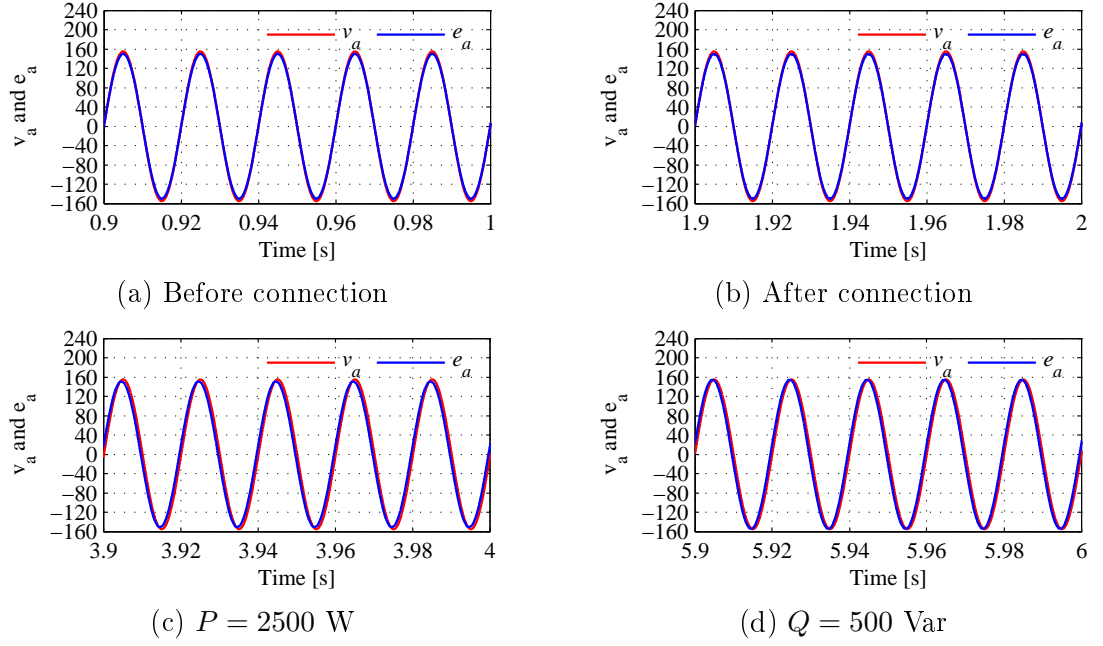


Figure 5.5: Grid voltage and control signal

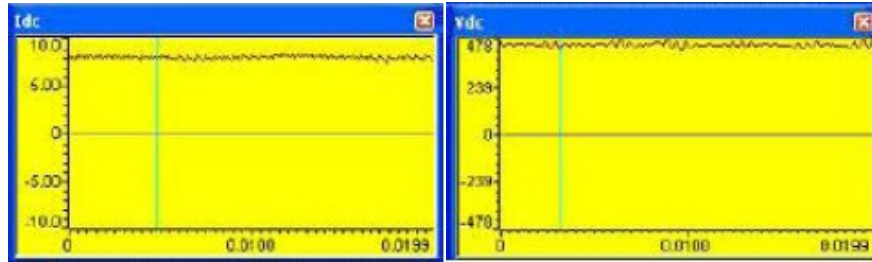
manent magnet synchronous generator. The AC power generated from the permanent magnet synchronous generator is converted into DC power through diode bridge rectifier. On the DC bus, a boost converter was used to control the DC bus voltage, which is the input voltage of the inverter, to be 480 V. The inverter is connected to the grid, a three-phase 400 V/50 Hz system, via an LCL filter and a three-phase 190/400 V step-up transformer.

The parameters are roughly the same as those given in Table 5.1, with the same control parameters given in Table 5.2. The experimental results of 2.5 kW output power are shown in Figure 5.6. The real power and the reactive power are shown in Figure 5.6(a). Figure 5.6(b) shows the DC bus voltage and current. The three-phase inverter output voltage and the three-phase grid voltage are shown in Figure 5.6(c).

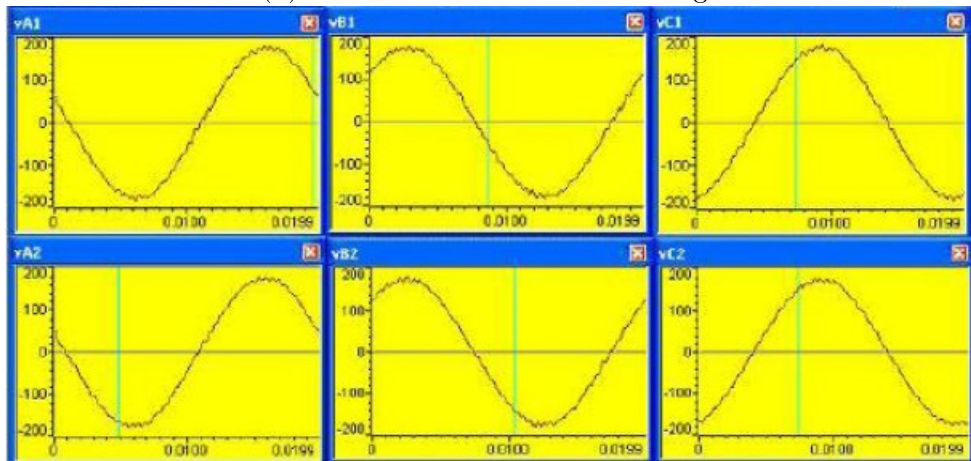
The difference between the inverter output voltage and the grid voltage at around the connection time is shown in Figure 5.7 with Phase  $a$  taken as an example. Before connection, the difference was about 0.2 V peak-to-peak, which was very small, and there was no problem to connect it to the grid.



(a) The real power and the reactive power



(b) The DC bus current and voltage



(c) the three-phase inverter output voltage and the three-phase grid voltage

Figure 5.6: 2.5kW experimental results

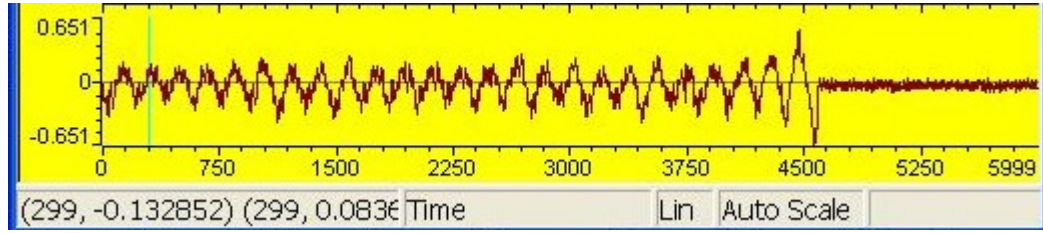


Figure 5.7: Error between output voltage and grid voltage

## 5.4 Conclusions

In this chapter, the synchronverter technology was introduced. It can be operated in the standalone mode or the grid-connected mode and the transition between the modes is seamless. It is able to send a set power to the grid and is also able to take part in the regulation of the system frequency and voltage. Moreover, it can be operated in parallel to share the real power and reactive power accurately. Both simulation and experimental results were provided.

## Chapter 6

# Synchronverters in Parallel Operation

As mentioned in the previous chapter, synchronverters can be operated in parallel to share the real power and reactive power accurately because of the voltage and frequency droop control method. In this chapter, the speciality of synchronverters with parallel operation was discussed and a synchronverter-based control scheme for parallel inverters was proposed.

Rapidly increasing DPGS based on renewable energy are connected to the public grid via power inverters. They often form microgrids before being connected to the utility grid [41, 42, 43, 44, 45]. Due to the availability of high current power electronic devices, it is inevitable that multiple inverters are needed to be operated in parallel for high-power and/or low-cost application. Additionally, inverters are widely used in stand-alone mode, such as UPS, energy storage systems and backup power supply systems. These applications can be implemented by using a high-capacity inverter or several low-capacity inverters. It is well-known that the use of a singular high-capacity inverter has many disadvantages [46]. In other words, the parallel operation of several low-capacity inverters is better than a singular high-capacity inverter due to the advantages of better extensibility and reliability. Consequently, the inverter that gives the performance of parallel operation is an important trend.

The conventional control methods for parallel-connected inverters can be classified into two types. One is the active current distribution type which uses active current distribution control to adapt the current-mode control. The object of the active current distribution control is to generate a reference current for each parallel-connected

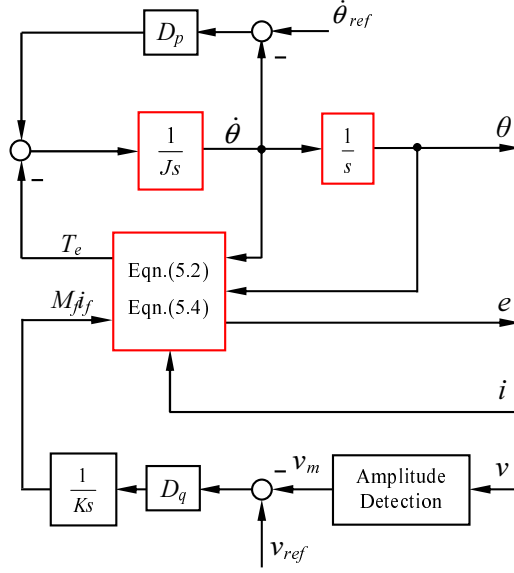


Figure 6.1: Proposed control scheme for parallel operation

inverter, and it can be subdivided into three methods: the master-slave control method [46, 47, 48], the concentrated distribution control method [49, 50] and the ring control method [51]. Another is the droop control [52, 53, 54, 55, 56, 57, 58, 59, 1], which is widely used in conventional power generation systems [60]. The advantage is that no external communication mechanism is needed among the inverters to share the load automatically [57, 61]. This enables good sharing for linear and/or nonlinear loads [62, 63, 64, 65, 66]. In some cases, external communication means are still adopted for load sharing [67] and restoring the microgrid voltage and frequency.

## 6.1 Description of the Control Scheme

A parallel operation control strategy based on synchronverters was proposed in Figure 6.1. In comparison to the synchronverter (see Figure 5.2),  $P_{set}$  and  $Q$  loop are removed from the controller. The real power is controlled by a frequency droop control loop, which is implemented in a synchronverter by comparing the virtual angular speed  $\dot{\theta}$  with the angular frequency reference  $\dot{\theta}_{ref}$ , and adding this difference, multiplied with a gain, to the active mechanical torque  $T_m$ . This loop regulates the virtual angular speed  $\dot{\theta}$  of the synchronous generator and creates the phase angle  $\theta$  for the control signal  $e$ . The mechanical friction coefficient plus the frequency drooping coefficient is represented

Table 6.1: The parameters used in the simulation.

Parameters	Values	Parameters	Values
$D_{p1}$	6.08	$D_{p2}$	3.04
$D_{q1}$	385.7	$D_{q2}$	192.8
$J_1$	0.0122	$J_2$	0.0061
$K_1$	242.34	$K_2$	121.17

by  $D_p$ . Defining the frequency drooping coefficient  $D_p$  as the change in the total torque acting on the imaginary rotor  $\Delta T$  and the change in angular frequency  $\Delta\dot{\theta}$  gives:

$$D_p = -\frac{\Delta T}{\Delta\dot{\theta}}.$$

The regulation of reactive power flowing out of the synchronverter can be realised similarly. This loop regulates the field excitation  $M_{fi}$ , which is proportional to the amplitude of the voltage generated. The reactive power is controlled by a voltage droop control loop, using the voltage droop coefficient  $D_q$ . Defining the voltage drooping coefficient  $D_q$  as the ratio of the required change of reactive power  $\Delta Q$  to the change of voltage  $\Delta v$  gives:

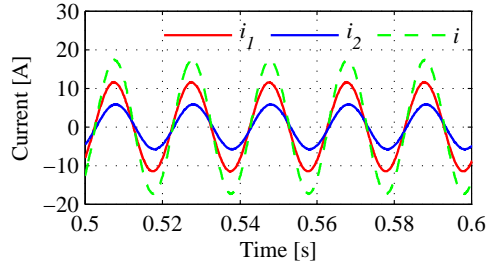
$$D_q = -\frac{\Delta Q}{\Delta v}.$$

## 6.2 Simulation Results

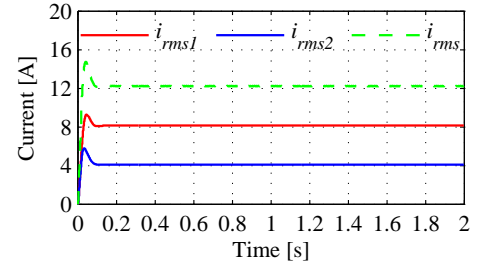
A system that consists of two three-phase inverters powered by two separate 400 V DC voltage supplies was used to carry out simulations to verify the control strategy. The simulations were carried out in Matlab7.6/ Simulink/ SimpowerSystems. The solver used in the simulations was ode23t with a relative tolerance of  $10^{-3}$  and the sampling time was 10  $\mu s$ . The rated voltage is 110V and the frequency of the system is 50Hz. The filter inductor is  $L = 2.2\text{mH}$  with a parasitic resistance of  $0.1\Omega$  and the filter capacitance  $C$  is  $22\mu\text{F}$ .

### 6.2.1 With a linear load

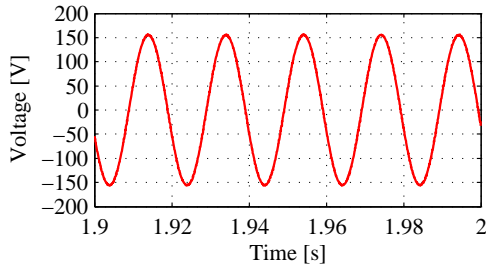
The capacity of Inverter 1 is 3000VA and the capacity of Inverter 2 is 1500VA. The parameters of simulation are shown in Table 6.1. Simulation was carried out for a



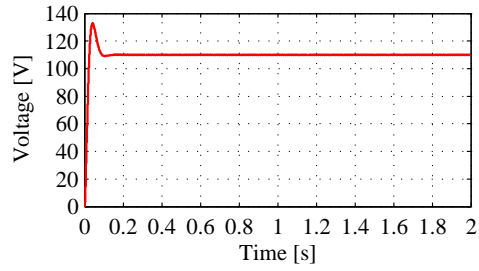
(a) Current  $i_1$ ,  $i_2$  and  $i$



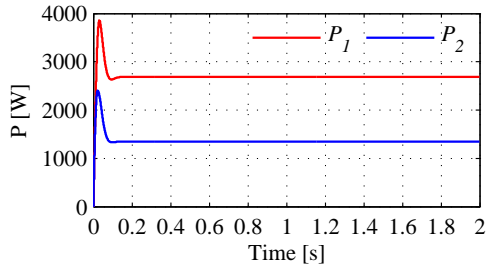
(b) RMS current  $i_{rms1}$ ,  $i_{rms2}$  and  $i_{rms}$



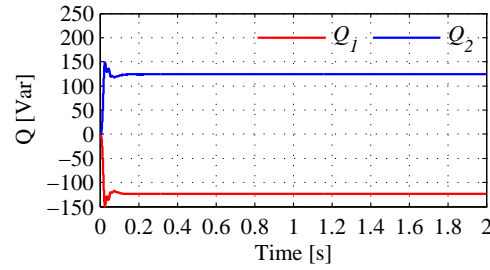
(c) Load voltage



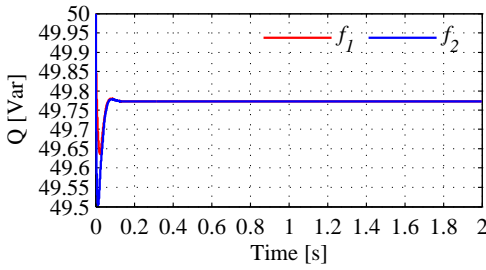
(d) RMS voltage of load



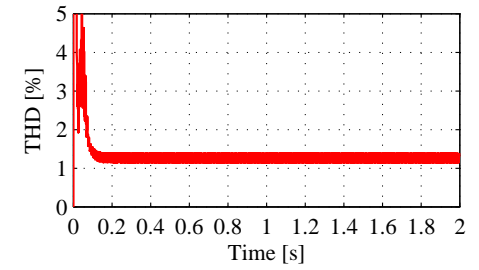
(e) Real power  $P_1$  and  $P_2$



(f) Reactive power  $Q_1$  and  $Q_2$



(g) Frequency  $f_1$  and  $f_2$



(h) THD of load voltage

Figure 6.2: Simulation results with a linear load



linear load with  $R = 9\Omega$  for each phase. The system responses are shown in Figure 6.2. It can be seen that the parallel operation of two inverters performed very well. The current of Inverter 1, Inverter 2 and load are shown in Figure 6.2 (a) with Phase A taken as an example. They are nearly sinusoidal with little phase shift between them and  $i_{rms1} + i_{rms2} = i_{rms}$ . The output voltage is very close to the rated voltage 110V with low THD (about 1.1%). The real power and reactive power are well shared.

### 6.2.2 With a nonlinear load

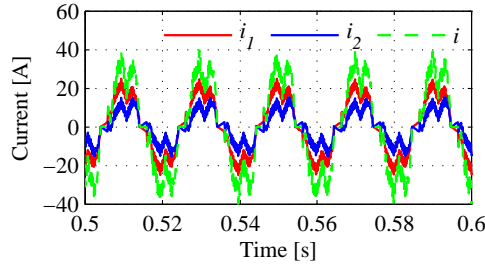
The same simulations were carried out for a full-bridge rectifier load with an LC filter  $L = 150\mu\text{H}$ ,  $C = 1000\mu\text{F}$  and  $R = 9\Omega$ . The system responses are shown in Figure 6.3. While this appliance consumes the real power, as it is a nonlinear load, it also outputs harmonics and consumes the reactive power. The real power and reactive power were accurately shared. The load voltage is close to the rated voltage with 21% THD.

### 6.2.3 Master-slave mode with a linear load

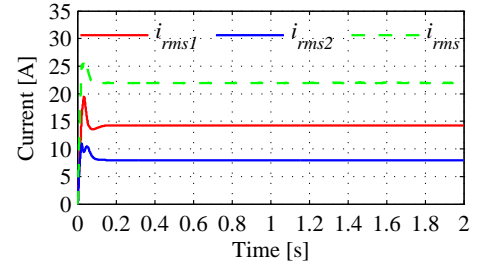
A master-slave architecture of an inverter system is presented which allows parallel operation of an arbitrary number of inverter modules by a simple control method. The simulation of master-slave mode was also carried out. The proposed control scheme was applied for Inverter 1 as the master mode. Inverter 2 is a synchronverter which means that Inverter 2 can track the master phase by a synchronisation unit and can also set the real power and reactive power references.

The simulation was started at  $t = 0\text{s}$ , with the Circuit breaker  $S$  off. At  $t = 1\text{s}$ , the Circuit breaker  $S$  was on and Inverter 2 was connected to the load. Meanwhile, the real power reference  $P_2$  was 1000W and the reactive power reference  $Q_2$  was zero. Then,  $P_2$  was changed to 1500W at  $t = 2\text{s}$  and  $Q_2$  was changed to 500Var at  $t = 3\text{s}$ . The system responses are shown in Figure 6.4. The parallel operation of two inverters performed very well. The real power and reactive power were accurately shared with  $P = P_1 + P_2$  and  $Q = Q_1 + Q_2$ .  $P_2$  tracked the reference very well and  $P_1$  shared the load automatically. The load voltage is stable and purely sinusoidal, even when the state of the inverters changed.

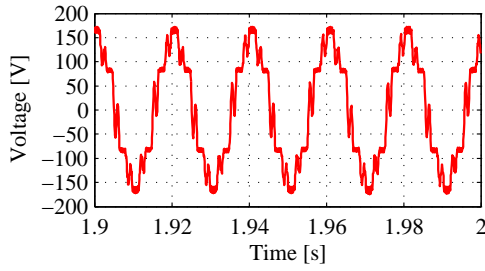
The current of Inverter 1, Inverter 2 and the load in different situations are shown in Figure 6.5. When Circuit breaker  $S$  was off, the current of Inverter 1  $i_1$  is exactly equal to the current of the load  $i$ . When  $P_2 = 1000\text{W}$  or  $P_2 = 1500\text{W}$ , the Inverter 1 current



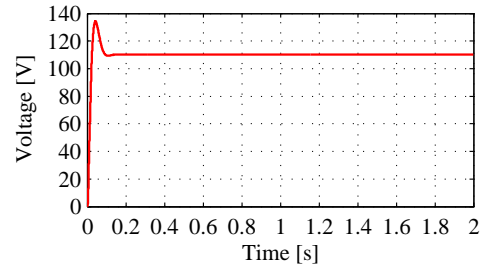
(a) Current  $i_1$ ,  $i_2$  and  $i$



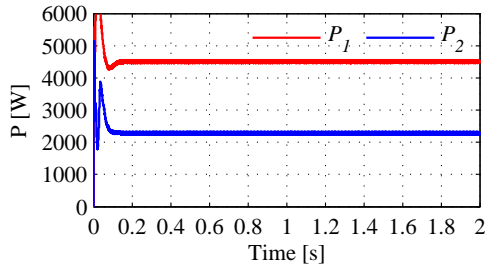
(b) RMS current  $i_{rms1}$ ,  $i_{rms2}$  and  $i_{rms}$



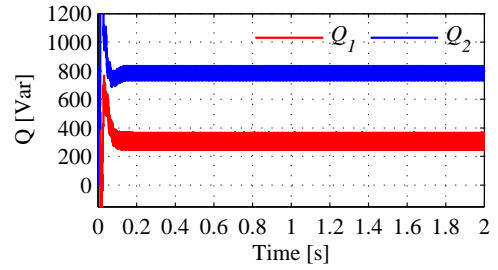
(c) Load voltage



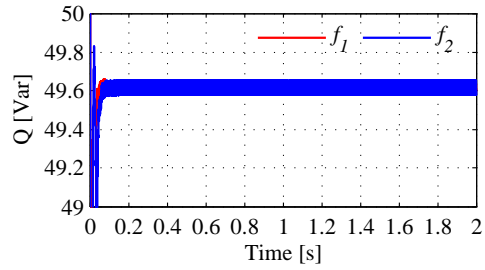
(d) RMS voltage of load



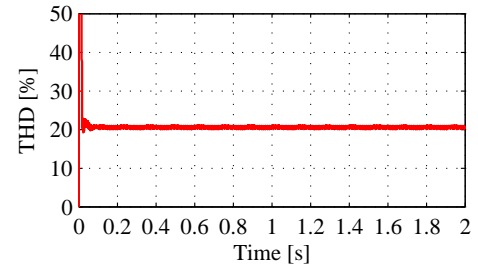
(e) Real power  $P_1$  and  $P_2$



(f) Reactive power  $Q_1$  and  $Q_2$

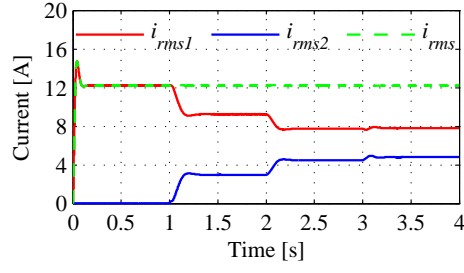


(g) Frequency  $f_1$  and  $f_2$

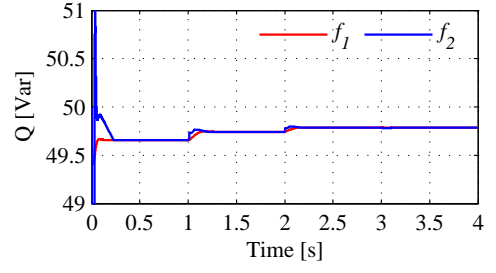


(h) THD of load voltage

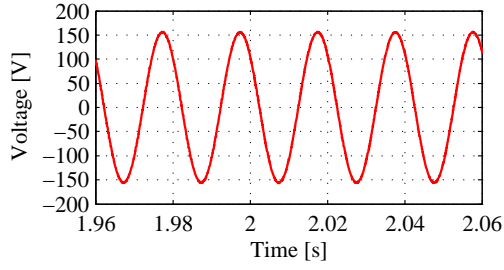
Figure 6.3: Simulation results with a nonlinear load



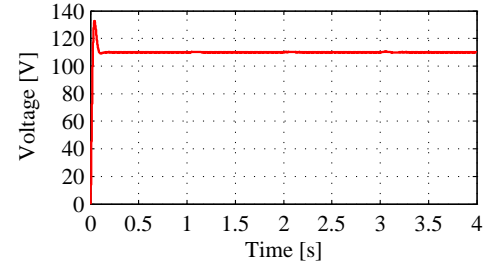
(a) RMS current  $i_{rms1}$ ,  $i_{rms2}$  and  $i_{rms}$



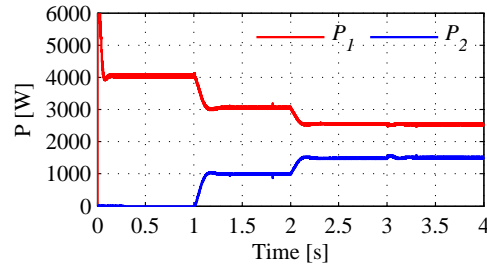
(b) Frequency  $f_1$  and  $f_2$



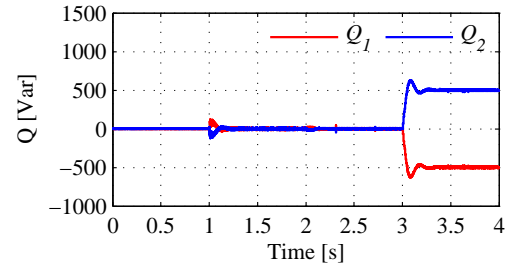
(c) Load voltage



(d) RMS voltage of load

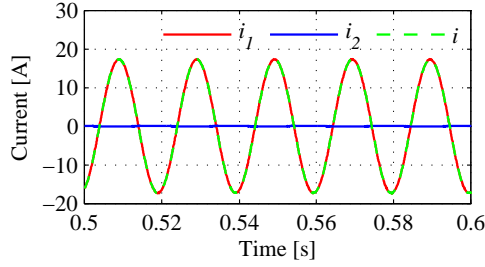


(e) Real power  $P_1$  and  $P_2$

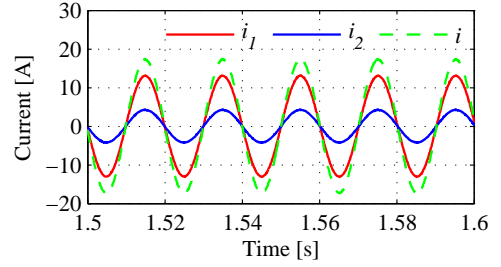


(f) Reactive power  $Q_1$  and  $Q_2$

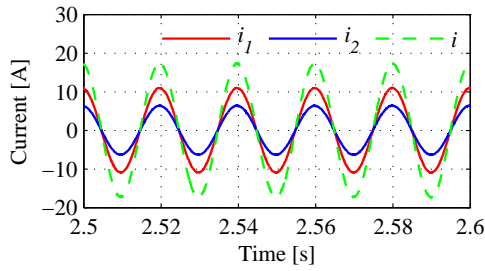
Figure 6.4: Simulation results in the master-slave mode with a linear load



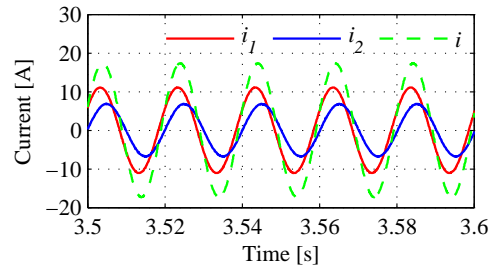
(a) When  $P_2 = 0$  W



(b) When  $P_2 = 1000$  W



(b) When  $P_2 = 1500$  W



(b) When  $Q_2 = 500$  Var

Figure 6.5: Current of inverter1, inverter2 and load

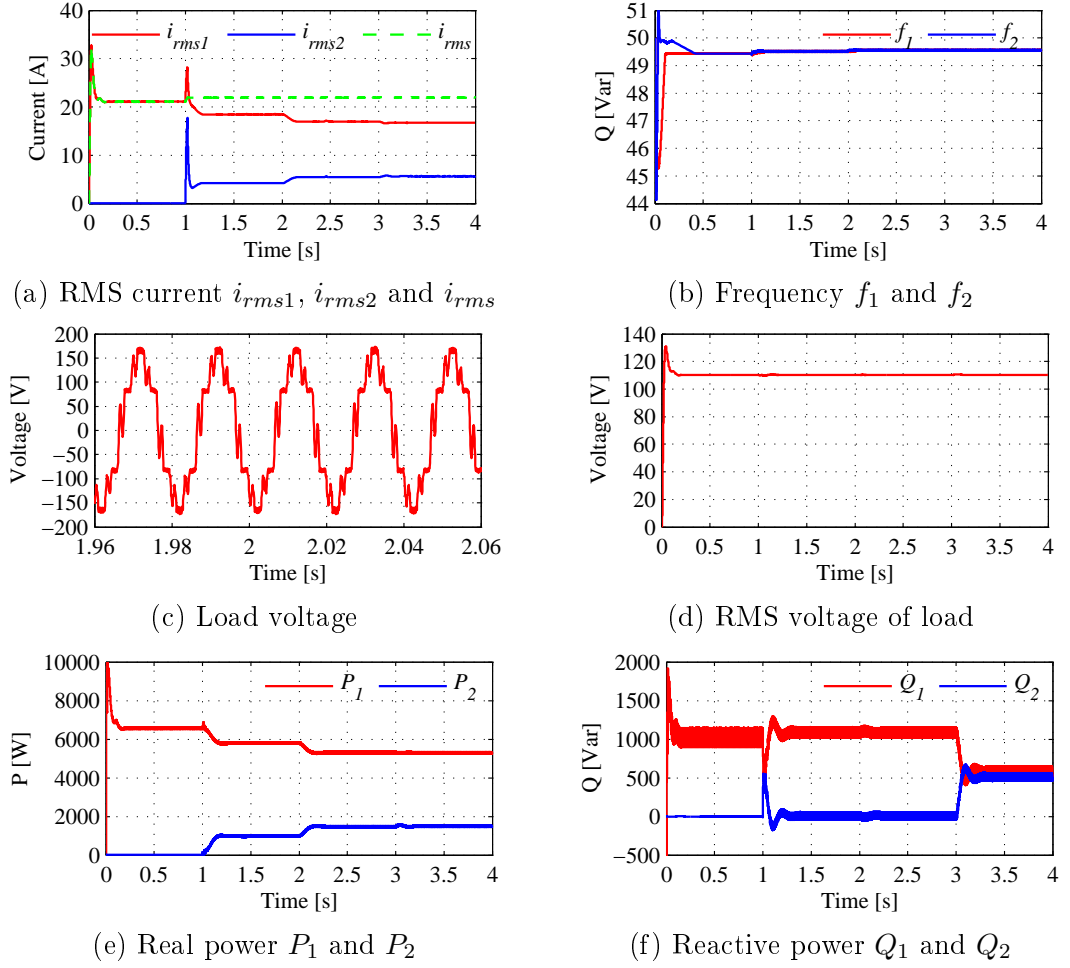
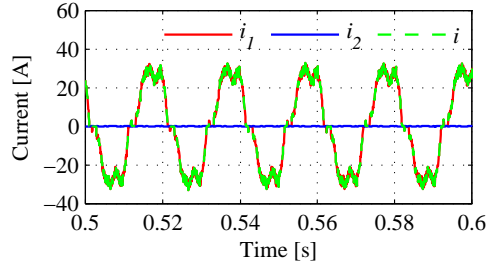


Figure 6.6: Simulation results in the master-slave mode with a nonlinear load

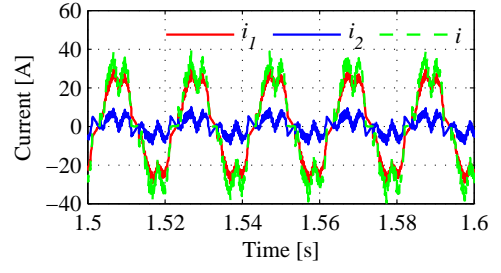
$i_1$  and the Inverter 2 current  $i_2$  are nearly sinusoidal and in phase with the load current  $i$ .  $i$  always remains constant even when  $i_1$  and  $i_2$  are changed. When  $Q_2 = 500\text{Var}$ , the Inverter 1 current  $i_1$  and the Inverter 2 current  $i_2$  have a clear phase shift with the load current  $i$  because  $Q_1$  and  $Q_2$  are changed.

#### 6.2.4 Master-slave mode with a nonlinear load

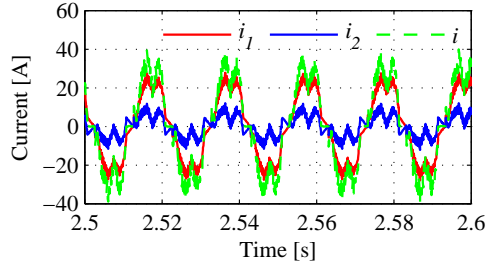
The simulation of master-slave mode was also carried out for a full-bridge rectifier load with an LC filter  $L = 150\mu\text{H}$ ,  $C = 1000\mu\text{F}$  and  $R = 9\Omega$ . The system responses are shown in Figure 6.6 and the current of Inverter 1, Inverter 2 and the load in different situations are shown in Figure 6.7.



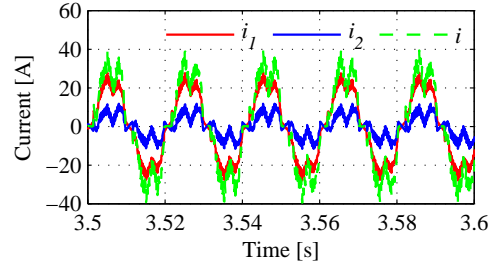
(a) When  $P_2 = 0$  W



(b) When  $P_2 = 1000$  W



(b) When  $P_2 = 1500$  W



(b) When  $Q_2 = 500$  Var

Figure 6.7: Current of inverter1, inverter2 and load

### 6.3 Conclusions

In this chapter, a controller based on synchronverters for parallel inverters in stand-alone mode has been proposed. The control strategy consists of a frequency droop loop and a voltage droop loop which allow the sharing of the real power and reactive power, respectively. Simulation results were provided to demonstrate the excellent performance.

## Chapter 7

# Synchronverters with Capacitive Output Impedances

Rapidly increasing energy consumption on one side and steadily reducing energy sources on the other side, lead to the need for a DPGS based on renewable energy sources, mainly from wind and solar energy [68, 69, 70]. They often form microgrids before being connected to the utility grid [41, 71, 72, 73]. One of the major problems with these applications is the quality of the microgrid voltage. For both wind turbines and photovoltaics connected to the grid, the maximum limit for the Total harmonic distortion of the output voltage is  $THD = 5\%$  according to industrial regulations [74, 75].

Several feedback control schemes, e.g. deadbeat or hysteresis controllers [76, 77], have been proposed for inverters to reduce THD. However, these controllers alone cannot eliminate the periodic distortion caused for example by nonlinear loads. Repetitive control theory [78, 79], which is regarded as a simple learning control method, provides an alternative for eliminating periodic errors in dynamic system, using the internal model principle [80]. Furthermore, some research has been done on active filters [81, 82] and grid-connected inverters [71, 74, 83].

The switching frequency of the PWM switching converter is usually a few kilohertz and high-order frequency harmonics are small in magnitude and can be removed by a filter. The filter is connected in parallel as an interface between the inverter and the grid [84, 85, 86, 87, 88]. The output filter, used to reduce harmonic currents injected into the grid or load, is a simple first order L filter. However, implementation of LC filters has been proposed to provide better harmonic attenuation and reduce the filter

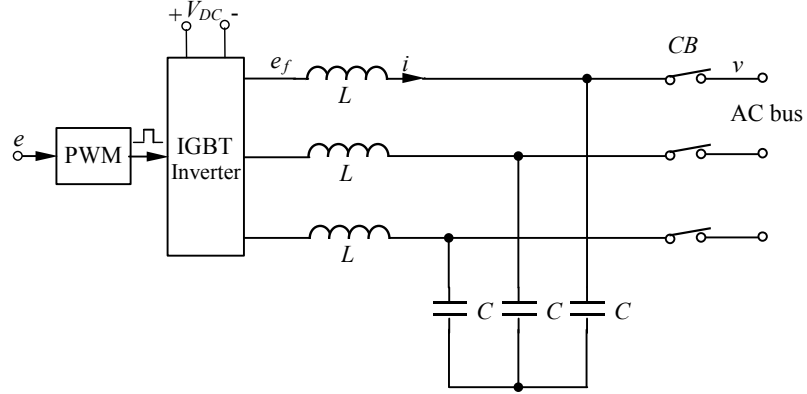


Figure 7.1: A descriptive circuit of a three-phase inverter.

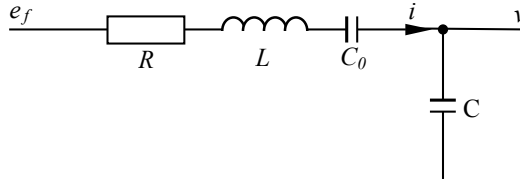


Figure 7.2: Single phase of LC filter.

size. In these cases, the inverter output impedance is inductive because of the output inductor and /or the highly inductive line impedance. In low-voltage applications, the line impedance is predominantly resistive. Since control strategies can be used to change the output impedance, it can be easily forced to be resistive, inductive, or other types. Arguably, it is better to force the output impedance to be resistive because its impedance does not change with the frequency, and the effect of nonlinear loads (harmonic current components) on the voltage THD can be compensated more easily.

## 7.1 Capacitive Output Impedances

Recently, the capacitive output impedance of an inverter was introduced and a strategy was proposed to force the output impedance of an inverter to be capacitive [89]. Both simulation and experimental results were provided to demonstrate that an inverter achieves a lower THD when it is designed to have a capacitive output impedance than when it is designed to have an inductive output impedance.

Figure 7.1 shows an inverter, which consists of a three-phase inverter powered by a DC source, and an LC filter. The control signal  $e$  is converted to a PWM signal to drive

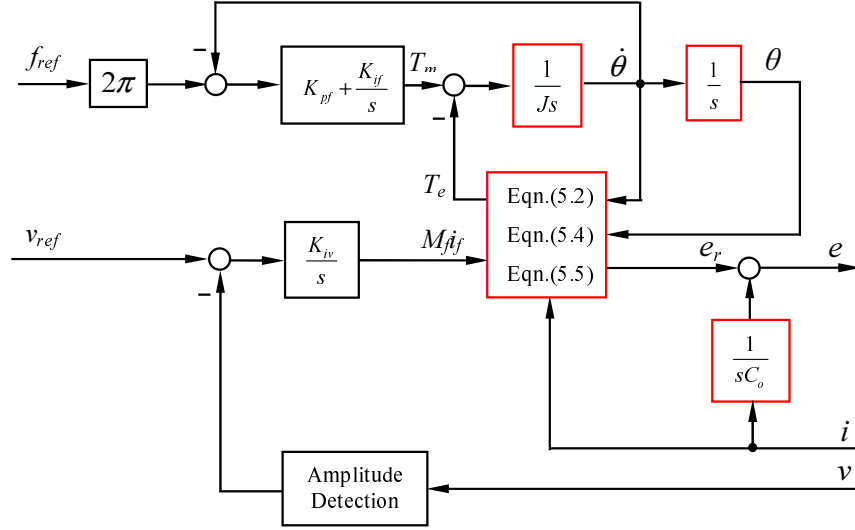


Figure 7.3: Control strategy based on synchronverters.

the inverter so that the average of  $e_f$  over a switching period is the same as  $e$ . Figure 7.2 shows the single phase of LC filter. The following equation is easily obtained,

$$e_f = (R + sL + \frac{1}{sC_0})i + v,$$

which gives

$$v = e_f - Z_o(s) \cdot i,$$

where the output impedance  $Z_o(s)$  is

$$Z_o(s) = R + sL + \frac{1}{sC_0}.$$

When  $R$  is bigger than  $sL + \frac{1}{sC_0}$ , the output impedance of the inverter can be treated as resistive. When  $sL$  is bigger than  $R + \frac{1}{sC_0}$ , the output impedance of the inverter can be treated as inductive. When  $\frac{1}{sC_0}$  is bigger than  $R + sL$ , the output impedance of the inverter can be treated as capacitive. Therefore, if the capacitor  $C_0$  is chosen to be small enough, the effect of the inductor ( $R + sL$ ) is not significant and the output impedance can be made to be nearly purely capacitive at the fundamental frequency, i.e., roughly

$$Z_o(s) \approx \frac{1}{sC_0}.$$



Table 7.1: Steady-state performance of the inverter with L=0.6mH.

	THD		<i>h</i> -th harmonics		
Type of $Z_o$	$e$	$v_o$	5th	7th	11th
L	0.1%	7.3%	0.9	0.33	0.26
$C_0(675\mu F)$	3.99%	5.98%	0.65	0.365	0.151
$C_0(510\mu F)$	5.3%	6%	0.79	0.32	0.16
$C_0(344\mu F)$	7.2%	6.7%	0.926	0.355	0.12

In [90], the optimal  $C_0$  was given as follows

$$C_0 = \frac{1}{(h\omega^*)^2 L}, \quad (7.1)$$

where  $\omega^*$  is the rated frequency. This forces the impedance at the  $h$ -th harmonic frequency to be 0 and hence no voltage at this frequency is caused.

The proposed control strategy is based on the idea of operating an inverter to mimic a synchronous generator [1, 40], as shown in Figure 7.3.  $T_m$  and  $M_{fi}$ , which were determined by the output frequency and amplitude respectively, are the control inputs of the synchronous generator. A PI controller and an I controller were applied in the  $T_m$  loop and  $M_{fi}$  loop to regulate output frequency and amplitude, respectively. The inductor current  $i$  is measured for feedback by an integrator block  $\frac{1}{sC_0}$  so that the output impedance of the inverter is forced to be capacitive. This is equivalent to having a virtual capacitor  $C_0$  connected in series with the filter inductor  $L$ .

## 7.2 Simulation Results

To study the operation of the control strategy described above, simulations have been carried out on a three-phase inverter powered by a 42V DC voltage supply in Matlab7.6/ Simulink/ SimpowerSystems. The solver used in the simulations was ode23t with a relative tolerance of  $10^{-3}$  and the sampling time was  $10 \mu s$ . The switching frequency is 7.5kHz and the frequency of the system is 50Hz. The rated output voltage is 12V. The filter capacitance is  $22\mu F$  and the load is a full-bridge rectifier loaded with an LC filter  $L = 150\mu H$ ,  $C = 1000\mu F$  and  $R_L = 9\Omega$ .

### 7.2.1 The case with $L = 0.6mH$

It is well known that there is no need to take  $3 \cdot n$ -th ( $n=1,2,\dots$ ) harmonics components into account in the three-phase system. According to Equation (7.1), the optimal capacitance  $C_0$  can be chosen as  $675\mu F$ ,  $510\mu F$  and  $344\mu F$  to minimise the effect of the 5th, 7th and 11th harmonics in  $v_o$ , respectively. The steady-state performance of the system with these controllers are shown in Table 7.1. When the inverter has inductive output impedance, the control signal  $e$  is very clean (with low THD 0.1%), but the output voltage  $v_o$  has the highest THD because of high 5th, 7th and 11th harmonics components. From this Table 7.1, the lowest 5th harmonics component (0.65) was obtained when the capacitor was designed as  $C_0 = 675\mu F$  to minimise the effect of the 5th harmonics. The same situations occurred with the 7th and 11th harmonics. In this case, the control signal  $e$  became worse because of the feedback of  $i$ . Nevertheless, the THD of output voltage  $v_o$  was better because of the compensation of feedback to eliminate the periodic errors. Based on the same argument, the lowest THD (5.98%) of the output voltage  $v_o$  was obtained when the capacitor was designed as  $C_0 = 675\mu F$  to minimise the effect of the 5th harmonics.

The output voltage, the THD of the output voltage and the current curves for the inverters with different output impedances are shown in the left, middle and right columns of Figure 7.4, respectively. Obviously, the inverter achieves a lower THD when it is designed to have a capacitive output impedance than when it is designed to have an inductive output impedance. Moreover, other techniques, e.g. the ones proposed in [91, 92], can be applied to further decrease the THD to meet industrial regulations.

### 7.2.2 The case with $L = 0.15mH$

Table 7.2: Steady-state performance of the inverter with  $L=0.15mH$ .

	THD		$h$ -th harmonics		
Type of $Z_o$	$e$	$v_o$	5th	7th	11th
L	0.1%	7.25%	0.306	0.295	0.135
$C_0(2700\mu F)$	2%	6.85%	0.127	0.185	0.16
$C_0(1400\mu F)$	4.1%	6.69%	0.32	0.102	0.148
$C_0(558\mu F)$	5.9%	7.74%	0.605	0.345	0.066

In this case, the filter inductor  $L=0.6mH$  was replaced with an inductor  $L=0.15mH$  and the parasitic resistance of the inductor was assumed to be  $0.045\Omega$ . The optimal

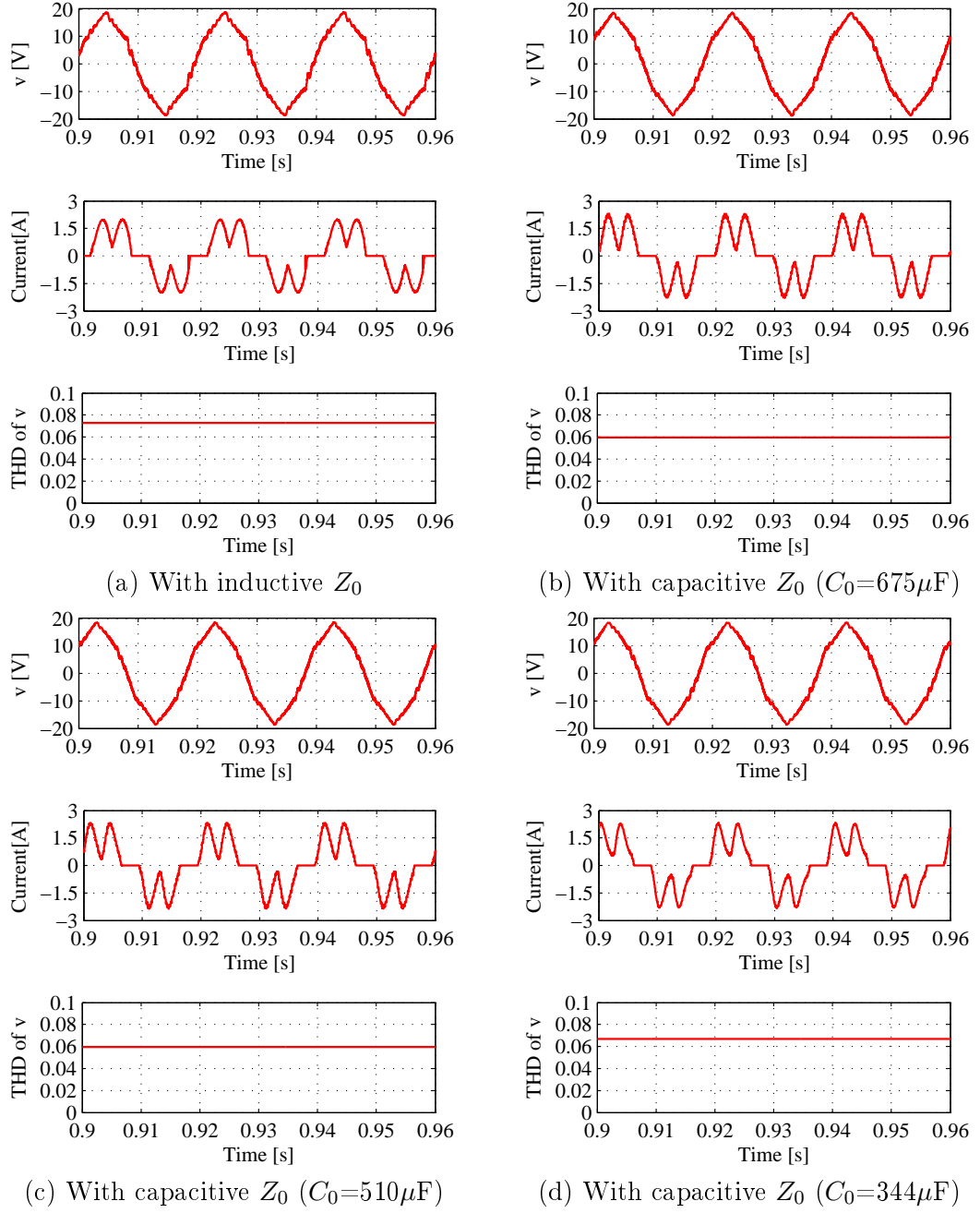


Figure 7.4: Simulation results for the case with  $L=0.6$  mH: output voltage, current, and THD of the output voltage.

capacitance  $C_0$  can be chosen as  $1600\mu F$ ,  $1200\mu F$  and  $827\mu F$  to minimise the effect of the 5th, 5th+7th and 7th harmonics in  $v_o$ , respectively. The steady-state performances of the system with these controllers are shown in Table 7.2. The best THD (16.7%) was obtained when the capacitor was designed to minimise the effect of the 5th+7th harmonics as  $C_0=1200\mu F$ . The output voltage, the THD of the output voltage and the current curves for the inverters with different output impedances are shown in the left, middle and right columns of Figure 7.5, respectively.

### 7.3 Experimental Results

Experiments were also carried out in the stand-alone mode, as shown in Figure 7.6, to further demonstrate the control strategy. The experimental setup consists of a 42V DC voltage supply, an inverter board, a LC filter, a board consisting of voltage and current transducers, a full-bridge rectifier loaded with an LC filter  $L = 150\mu H$ ,  $C = 1000\mu F$  and  $R_L = 9\Omega$ , a dSPACE DS1104 R&D controller board with ControlDesk software and MATLAB Simulink/SimPower software package. The sampling frequency of the controller was 5 kHz and the switching frequency was 10 kHz. Two cases were tested: one with  $L = 0.6$  mH and the other with  $L = 0.15$  mH.

#### 7.3.1 The case with $L = 0.6mH$

The experimental results when the inverter was designed to have different types of output impedance are shown in Figure 7.7. The experimental results are similar to the simulation ones, but the effect of the THD reduction is not remarkable. However, the improvement can still be noticed.

#### 7.3.2 The case with $L = 0.15mH$

The experimental results when the inverter was designed to have different types of output impedance are shown in Figure 7.8. When the inverter was designed to have a capacitive output impedance to minimise the effect of the 7th harmonics, the best result was obtained. The THD was improved by about 1% from the case with an inductive output impedance.

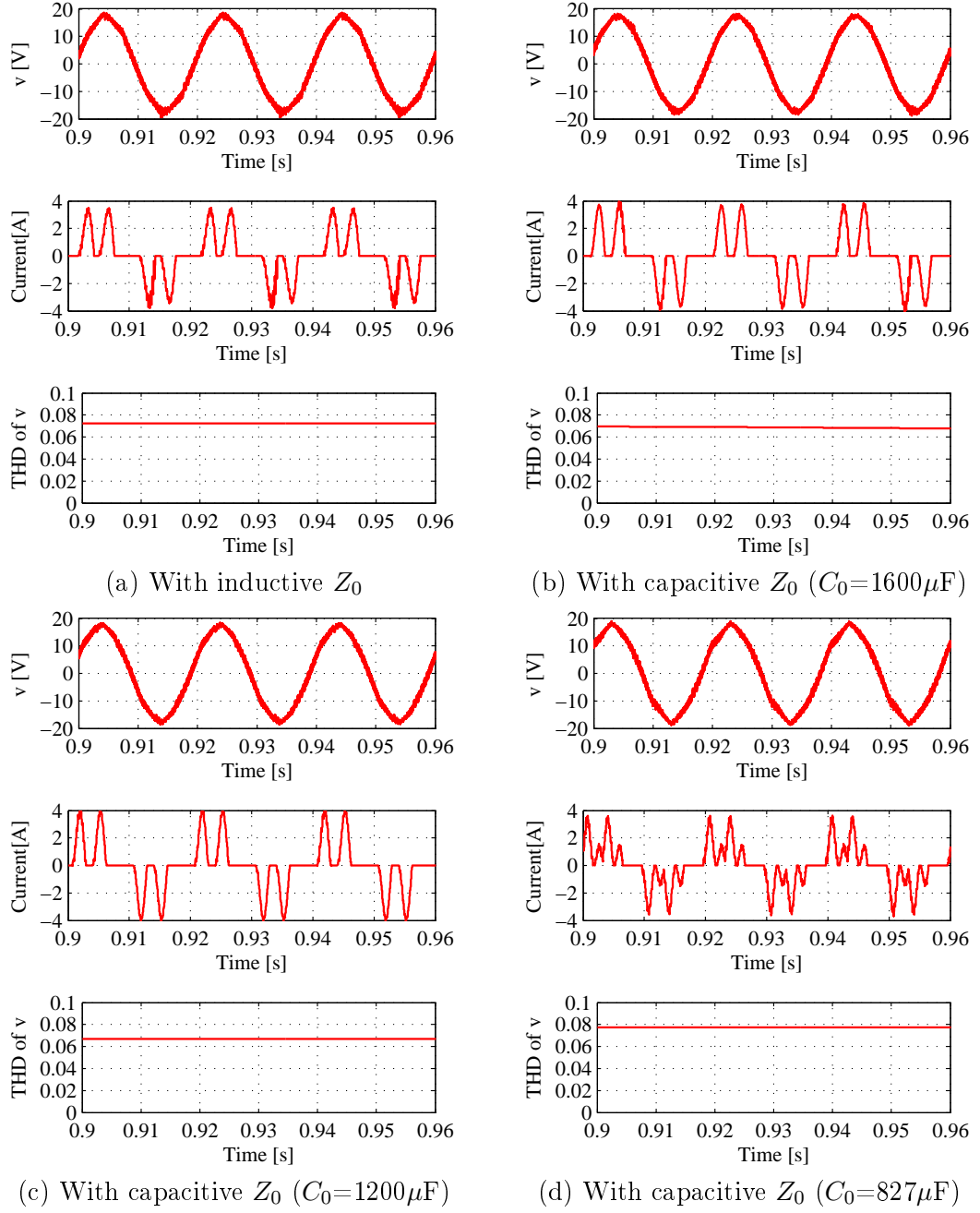


Figure 7.5: Simulation results for the case with  $L=0.15\text{mH}$ : output voltage, current and THD of the output voltage.

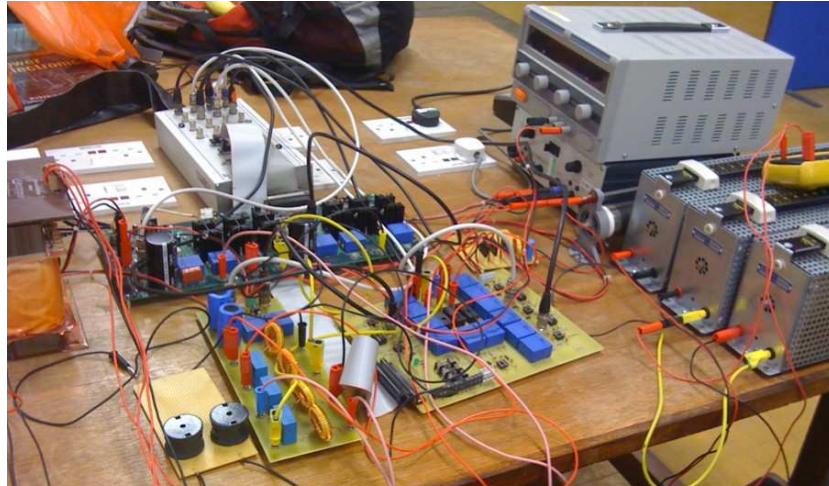


Figure 7.6: The experimental setup

## 7.4 Conclusions

In this chapter, a synchronverter-based control strategy which introduced a current feedback was presented to force the output impedance of the inverter to be capacitive. Both simulation and experimental results were provided to demonstrate that an inverter achieves a lower THD when it is designed to have a capacitive output impedance than when it is designed to have an inductive output impedance.

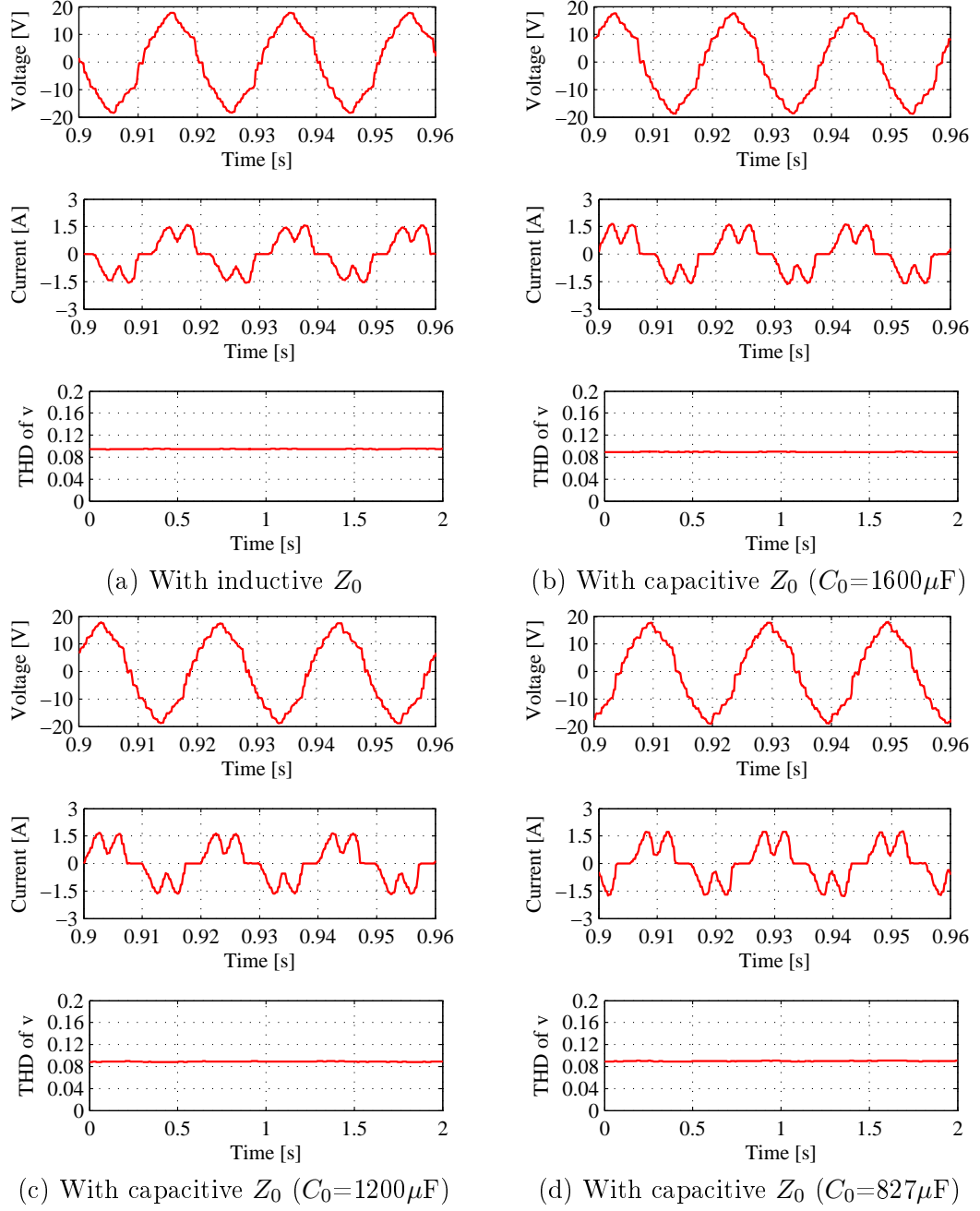


Figure 7.7: Experimental results for the case with  $L=0.6\text{mH}$ : output voltage, current and THD of the output voltage.

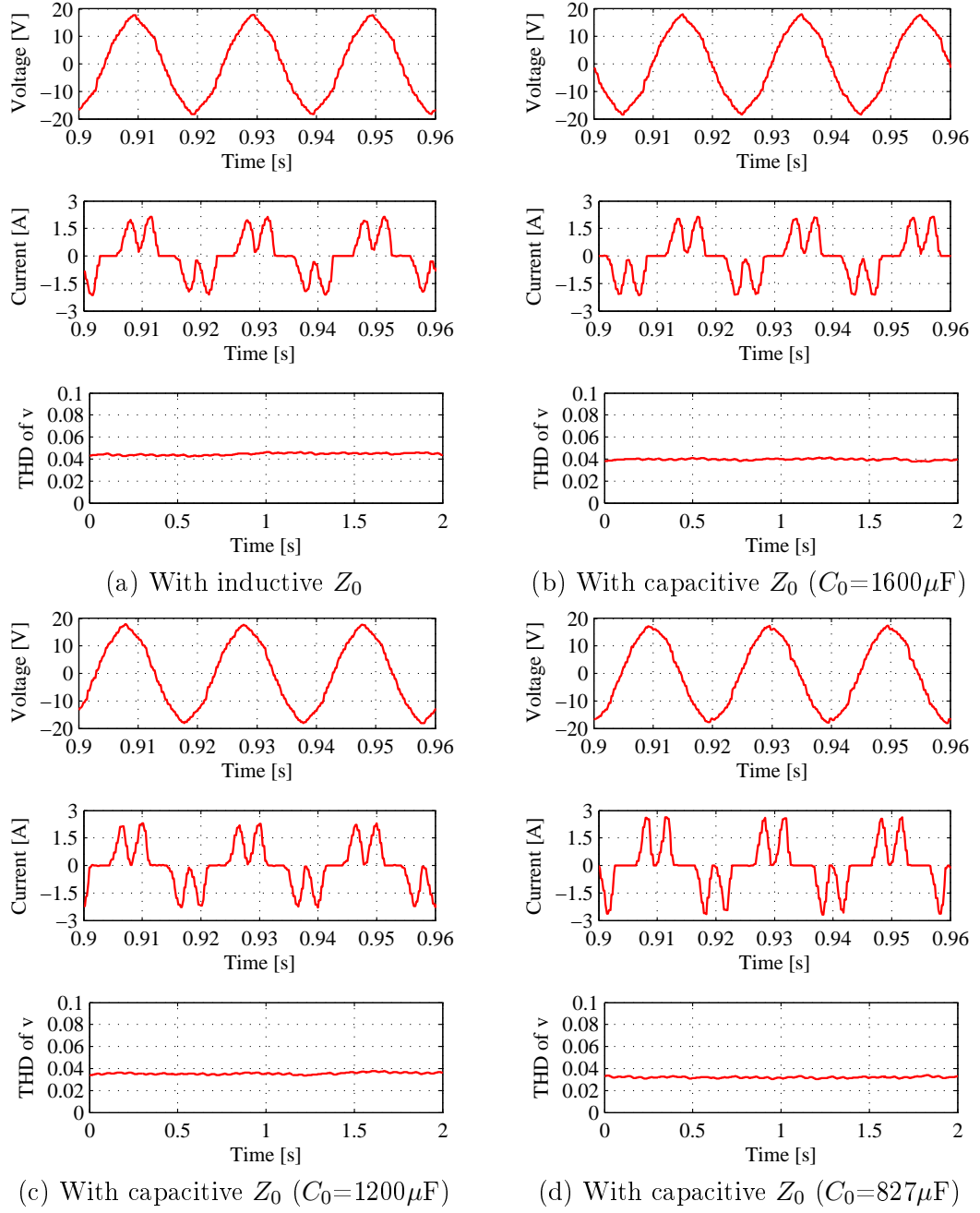


Figure 7.8: Experimental results for the case with  $L=0.15\text{mH}$ : output voltage, current and THD of the output voltage.



## Chapter 8

# Synchronverters Operated as Rectifiers

Most three-phase rectifiers use a diode bridge circuit and a bulk storage capacitor. This has the advantage of being simple, robust and low cost. However, it allows only unidirectional power flow. Moreover, the energy returned from the motor must be dissipated on the power resistor controlled by a chopper connected across the DC bus. The diode input circuit also results in a lower power factor and a high level of harmonic input currents. The voltage source PWM rectifier is increasingly used in industrial DC power supplies, motor drives, and a common DC bus for multiple drives [93]. PWM rectifiers are well known for their advantages and merits compared to uncontrolled diode rectifiers e.g. lower THD factor, Power Factor correction, regenerative operation and Active Filtering capabilities [94, 95].

Figure 8.1 presents the most popular topology used in the ASD system for induction machines, UPS and AC-excited induction generator drive systems utilise the bidirectional AC-DC-AC power converters.  $L_s$  and  $R_s$  represent the line impedance. It brings the current source character of the input circuit and provides the boost feature of converters.

Various strategies have been proposed to control PWM rectifiers. These strategies can achieve the same major goals, such as a high power factor and near-sinusoidal current waveforms, but they are often based on different principles. In particular, the VOC, which uses closed-loop current control in a rotating reference frame, offers good dynamic and static performance. It has become very popular and has constantly been developed and improved [96, 97, 98, 99]. The configuration and performance of the VOC system largely depends on the quality of the applied current control strategy

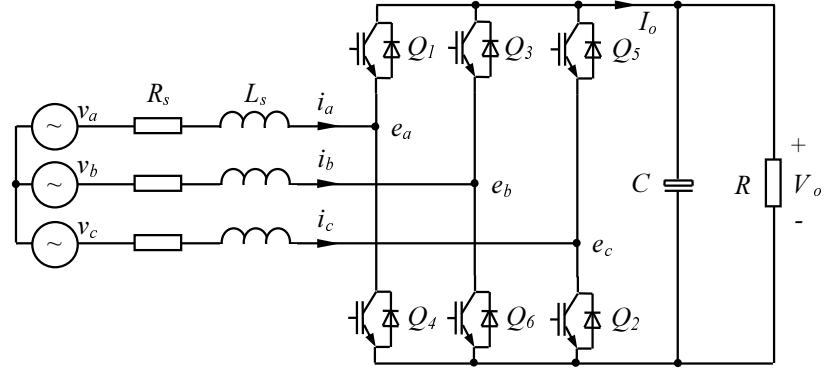


Figure 8.1: Representation of three-phase voltage source PWM rectifier.

which normally consists of an inner high bandwidth current control loop and an outer low bandwidth DC bus voltage regulation loop [100]. The current controller controls the input line current to track the reference to ensure the unity power factor operation and the power balance on the output of the rectifier. The DC bus voltage regulator indirectly regulates the power fed into the rectifier to realise the constant DC bus voltage control [101, 102, 103].

DPC adopts instantaneous real and reactive power control loops to control the power directly, without using inner current loops, by using hysteresis control. No PWM block is needed because the states of the converter switches are selected from a table based on the instantaneous errors between the set-point and the measured values of real and reactive power [104, 105, 106, 107, 108, 109]. This leads to a variable switching frequency. It is difficult to implement in industry because of the variable switching frequency and the high sampling frequency needed for digital implementation.

In this chapter, two control strategies are proposed to operate a rectifier to mimic a synchronous motor, following the idea of operating inverters to mimic synchronous generators [1]. This allows the use of a PWM block to convert the voltage into PWM signals to drive the rectifier switches and, hence, the switching frequency is fixed. Moreover, the line currents can be made sinusoidal and good dynamics can be achieved.

## 8.1 Direct Power Control

The principle of DPC was first introduced in [104] where an optimum switching table was defined for the demands of real or reactive power as a function of the power source

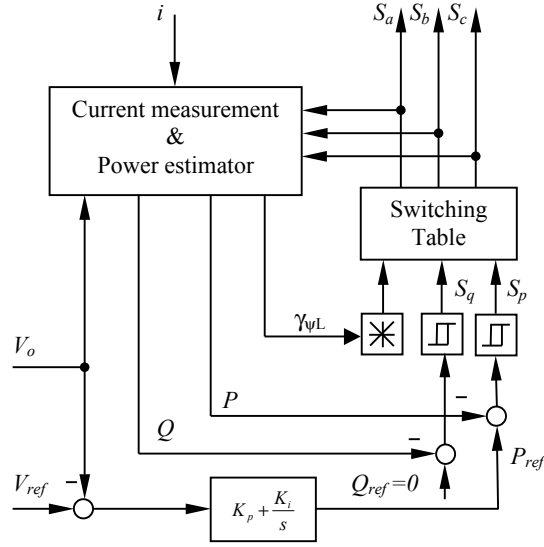


Figure 8.2: Conventional DPC.

voltage angle. [105] proposed the use of a PWM controlled switched rectifier using the virtual flux signal for power estimation without voltage sensors. Therefore, the most important thing in this paper is a correct and fast estimation of the real and reactive power. The real power  $P$  and reactive power  $Q$  can be defined as

$$P = L_s \left( \frac{di_a}{dt} i_a + \frac{di_b}{dt} i_b + \frac{di_c}{dt} i_c \right) + V_o (S_a i_a + S_b i_b + S_c i_c),$$

$$Q = \frac{1}{\sqrt{3}} \{ 3L_s \left( \frac{di_a}{dt} i_c - \frac{di_c}{dt} i_a \right) - V_o [S_a (i_b - i_c) + S_b (i_c - i_a) + S_c (i_a - i_b)],$$

where  $i_a, i_b, i_c$  are three phase line currents;  $S_a, S_b, S_c$  are the switching states of the converter;  $V_o$  is the DC bus voltage. The basic block diagram of DPC is shown in Figure 8.2.

The reference of real power  $P_{ref}$  (delivered from the outer PI-DC voltage controller) and reactive power  $Q_{ref}$  (set to zero for unity power factor) are compared with the estimated  $P$  and  $Q$  values (line voltage or virtual flux), in real and reactive power hysteresis controllers, respectively.

The digitised output signals of the real and reactive power controllers are defined as

$$S_p = \begin{cases} 1 & P < P_{ref} - H_p \\ 0 & P > P_{ref} + H_p \end{cases},$$

$$S_q = \begin{cases} 1 & Q < Q_{ref} - H_q \\ 0 & Q > Q_{ref} + H_q \end{cases},$$

where  $H_p$  and  $H_q$  are the hysteresis bands.

The digitised variables  $S_p$ ,  $S_q$  and the flux vector position  $\gamma_{\psi L} = \arctan(\frac{\psi_{L\alpha}}{\psi_{L\beta}})\gamma_{\psi L}$ , which, by accessing the address of the look-up table, select the appropriate voltage vector according to the switching table[104].

The region of the voltage or flux vector position is divided into twelve sectors and the sectors can be numerically expressed as

$$\frac{(n-2)\pi}{6} \leq \gamma \leq \frac{(n-1)\pi}{6},$$

where,  $n=1,2,\dots,12$ .

However, superimpositions of the disturbances on the line voltage have direct influences on the line voltage vector position in the control system. Sometimes, this kind of problem can be overcome by phase-locked loops only, but the quality of the controlled system depends on the effectiveness of PLL design.

## 8.2 Modeling of a Synchronous Motor

A three-phase PWM bridge rectifier is shown in Figure 8.3. Inductors  $L_s$  with equivalent series resistance  $R_s$  are connected between the rectifier and the source to reduce the current harmonics. Assume that the field and the three identical stator windings are distributed in slots around the periphery of the uniform air gap. The stator windings can be regarded as concentrated coils having self-inductance  $L$  and mutual inductance  $-M$  ( $M > 0$ , the negative sign is due to the  $\frac{2\pi}{3}$  phase angle). In this chapter, the model of a synchronous motor presented in [1] is adopted because the model for a generator or a motor is more or less the same, apart from the direction of the stator current is defined as opposite.

Denote the flux vector and the current vector as

$$\Phi = \begin{bmatrix} \Phi_a \\ \Phi_b \\ \Phi_c \end{bmatrix}, \quad i = \begin{bmatrix} i_a \\ i_b \\ i_c \end{bmatrix}$$

respectively, and

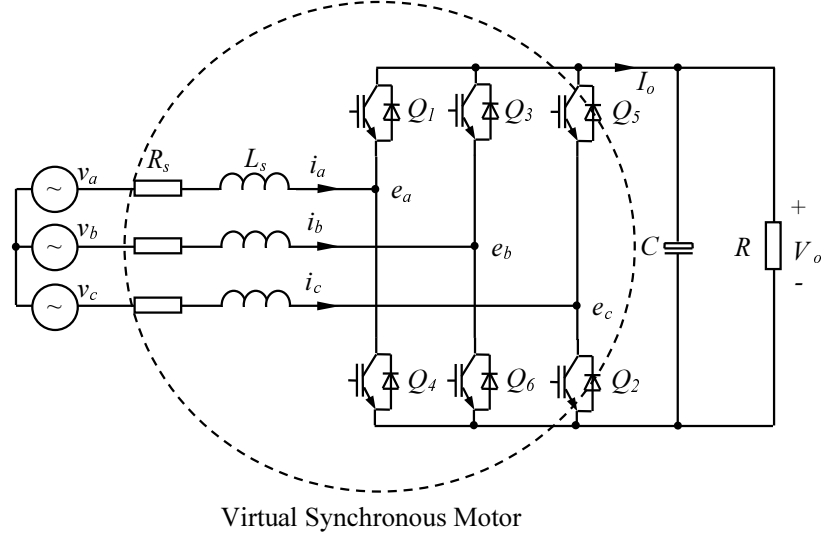


Figure 8.3: PWM rectifier treated as a virtual synchronous motor.

$$\widetilde{\cos\theta} = \begin{bmatrix} \cos\theta \\ \cos(\theta - \frac{2\pi}{3}) \\ \cos(\theta - \frac{4\pi}{3}) \end{bmatrix}, \quad \widetilde{\sin\theta} = \begin{bmatrix} \sin\theta \\ \sin(\theta - \frac{2\pi}{3}) \\ \sin(\theta - \frac{4\pi}{3}) \end{bmatrix},$$

where  $\theta$  is the rotor angle with respect to the Phase A winding.

Assume that the resistance of the stator windings is  $R_s$ , then the phase terminal voltages  $v = [v_a \ v_b \ v_c]^T$  can be written as

$$v = e + R_s i + L_s \frac{di}{dt}, \quad (8.1)$$

where  $L_s = L + M$  and  $e = [e_a \ e_b \ e_c]^T$  is the back EMF due to the rotor movement given by

$$e = M_f i_f \dot{\theta} \widetilde{\sin\theta} - M_f \frac{di_f}{dt} \widetilde{\cos\theta}. \quad (8.2)$$

The voltage vector  $e$  is also called the no-load voltage, or synchronous internal voltage.

For the mechanical part, there is

$$\ddot{\theta} = \frac{1}{J}(T_e - T_m - D_p \dot{\theta}), \quad (8.3)$$

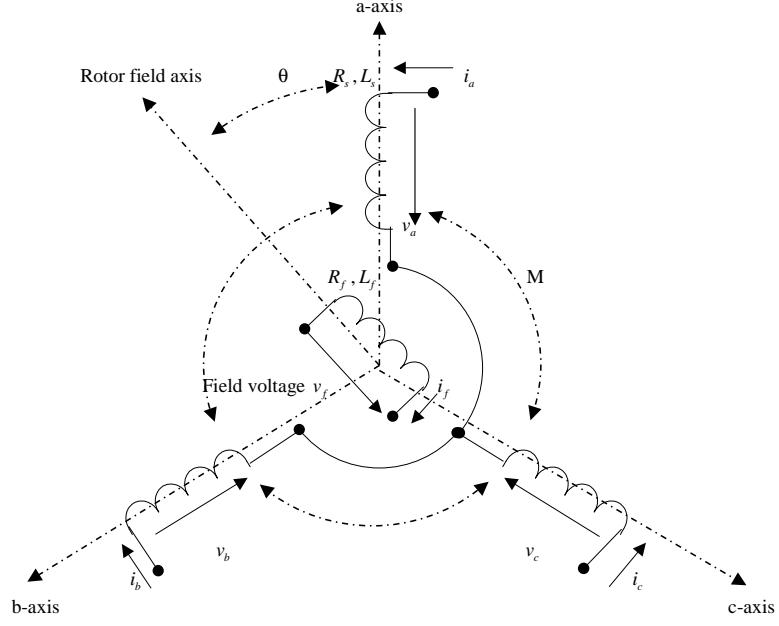


Figure 8.4: Structure of an idealized three-phase round-rotor synchronous motor.

where  $J$  is the moment of inertia of all the parts rotating with the rotor;  $D_p$  is a damping factor;  $T_m$  is the mechanical torque and  $T_e$  is the electromagnetic torque

$$T_e = M_f i_f \langle i, \widetilde{\sin \theta} \rangle, \quad (8.4)$$

where  $\langle \cdot, \cdot \rangle$  denotes the conventional inner product in  $\mathbb{R}^3$ .

Define the generated real power  $P$  and reactive power  $Q$  as

$$P = v_a i_a + v_b i_b + v_c i_c, \quad (8.5)$$

$$Q = \frac{1}{\sqrt{3}} [(v_b - v_c) i_a + (v_c - v_a) i_b + (v_a - v_b) i_c]. \quad (8.6)$$

The model can be described with the block diagram shown in Figure 8.5. Thus, the state variables of the synchronous motor are  $i$  (the inductor currents),  $\theta$  and  $\dot{\theta}$  (which

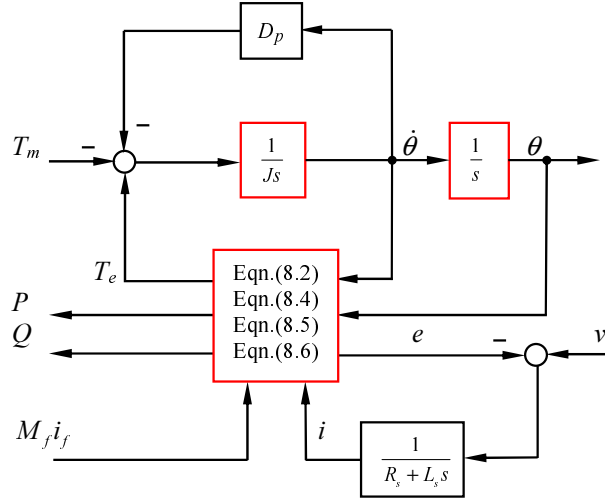


Figure 8.5: The model of a synchronous motor.

are a virtual angle and a virtual angular speed).  $T_m$  and  $M_f i_f$  are the control inputs of the synchronous motor. The control strategy will be discussed in the next section.

### 8.3 Proposed Strategy

The STA, which is the basic component of the proposed controller for synchronisation, is explained in subsection A. The proposed methodology of DPC, which is based on the virtual synchronous motor, is explained in subsection B. The proposed strategy to control the output voltage is described in subsection C and some applications are given in subsection D.

#### 8.3.1 STA

In order for the strategy to work properly, the frequency  $\dot{\theta}$  inside the rectifier should be the same as, or very close to the grid frequency  $\dot{\theta}_g$ . Before the rectifier is connected to the power source, its phase  $\theta$  should be kept the same as that of the grid in order to minimise the settling time when connecting it to the grid. This can be achieved by measuring the phase of the grid, e.g. via a phase-locked loop. In this control strategy, STA [110] is adopted to generate a signal to reset the integrator and the grid frequency.

A nonstationary sinusoidal  $y(t)$  can be expressed as

$$y(t) = A(t) \sin(\int^t \omega(\tau) d\tau + \delta(t)),$$

where  $A(t)$  and  $\omega(t)$  are the time-varying amplitude and the angular frequency of the sinusoidal component, respectively. The variable  $\delta(t)$  is the initial phase which is normally of a fixed value, but is assumed to be time-varying to include the cases where the phase has abrupt changes independent of its frequency. The total phase can be derived by

$$\phi(t) = \int^t \omega(\tau) d\tau + \delta(t).$$

The frequency can be calculated according to the angular frequency  $\omega(t)$  by

$$f(t) = \frac{\omega(t)}{2\pi}.$$

In order to estimate a sinusoidal component  $y(t)$  of a given signal  $u(t)$ , three variables  $A(t)$ ,  $\omega(t)$  and  $\phi(t)$  need to be estimated. The estimated values of amplitude  $\dot{A}(t)$ , frequency  $\dot{\omega}(t)$  and phase  $\dot{\phi}(t)$  are described according to the sinusoid-tracking algorithm by the following differential equations[110]:

$$\begin{aligned} \frac{d\dot{A}(t)}{dt} &= \mu_1 e(t) \sin \dot{\phi}(t), \\ \frac{d\dot{\omega}(t)}{dt} &= \mu_2 e(t) \dot{A}(t) \cos \dot{\phi}(t), \\ \frac{d\dot{\phi}(t)}{dt} &= \dot{\omega}(t) + \mu_3 \frac{d\dot{\omega}(t)}{dt}, \end{aligned}$$

where the dot on top represents the differentiation with respect to time.

$y(t)$  can be expressed as

$$y(t) = \dot{A}(t) \sin \dot{\phi}(t),$$

and the error signal  $e(t)$  is

$$e(t) = u(t) - y(t).$$

The parameters  $\mu_i$  ( $i=1, 2, 3$ ) are the controlling parameters of the algorithm which determine the convergence speed and the accuracy of the algorithm in tracking the variations in the amplitude and frequency.

Figure 8.6 shows the block diagram of the sinusoid-tracking algorithm. The algorithm finds the sinusoidal component of the input signal, which has the closest frequency to its initial value.





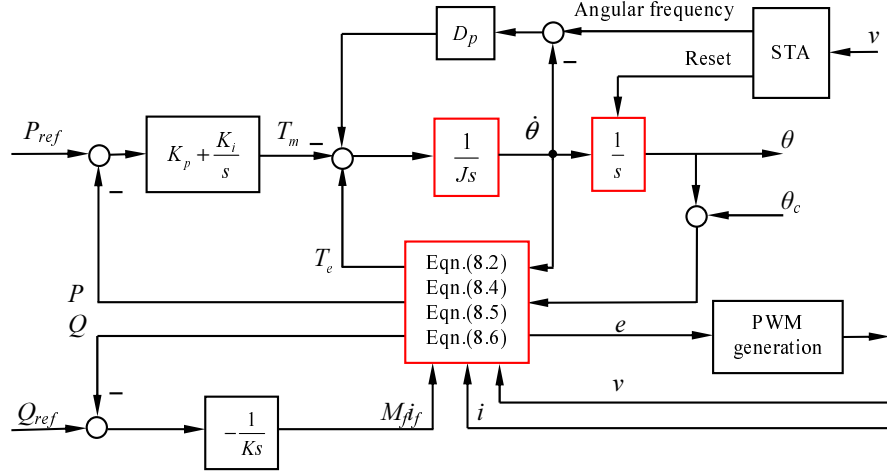


Figure 8.7: Proposed DPC.

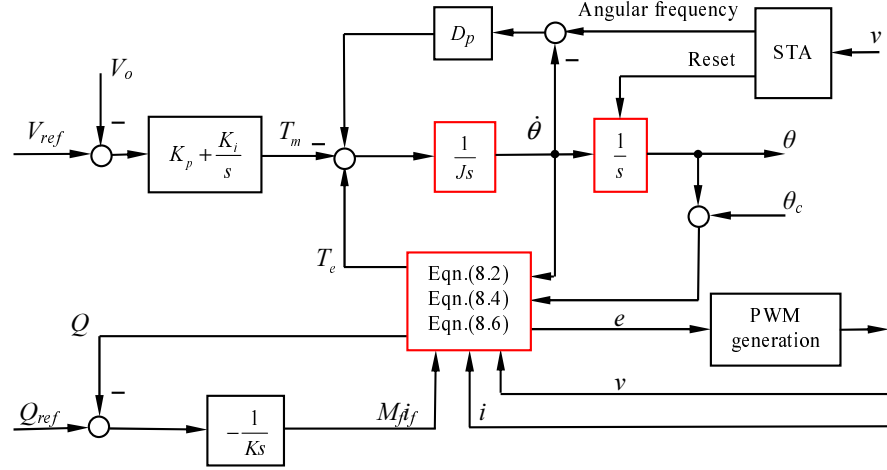


Figure 8.8: Proposed control strategy to maintain the DC bus voltage.

### 8.3.3 Proposed strategy to control the output voltage

The important application of PWM rectifiers is to provide a constant DC bus voltage. The control strategy to achieve this is shown in Figure 8.8. The outer-loop controller regulating the real power in Figure 8.7 is replaced with one to regulate the DC bus voltage. The error between the voltage reference  $V_{ref}$  and the measured voltage  $V_o$  is fed into the PI controller to generate the virtual torque  $T_m$ .

Table 8.1: Parameters used in the simulation.

Parameters	Values	Parameters	Values
$L_s$	4 mH	$R_s$	0.135 $\Omega$
nominal voltage	110 Vrms	switch frequency	5k Hz
$J$	0.0405 $kgm^2$	$C$	3300 $\mu F$
Pole pairs	1	$K$	114

### 8.3.4 Applications of the two proposed strategies

From the analysis above, the difference between the two proposed strategies is the control objective: one is the real power and the other is the output voltage. Actually, a certain output voltage means a certain real power for a certain DC load. Therefore, the two strategies are the same in essence to a certain extent. For a DC distribution system, or other applications requiring the fixed DC bus voltage, the output voltage can be controlled to level the DC bus voltage. On the other hand, the proposed strategy for the DPC can be employed when a certain stand-alone DC load is connected, or the rectifier is connected to the AC utility grid functioning as the reactive power compensator in which a variable DC bus voltage is acceptable.

For example, if the DC load abruptly increases/decreases in a DC distribution system, then the output voltage will decrease/increase accordingly. With the proposed strategy to control the output voltage, the real power extracted from the AC source is indirectly controlled to increase/decrease in order to balance the transferred power in the DC distribution system. Therefore, the output-voltage control strategy can be considered as an indirect or particular type of the real-power control strategy.

## 8.4 Simulation Results

To study the operation of the control strategy described above, the PWM rectifier with the whole DPC control scheme has been simulated in Matlab7.6/ Simulink/ Simpower-Systems. The solver used in the simulations was ode23t with a relative tolerance of  $10^{-3}$  and the sampling time was 10  $\mu s$ . The parameters of the rectifier used in the simulation are given in Table 9.1. The frequency regulation coefficient is chosen as  $D_p = 6.0793$ .

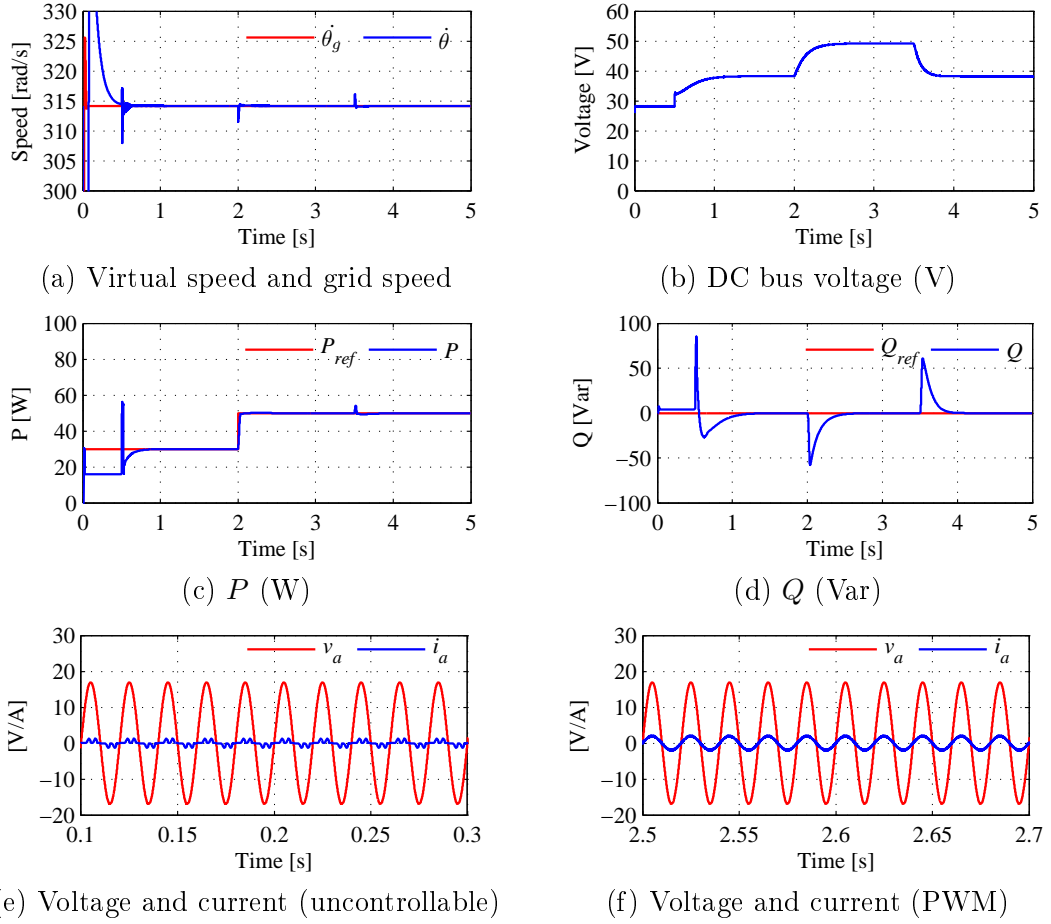


Figure 8.9: Simulation results with the nominal grid frequency.

#### 8.4.1 DPC

The simulation was started at  $t = 0$ . An STA was used for the initial synchronisation at the first 0.5 second. During this time, the PWM rectifier worked as an uncontrollable rectifier. The reactive power reference  $Q_{ref}$  was set to zero to obtain the unity power factor. Initially, the real power reference  $P_{ref}$  was 30W and the load  $R$  was  $50\Omega$ . The real power reference was increased to  $P_{ref} = 50\text{W}$  at  $t = 2\text{s}$  and the load was changed to  $R = 30\Omega$  at  $t = 3.5\text{s}$ . In this simulation,  $K_p = 0.05$  and  $K_i = 0.5$  are proportional and integral gains for a PI controller of the real power loop, respectively.

The system responses are shown in Figure 8.9. The virtual angular speed  $\dot{\theta}$  tracked the grid angular speed  $\dot{\theta}_g$  very well before the connection. There were small transient responses at the connection time, but they quickly settled down after the connection.

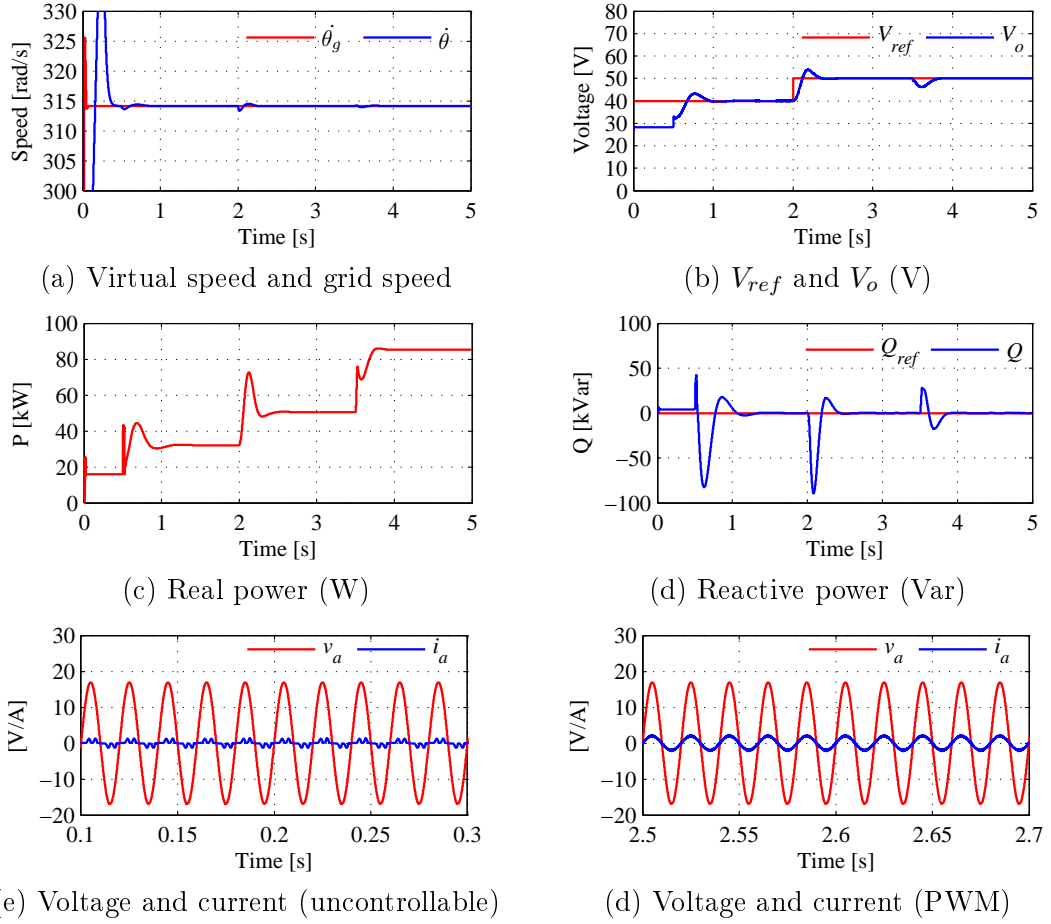


Figure 8.10: Simulation results when maintaining DC bus voltage.

The real power changed slightly but quickly recovered to the reference value. Meanwhile, the DC bus voltage changed gradually because of the capacitor on the DC bus. The reactive power was maintained at zero, apart from when there were changes in the reference or the load. The input voltage and current were in the same phase, which means the unity power factor is always achieved.

#### 8.4.2 Regulation of the output voltage

The reactive power reference  $Q_{ref}$  was set to zero for the unity power factor and the output voltage reference  $V_{ref}$  was set at 40V. The load  $R$  was  $50\Omega$  at the beginning. The output voltage reference was changed to  $V_{ref} = 50V$  at  $t = 2s$  and the load was changed to  $R = 30\Omega$  at  $t = 3.5s$ . In this simulation,  $K_p = 0.02$  and  $K_i = 0.2$  are

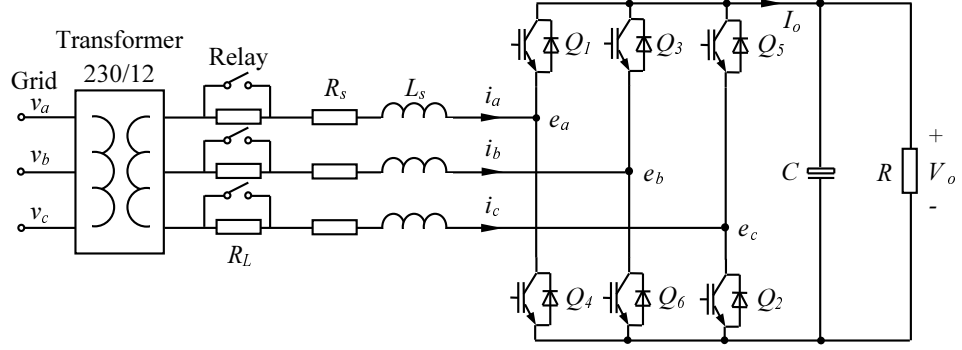


Figure 8.11: Experimental topology.

proportional and integral gains for a PI controller of the voltage loop, respectively.

The system responses are shown in the Figure 8.10. The virtual angular speed  $\dot{\theta}$  tracked the grid angular speed  $\dot{\theta}_g$  very well all the time. The results are similar to the previous case. There was a big overshoot on the real power when the DC bus voltage reference changed due to the effect of the DC bus capacitor. The output voltage tracked the reference voltage very well. When the load was changed, the voltage dropped but quickly returned to the reference value.

## 8.5 Experiment Results

Experiments were also carried out on a test rig, of which the parameters are roughly the same as those given in Table 9.1 and the control parameters are the same, to further demonstrate the analysis. The experimental setup consists of a rectifier board, a three-phase grid interface inductor, a board consisting of voltage and current transducers, a step-up transformer, a dSPACE DS1104 R&D controller board with ControlDesk software and the MATLAB Simulink/SimPower software package. The sampling frequency of the controller is 5kHz and the switching frequency is 10 kHz. For safety reasons, this test rig was a low-power low-voltage system but it was enough to demonstrate the proposed strategy and to compare the results with the simulation results. The parameters used in the experimental setup are the same as those used in the simulations given in Table 9.1. The experimental topology is shown in Figure 9.8 and the experimental setup is shown in Figure 8.12.

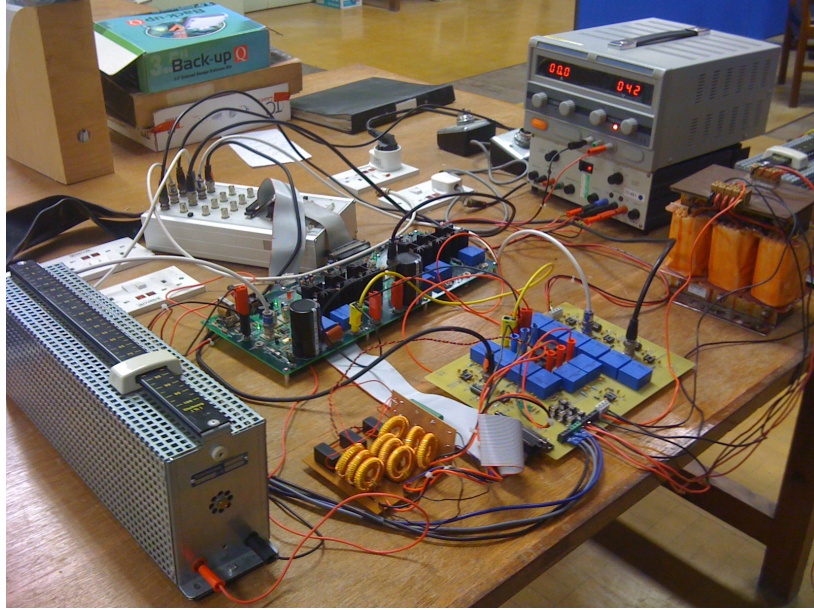


Figure 8.12: Experimental setup.

### 8.5.1 DPC

The experiment was carried out according to the following sequence of actions:

- 1) start the system, but keep all the IGBTs off; use the STA algorithm to synchronise the grid's frequency;
- 2) turn the relay on roughly at  $t=3s$ ;
- 3) connect to the load  $R=50\Omega$  roughly at  $t=5s$ ;
- 4) start operating the IGBTs roughly at  $t=10s$ ,  $P_{ref}=40W$  and Q loop was closed;
- 5) activate the Q loop roughly at  $t=20s$ ;
- 6) apply  $P_{ref}=60W$  roughly at  $t=30s$ ;
- 7) change the load to  $R=30\Omega$  roughly at  $t=41s$ .

Figure 8.13 shows the responses of the system.  $\dot{\theta}$  tracked  $\dot{\theta}_g$  very well all the time. From the beginning to 3s, most of the power is lost on  $R_L$  which makes the system safe for building up DC bus voltage slowly at the beginning. The DC bus voltage was built up at around 26V. The real power and reactive power were zero because there was no load on the DC bus. In order to remove  $R_L$ , relays were turned on at  $t=3s$ . The real power, increased slightly for charging the DC bus capacitor, then went back to zero, so that the the DC bus voltage went up to 28V. When the load  $R=50\Omega$  was connected to DC bus at  $t=5s$ , the real power increased to 16W. Theoretically, the DC bus voltage

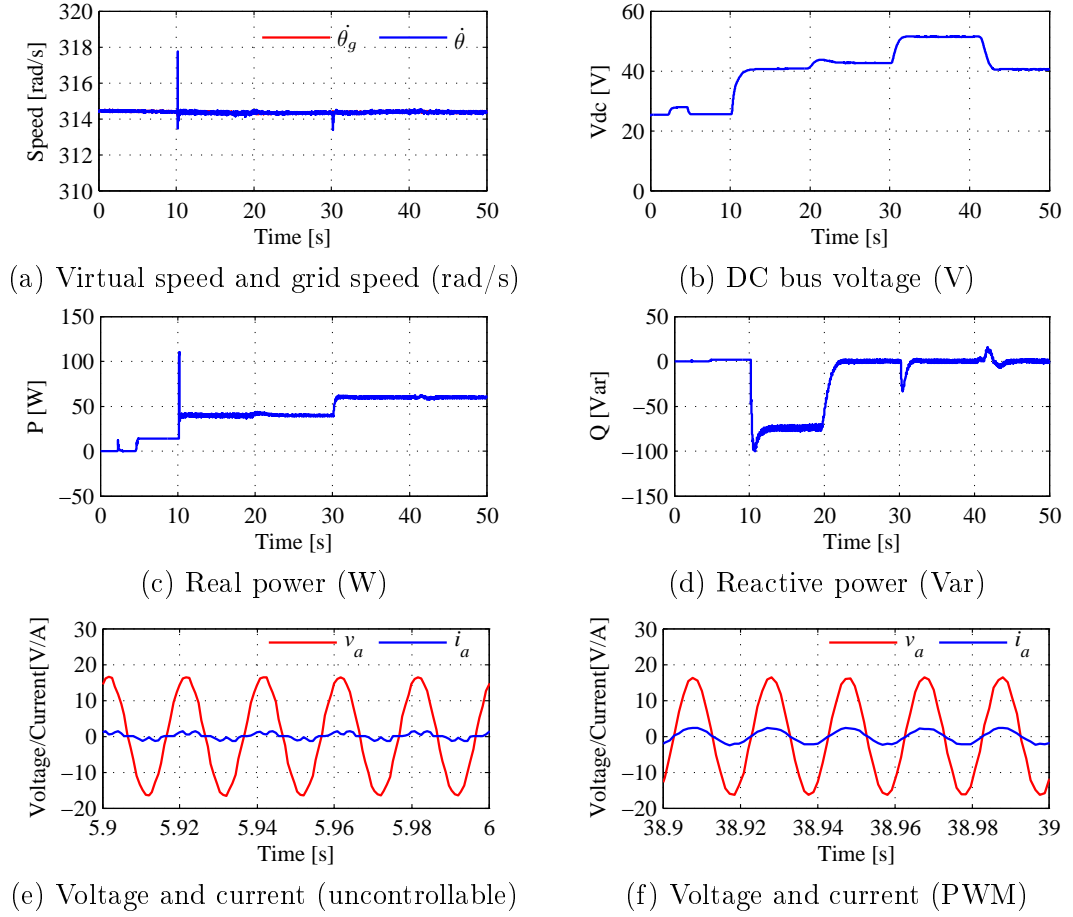


Figure 8.13: Experimental results of DPC.

should be  $2.34 \times 12 = 28$  V. The DC bus voltage dropped to 26V because the reactive power increased slightly. During this time, the system worked as an uncontrollable rectifier.

When the control strategy worked at  $t=10$ s, the real power went up to the reference value 40W immediately and the DC bus voltage increased to 41V gradually because of the big capacitor on the DC bus. Since the Q loop was closed, the reactive power decreased to 75 Var. After turning the Q loop on at  $t=20$ s, the reactive power needed to be zero to obtain the unity power factor. The DC bus voltage increased to 43V because of the reactive power compensation from 20s to 30s. After that, the real power increased to 60W quickly due to the reference changed. The DC bus voltage increased also, but the reactive power did not. When the load changed from  $50\Omega$  to  $30\Omega$  at  $t=41$ s, the real power and the reactive power were not changed, and the DC bus voltage dropped to



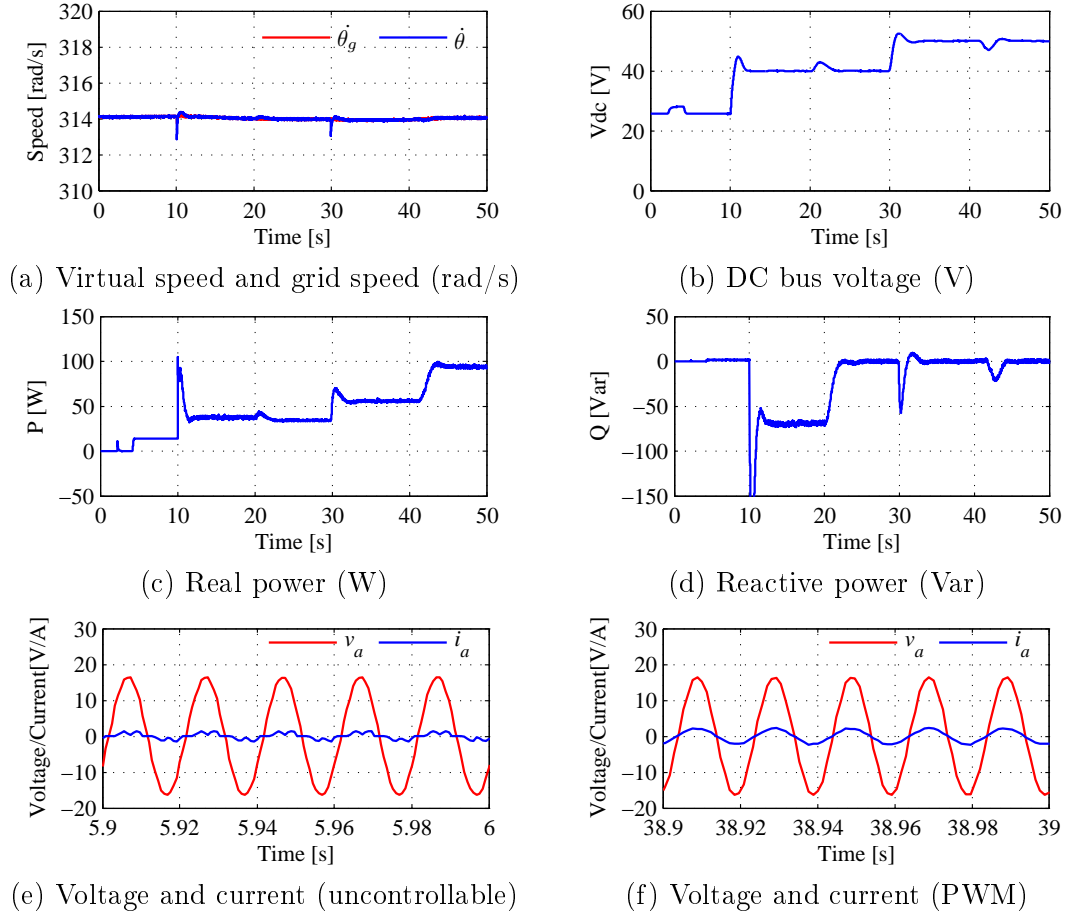


Figure 8.14: Experimental results with maintained the DC bus voltage.

40V. All the responses were the same as expected.

### 8.5.2 Regulation of the output voltage

The experiment was carried out according to the following sequence of actions:

- 1) start the system, but keep all the IGBTs off; use the STA algorithm to synchronise the grid's frequency;
- 2) turn the relay on roughly at  $t=2s$ , system works as an uncontrollable rectifier without load;
- 3) connect to the load  $R=50\Omega$  roughly at  $t=4s$ ;
- 4) start operating the IGBTs roughly at  $t=10s$ ,  $V_{ref}=40V$  and Q loop was closed;
- 5) activate the Q loop roughly at  $t=20s$ ;
- 6) apply  $V_{ref}=50V$  roughly at  $t=30s$ ;

7) change the load to  $R=30\Omega$  roughly at  $t=41s$ .

Figure 8.14 shows the responses of the system. From  $t=0$  to  $10s$ , the results are totally the same as the previous case. When the control strategy worked at  $t=10s$ , the DC bus voltage increased to the reference value  $40V$  and the real power increased to around  $40W$ . Since the Q loop was closed, the reactive power decreased to  $70Var$ . After turning the Q loop on at  $t=20s$ , the reactive power needed to be zero to obtain the unity power factor. The real power dropped slightly because of the reactive power compensation from  $20s$  to  $30s$ . The DC bus voltage kept the reference value very well. After this, the DC bus voltage increased to  $50V$  quickly due to the reference change. The real power increased as well but the reactive power did not. When the load changed from  $50\Omega$  to  $30\Omega$  at  $t=41s$ , the DC bus voltage and the reactive power did not change, and the real power went up to  $95W$ .

## 8.6 Conclusions

In this chapter, the three-phase PWM rectifiers are operated to mimic a synchronous motor with two different control strategies, which can possess most of the characteristics of conventional synchronous motors. Therefore, when PWM rectifiers are connected with the utility grid, the previous operation methods of the utility grid can still be used regardless of the particular load characteristics; the stability of the utility grid can be improved accordingly. In the proposed schemes, the real power extracted from the source and the output voltage are the control objectives, respectively, hence they can be employed in different applications. Moreover, the reactive power can easily be controlled to remain at zero in the steady state so that the unity power factor is obtained. Both simulation and experimental results are provided to demonstrate the proposed control strategies.

## Chapter 9

# Synchronverters Operated as Rectifiers without a PLL

PWM-controlled rectifiers are increasingly used in industrial applications, such as ASD for induction machines and UPS, with bidirectional AC-DC-AC power converters. When compared with conventional diode rectifiers, PWM-controlled rectifiers have many advantages such as output voltage control, direct power control, sinusoidal line current with low THD, power factor correction, and bi-directional power flow [94, 95].

Various control strategies have been proposed in recent years for PWM-controlled rectifiers. The classical solution is the VOC scheme, which uses closed-loop current control in the rotating reference frame. It offers good dynamic and static performance and has constantly been developed and improved [96, 97, 98, 99]. The configuration and performance of a VOC system largely depend on the quality of the applied current control strategy, which normally consists of an inner high bandwidth current control loop and an outer low bandwidth DC voltage regulation loop [100]. The current controller regulates the line current to track the reference to ensure unity power factor operation and power balance on the output of the rectifier. The DC bus voltage regulator indirectly regulates the power fed into the rectifier to achieve constant DC bus voltage control [101, 102, 103].

Another solution is based on the idea of DPC. It adopts instantaneous real and reactive power control loops to control the power directly using hysteresis control, without using inner current loops. No pulse-width-modulation (PWM) block is needed because the states of the converter switches are selected from a table based on the instantaneous errors between the set-point and the measured values of real and reactive power

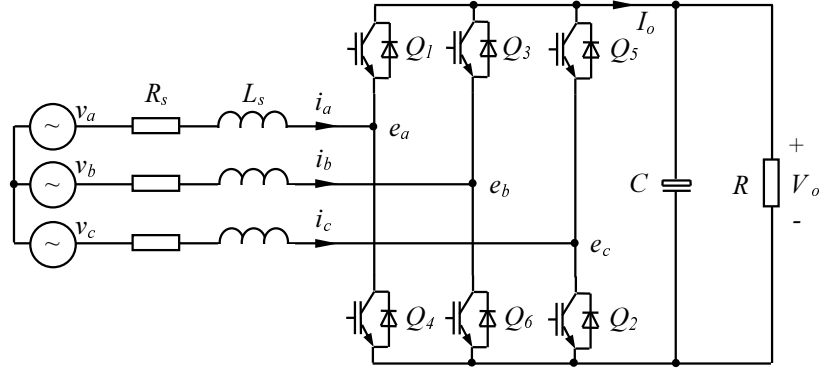


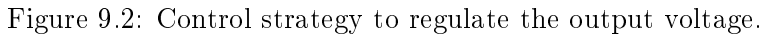
Figure 9.1: A three-phase PWM-controlled rectifier.

[104, 105, 106, 107, 108, 109]. This leads to a variable switching frequency. It is difficult to implement in industry because of the variable switching frequency and the high sampling frequency needed for digital implementation.

Recently, the synchronverter technology [40, 1] has been proposed as an inverter to mimic synchronous generators and, hence, it considerably facilitates the grid connection of renewable energy and smart grid integration. Since synchronous generators have been studied for more than 100 years, and the relevant technologies have reached a high level of maturity, all these technologies can easily be applied to control inverters. Moreover, the synchronverter technology has been extended to operate a rectifier to mimic SM [111]. This strategy can control the output voltage and the power directly with excellent performance.

It has become a convention for control strategies of a grid-connected converter (inverter or rectifier), regardless of the methods applied, to embed a synchronisation unit, e.g. a PLL [112, 113], to provide the information about the grid frequency and phase so that the converter is able to synchronise with the grid voltage. As a result, a large number of research activities have been developed for PLL [114, 115, 116, 117, 118, 119, 120]. It is known that PLLs have a negative impact on control performance [121, 122] and it is beneficial if it can be removed. A slow PLL could directly affect the control performance and degrade system stability but a complex PLL, on the other hand, is often computationally intensive, which adds significant burden to the controller.

In this chapter, a control strategy is presented to control the output voltage for three-phase PWM-controlled rectifiers. The controller is able to track the grid frequency and phase automatically so that an extra synchronisation unit is no longer needed. This



## 9.1 Proposed Control Strategies

The proposed controller to regulate the output voltage of a PWM-controlled rectifier is shown in Figure 9.2. Comparing this to Figure 8.8, it is easy to see that there are three major changes. Firstly, a virtual current  $i_s$  generated from the error between the grid voltage  $v$  and the control signal  $e$  is introduced, and the current fed into the controller can be either the virtual current  $i_s$  or the grid current  $i$ . Secondly, the synchronisation unit, which provides the grid frequency reference and the reset signal, is removed from the controller. Finally, a PI controller is added to generate the reference speed  $\dot{\theta}_r$  for the virtual synchronous motor, while driving the error between the reference speed  $\dot{\theta}_r$  and the virtual speed  $\dot{\theta}$  to zero. It will be shown later that the reference speed  $\dot{\theta}_r$  converges to the grid frequency at the steady state.

97

PWM-controlled mode to explain how the controller works and why the changes should be made.

#### 9.1.1.1 Uncontrolled mode

When turning on the switches, the control signals  $e$  must be synchronised with the grid voltage  $v$ , with the same phase sequence. Otherwise, high inrush currents may flow through the line impedance from the grid to the rectifier because of the error between the control signals  $e$  and the grid voltage  $v$ , which might destroy the relevant components in the circuit. Moreover, it would be ideal if the amplitude  $E$  is also the same as the amplitude of  $v$ .

During the uncontrolled mode, the  $Q$ -loop of the controller and the DC bus voltage loop should be disabled. The virtual mechanical torque  $T_m$  can be set to be zero and the virtual field excitation  $M_f i_f$  can be set as  $\frac{E}{\dot{\theta}_n}$ , where  $\dot{\theta}_n$  is the nominal grid frequency (here  $\dot{\theta}_n = 100\pi$ ). However, the current  $i$  flowing through the line impedance from the grid to the rectifier is not available for the controller because the current  $i$  cannot be controlled by the controller when the rectifier is operated in the uncontrolled mode. In order to solve this problem, a virtual current

$$i_s = \frac{1}{sL_s + R_s}(v - e), \quad (9.1)$$

which is generated from the error between  $v$  and  $e$ , is introduced to replace  $i$  for feedback so that  $T_e$  can be calculated according to Equation (8.4). Since the current  $i_s$  is not physical, the virtual synchronous inductor  $sL_s + R_s$  can be small to speed up the synchronisation process.

When the control signal  $e$  is equal to the grid voltage  $v$ , the virtual current  $i_s$  is zero according to Equation (9.1), so that the controller is synchronised with the grid. After synchronisation, the switches can be turned on at any time to operate the rectifier in the PWM-controlled mode. At the same time, the Switch  $S$  should be turned to Position 2 so that the real current  $i$  is fed into the controller for the normal operation. Note that although the control signal  $e$  is the same as the grid voltage  $v$ , the recovered voltage at the terminals of the PWM-controlled rectifier is in phase with  $v$  but with a smaller amplitude because the DC bus voltage is not high enough. Hence, the inrush current when turning the switches on can only be reduced, but not completely eliminated.

### 9.1.1.2 PWM-controlled mode

When the rectifier is operated in the PWM-controlled mode, not only should the Switch  $S$  be turned to Position 2, but also the  $Q$ -loop and the DC bus voltage loop should be enabled at the same time. Since the regulation of the output voltage and the reactive power are outlined in the last section, only the characteristics that are different from the control strategy are described here.

It is well known that the phase difference

$$\delta = \theta_g - \theta \quad (9.2)$$

where  $\theta_g$  is the phase of the grid voltage. The phase difference is often called the power angle and is controlled by the virtual mechanical torque  $T_m$ . If the grid phase  $\theta_g$  (or speed  $\dot{\theta}_g$ ) decreases, then the power angle  $\delta$  decreases according to Equation (9.2). As a result, the real power fed into the rectifier decreases and the output voltage of the rectifier also decreases when the load is not changed. This causes the virtual mechanical torque  $T_m$  to increase because of the regulation of the DC bus voltage PI controller ( $K_{pv} + \frac{K_{iv}}{s}$ ). As a result, the input to the integrator block  $\frac{1}{s}$  in Figure 9.2 decreases, because of the negative sign before the summation block, and the speed  $\dot{\theta}$  of the virtual SM decreases. At the same time,  $\Delta\dot{\theta}$  increases so that  $\Delta\dot{\theta}_g$  also increases because of the regulation of the frequency PI controller ( $K_{pf} + \frac{K_{if}}{s}$ ), which causes the speed reference  $\dot{\theta}_r$  to decrease according to  $\dot{\theta}_r = \dot{\theta}_n - \Delta\dot{\theta}_g$ . The regulation process continues till  $\dot{\theta} = \dot{\theta}_r$  and  $\dot{\theta}_r = \dot{\theta}_g$ .

If the grid frequency  $\dot{\theta}_g$  increases, then a similar process happens till  $\dot{\theta} = \dot{\theta}_r = \dot{\theta}_g$ . Therefore, the frequency  $\dot{\theta}$  is able to track the grid frequency  $\dot{\theta}_g$  automatically so that the controller does not need an extra synchronisation unit to provide the grid frequency  $\dot{\theta}_g$  as the reference frequency.

### 9.1.2 Regulation of the power

Direct Power Control (DPC) adopts instantaneous real and reactive power control loops to control the power directly. The control strategy to achieve this is shown in Figure 9.3. The outer-loop controller regulating the output voltage in Figure 9.2 is replaced with one to regulate the real power. The error between the real power reference  $P_{ref}$  and the real power  $P$  is fed into the real power PI controller ( $K_{pp} + \frac{K_{ip}}{s}$ ) to generate

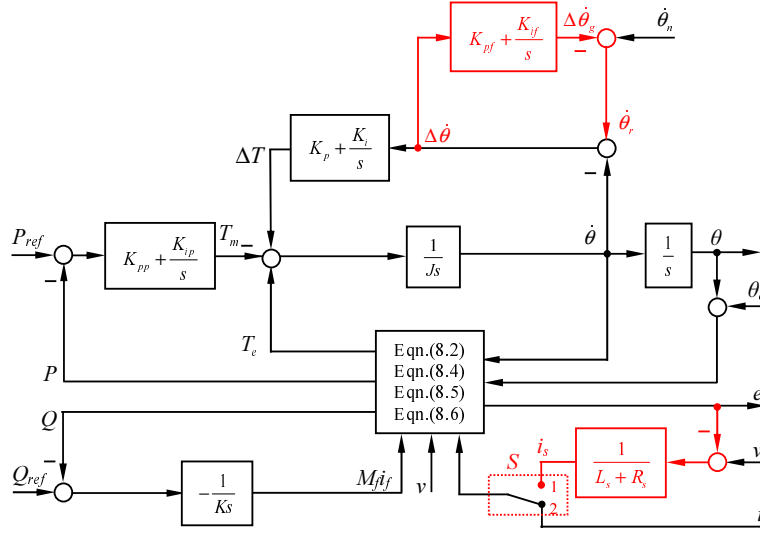


Figure 9.3: Control strategy to regulate the power.

Table 9.1: Parameters of the system for simulations

Parameters	Values	Parameters	Values
$L_s$	0.45 mH	$R_s$	0.135 $\Omega$
$C$	5000 $\mu$ F	Switching Frequency	10 KHz
Input voltage	12 Vrms	Line frequency	50 Hz

the virtual torque  $T_m$ . The rest of the controller is the same as in the previous case for regulating the output voltage.

## 9.2 Simulation Results

In order to verify the proposed control strategy described above, a three-phase PWM-controlled rectifier with the whole control scheme was simulated in Matlab7.6/ Simulink/ SimpowerSystems. The solver used in the simulations was ode23t with a relative tolerance of  $10^{-3}$  and the sampling time was 10  $\mu$ s. The parameters of the rectifier used in the simulation are given in Table 9.1.

In the simulation, the rectifier was connected to the grid via a step-down transformer. However, the proposed control strategy could work for high voltage and high power applications as well.



Table 9.2: Parameters of the controller.

Parameters	Values	Parameters	Values
$K_{pf}$	0.5	$K_{if}$	7
$K_{pv}$	0.01	$K_{iv}$	0.1
$J$	0.0002 kgm <sup>2</sup>	$K$	370

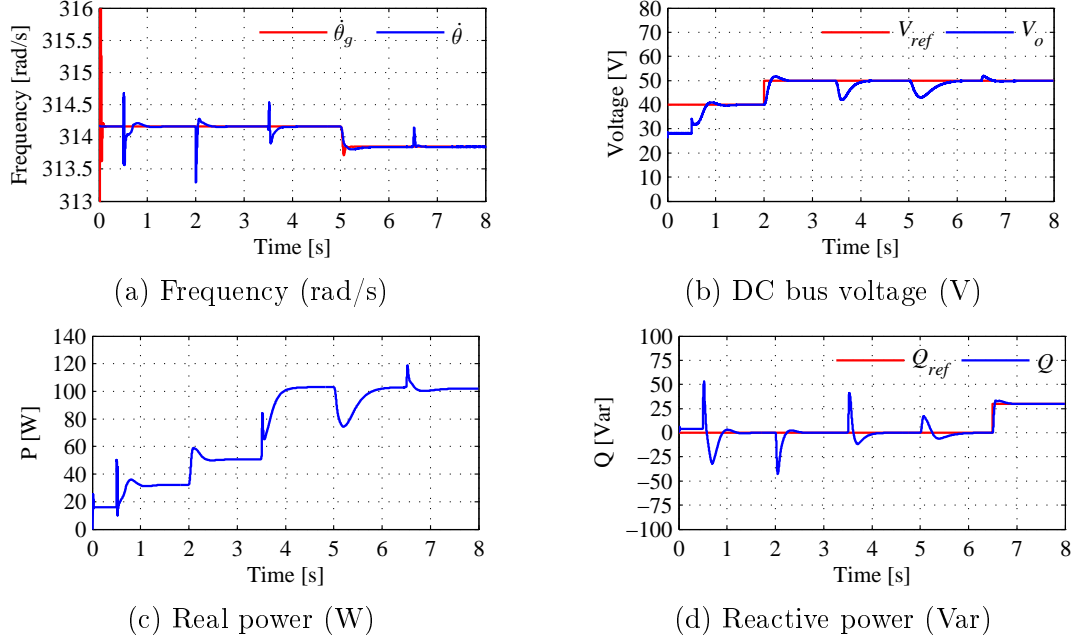
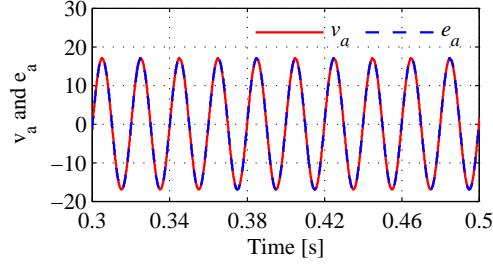


Figure 9.4: Simulation results when regulating the output voltage.

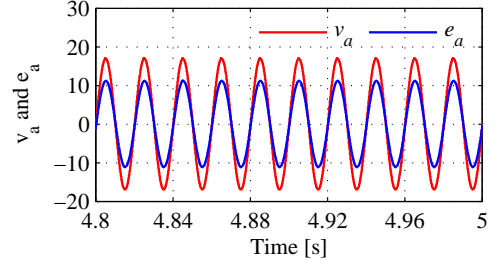
### 9.2.1 Regulation of the output voltage

The parameters of the controller used in the simulation are shown in Table 9.2.

The simulation was started at  $t = 0$  s, with Switch  $S$  at Position 1. The rectifier worked in the uncontrolled mode for the first 0.5 s, during which the DC bus voltage loop and the  $Q$ -loop were disabled in order for the rectifier to synchronise with the grid voltage. At  $t = 0.5$  s, the DC bus voltage loop and the  $Q$ -loop were enabled, the Switch  $S$  was switched to Position 2 and the PWM signals were released to the rectifier. Initially, the output voltage reference  $V_{ref}$  was 40 V and the reactive power reference  $Q_{ref}$  was set to zero to obtain the unity power factor for a load  $R$  of 50  $\Omega$ . The output voltage reference was increased to  $V_{ref} = 50$  V at  $t = 2$  s and the load was changed to  $R = 25$   $\Omega$  at  $t = 3.5$  s. At  $t = 5$  s, the grid voltage frequency decreased from 50 Hz to 49.95 Hz and at  $t = 6.5$  s the reactive power reference was changed to  $Q_{ref} = 30$  Var .

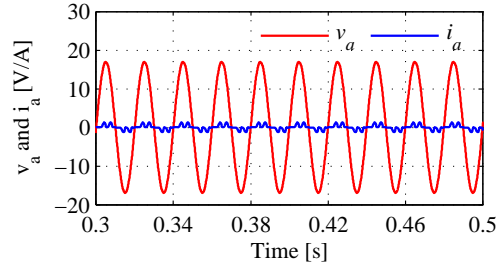


(a) In the uncontrolled mode

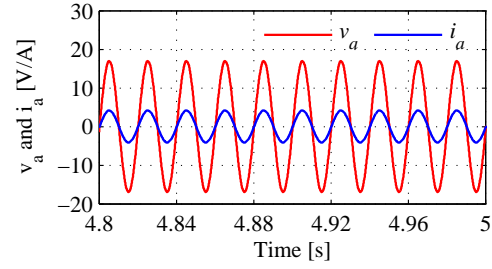


(b) In the PWM-controlled mode

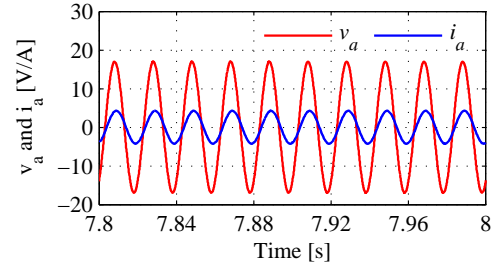
Figure 9.5: Grid voltage and control signal.



(a) In the uncontrolled mode



(b) In the PWM-controlled mode with  $Q_{ref} = 0$  Var



(c) In the PWM-controlled mode with  $Q_{ref} = 30$  Var

Figure 9.6: Input voltage and current.

Table 9.3: Control parameters for regulating the power.

Parameters	Values	Parameters	Values
$K_{pf}$	0.5	$K_{if}$	7
$K_{pp}$	0.001	$K_{ip}$	0.1
$J$	0.0002 kgm <sup>2</sup>	$K$	370

The simulation results are shown in Figure 9.4. The rectifier tracked the grid frequency very well. Moreover, the output voltage and the reactive power tracked their references quickly and accurately under different operational conditions. Here, the grid frequency  $\dot{\theta}_g$ , obtained from a PLL, is also shown in Figure 9.4(a) to illustrate that the proposed strategy worked properly without the need for an extra synchronisation unit.

As shown in Figure 9.5(a), when the rectifier worked in the uncontrolled mode, the control signal  $e$  was synchronised with the grid voltage  $v$  (in terms of phase and frequency). When it was operated in the PWM-controlled mode, as shown in Figure 9.5(b), the control signal  $e_a$  was lower than the grid voltage  $v_a$  so that the current could flow from the grid to the rectifier to supply the DC load.

PWM-controlled rectifiers are able to improve the THD of the input currents and to compensate for the reactive power drawn from the grid. This is demonstrated with the simulation results shown in Figure 9.6. When the rectifier was operated in the uncontrolled mode, the input current as shown in Figure 9.6 was distorted with high THD. When the rectifier was operated under the PWM-controlled mode with  $Q = 0$ , the input current was nearly sinusoidal with THD=0.5% and in phase with the line voltage, as shown in Figure 9.6(b). Therefore, the unity power factor operation of the rectifier was successfully achieved by maintaining the reactive power at zero. The rectifier was also able to provide reactive power, as shown in Figure 9.6(c), where the input current was also nearly sinusoidal but with a phase shift, because the reference for the reactive power was set at  $Q_{ref} = 30$  Var.

### 9.2.2 Regulation of the power

The parameters of the controller used in the simulation are given in Table 9.3.

The simulation was started at  $t = 0$ , with Switch  $S$  at Position 1. The rectifier worked in the uncontrollable mode for the first 0.5 s. During this time, the  $P$ -loop and  $Q$ -loop were disabled in order that the controller could be synchronised with the grid voltage and let  $e = v$  for the initial synchronisation. The rectifier operated in the PWM

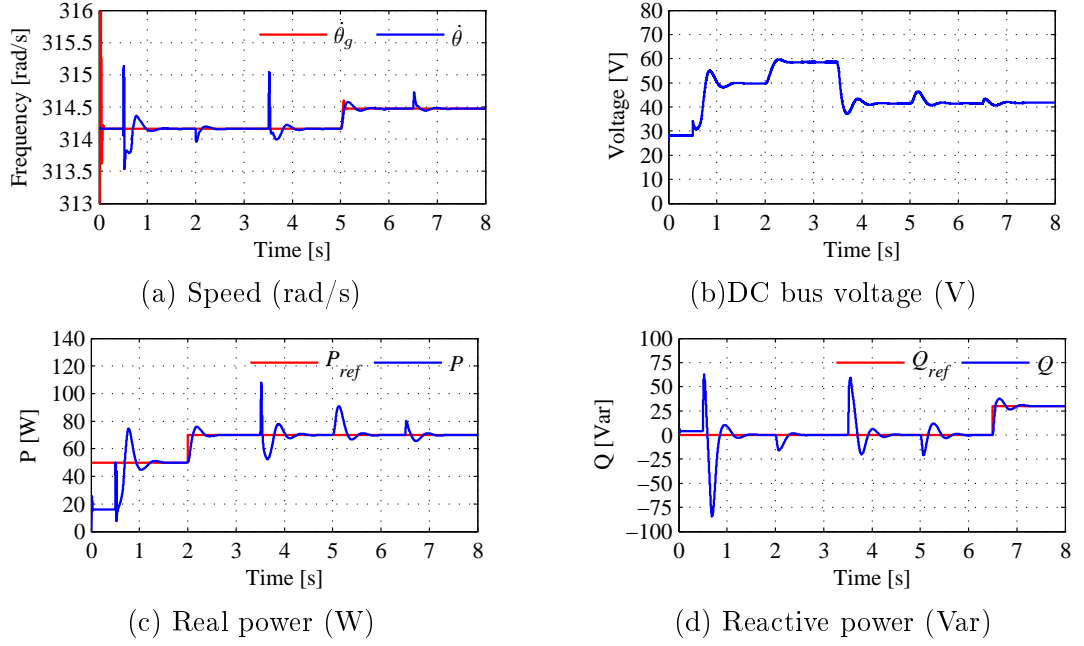


Figure 9.7: Simulation results when regulating the power.

mode at  $t = 0.5$  s, meanwhile, the  $P$ -loop and  $Q$ -loop were enabled and the Switch  $S$  was switched to Position 2. Initially, the real power reference  $P_{ref}$  was 50 W and the reactive power reference  $Q_{ref}$  was set to zero to obtain the unity power factor and load  $R$  was  $50 \Omega$ . The real power reference was increased to  $P_{ref} = 70$  W at  $t = 2$  s and the load was changed to  $R = 25\Omega$  at  $t = 3.5$  s. At  $t = 5$  s, the grid voltage frequency increased from 50 Hz to 50.05 Hz. Eventually, the reactive power reference was set to  $Q_{ref}=30$  Var at  $t = 6.5$  s. The system dynamic responses are shown in Figure 9.7.

### 9.3 Experimental Results

Experiments were also carried out on a test rig, which was described in the previous chapter, to further demonstrate the control strategy. The parameters are roughly the same as those given in Table 9.1, with the same control parameters given in Table 9.2 and Table 9.3. The experimental topology is shown in Figure 9.8.

#### 9.3.1 Regulation of the output voltage

The experiment was carried out according to the following sequence of actions:

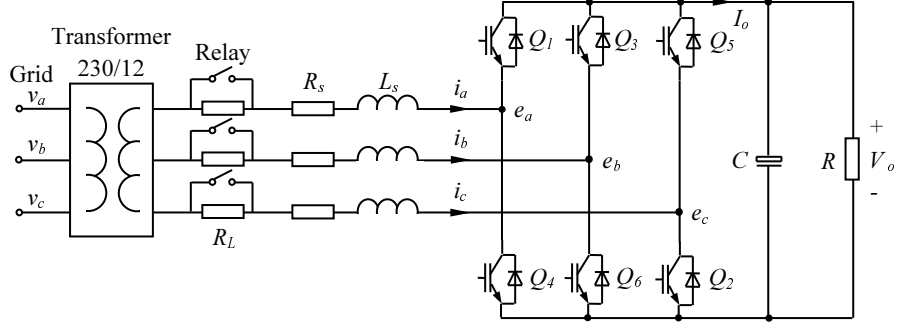


Figure 9.8: Experimental topology.

- 1) start the system but keep all IGBTs off; disable the DC bus voltage loop and the  $Q$ -loop, Switch  $S$  to Position 1;
- 2) turn the relay on roughly at  $t = 3$  s to short-circuit the rheostat that was added at the place of  $R_s$  to connect the rectifier to the power supply so that the system works in the uncontrolled mode without a load;
- 3) connect the load  $R = 50 \Omega$  roughly at  $t = 5$  s;
- 4) operate the IGBTs roughly at  $t = 10$  s, Switch  $S$  to Position 2, enable the DC bus voltage loop with  $V_{ref} = 40$  V;
- 5) enable the  $Q$ -loop and set  $Q_{ref} = 0$  roughly at  $t = 20$  s;
- 6) apply  $V_{ref} = 50$  V roughly at  $t = 31$  s;
- 7) change the load to  $R = 30 \Omega$  roughly at  $t = 42$  s.

Figure 9.9 shows the responses of the system, where the grid frequency  $\dot{\theta}_g$  obtained from a PLL is also shown in Figure 9.9(a) for comparison.  $\dot{\theta}$  tracked  $\dot{\theta}_g$  very well throughout. At the beginning, the real power and reactive power were zero because there was no load on the DC bus. After the relays were turned on at  $t = 3$  s, the real power increased slightly to charge the DC bus capacitor then went back to zero quickly and the DC bus voltage went up to 28 V. When the load  $R = 50 \Omega$  was connected to the DC bus at  $t = 5$  s, the real power increased to 16 W and the rectifier worked in the uncontrolled mode.

When the proposed control strategy started working at  $t = 10$  s, the DC bus voltage increased to the reference value 40 V. Since the  $Q$ -loop was not enabled, the reactive power decreased to about -70 Var. After turning the  $Q$ -loop on at  $t = 20$  s, the reactive power was driven to zero to obtain the unity power factor, while the DC bus voltage was maintained well at 40 V. When the DC bus voltage reference was increased to 50 V

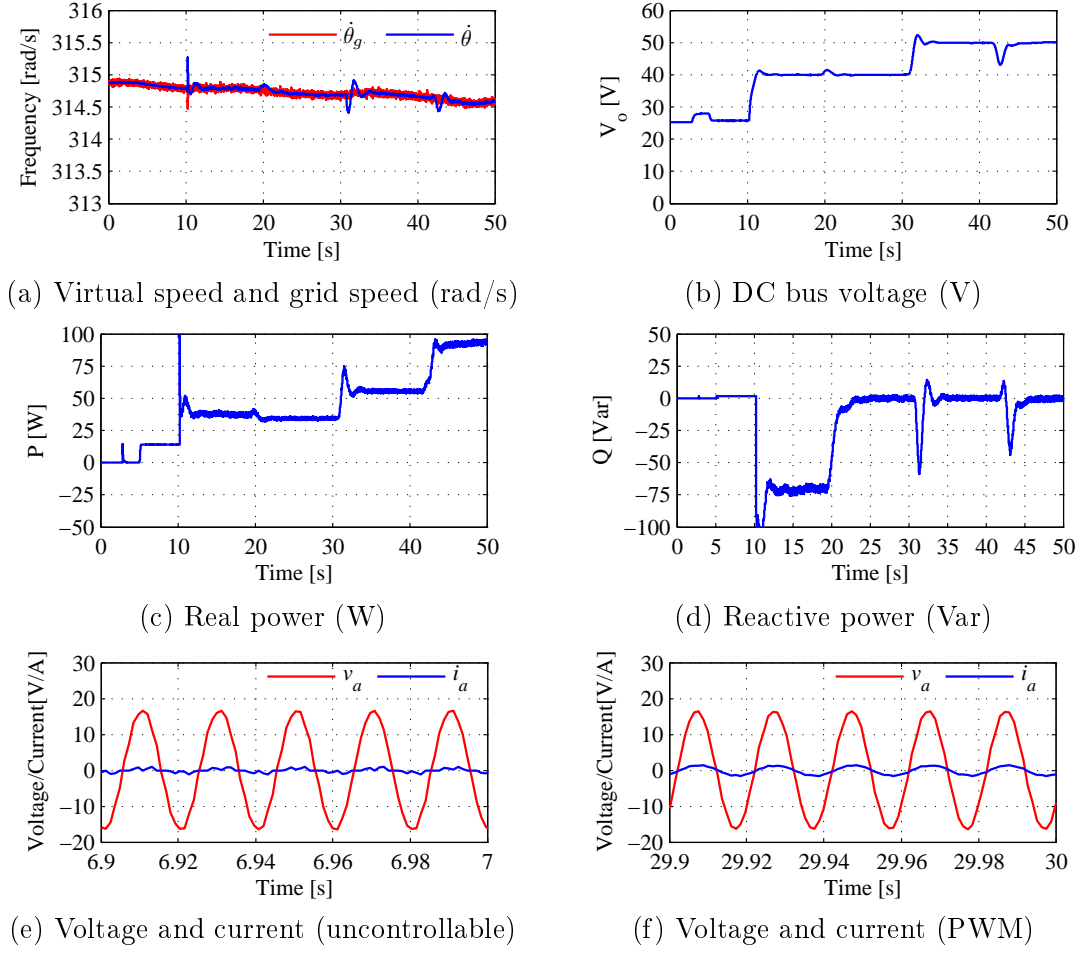


Figure 9.9: Experimental results when regulating the output voltage.

at  $t = 31$  s, the DC bus voltage quickly increased to the reference value. The reactive power deviated but quickly returned to zero to maintain the unity power factor. When the load was changed from  $50 \Omega$  to  $30 \Omega$  at  $t = 42$  s, the DC bus voltage was maintained well. Again the reactive power deviated but returned to zero quickly. It is worth noting that the grid frequency was changing during the experiment but it did not affect the performance of the system.

### 9.3.2 Regulation of the power

The experiment was carried out according to the following sequence of actions:

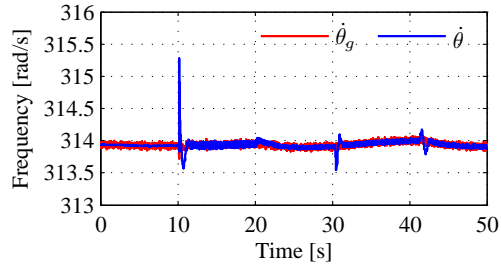
- 1) start the system, but keep all the IGBTs off; disable  $P$ -loop and  $Q$ -loop, Switch  $S$  to Position 1;

- 2) turn the relay on roughly at  $t = 2$  s;
- 3) connect to the load  $R = 50\ \Omega$  roughly at  $t = 7$  s;
- 4) start operating the IGBTs roughly at  $t = 10$  s, Switch  $S$  to Position 2, enable  $Q$ -loop and set  $P_{ref} = 40$  W;
- 5) enable the  $Q$ -loop roughly at  $t = 20$  s;
- 6) apply  $P_{ref} = 60$  W roughly at  $t = 30$  s;
- 7) change the load to  $R = 30\ \Omega$  roughly at  $t = 41$  s.

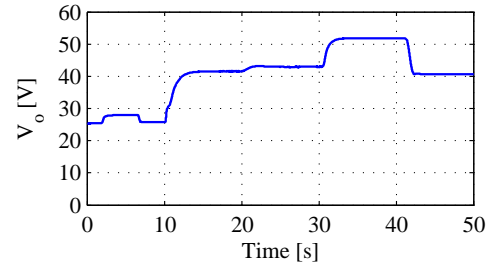
Figure 9.10 shows the responses of the system. From  $t = 0$  to 10 s, the results are totally the same as the previous case. When the control strategy worked at  $t = 10$  s, the real power went up to the reference value of 40 W immediately and the DC bus voltage increased to 42 V gradually because of the big capacitor on the DC bus. Since the  $Q$  loop was closed, the reactive power decreased to 70 Var. After turning the  $Q$  loop on at  $t = 20$  s, the reactive power remained at zero to obtain the unity power factor. The DC bus voltage increased to 43 V because of the reactive power compensation from 20s to 30s. After that, the real power increased to 60W quickly due to the reference change. The DC bus voltage also increased but the reactive power did not. When the load changed from 50  $\Omega$  to 30  $\Omega$  at  $t = 41$  s, the real power and the reactive power were not changed, and the DC bus voltage dropped to 41 V. All the responses are the same as expected.

## 9.4 Conclusions

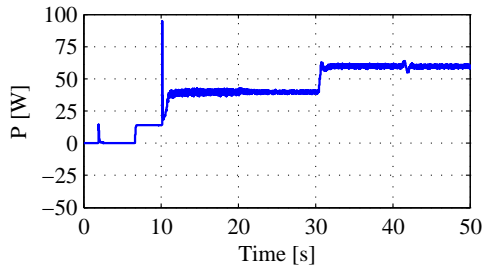
Control strategies without the need of a synchronisation unit have been proposed for three-phase PWM-controlled rectifiers, based on the recently proposed synchronverter technology. The proposed control strategies are able to regulate the DC bus voltage and the reactive power drawn from the supply. Hence, it is able to obtain clean sinusoidal line currents and a unity power factor with ease. Both simulation and experimental results are provided to demonstrate the excellent performance of the proposed control strategy.



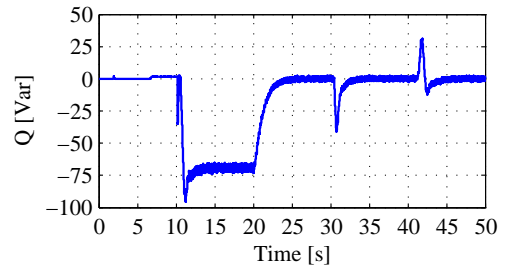
(a) Virtual speed and grid speed (rad/s)



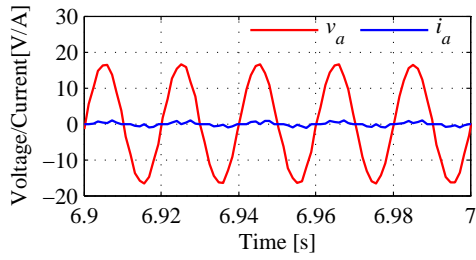
(b) DC bus voltage (V)



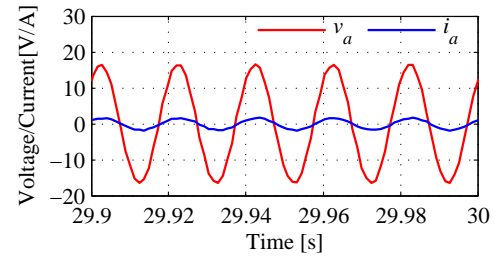
(c) Real power (W)



(d) Reactive power (Var)



(e) Voltage and current (uncontrollable)



(e) Voltage and current (PWM)

Figure 9.10: Experimental results when regulating the power.



## Chapter 10

# Synchronverter-based Back-to-back Converter for Wind Power

During the last decade, more and more attention has been paid to utilising renewable energy sources to tackle the energy crisis we are facing. Wind power has been regarded as one of the main alternative renewable power sources to replace/complement fossil fuels. Wind energy has many advantages such as no pollution, the relatively low capital cost involved and the short gestation period. Many countries have set strategic plans to develop technologies for utilising wind power and a lot of researchers have shifted into this area.

Wind generation systems can be divided into variable-speed generation systems and fixed-speed generation systems. Variable-speed systems are more attractive than fixed-speed systems due to the improved wind energy production and the reduction of flicker problems. Nowadays, the most-used topologies for variable-speed wind turbines are doubly-fed induction generators with wound rotors, induction generators with squirrel cage rotors and synchronous generators with permanent magnets [7]. In these three cases, one of the most popular grid connection topologies is to adopt back-to-back voltage source inverters to interface with the grid [10] to provide unity power factor and low harmonic distortion of current, as shown in Figure 10.1. The synchronous generator is connected to the grid through a full-scale back-to-back PWM converter and the conversion stage consists of a rotor-side converter and a grid-side converter. It has a substantial influence for power quality, because non-sinusoidal currents delivered to the grid can introduce an additional non-sinusoidal voltage drop across the line

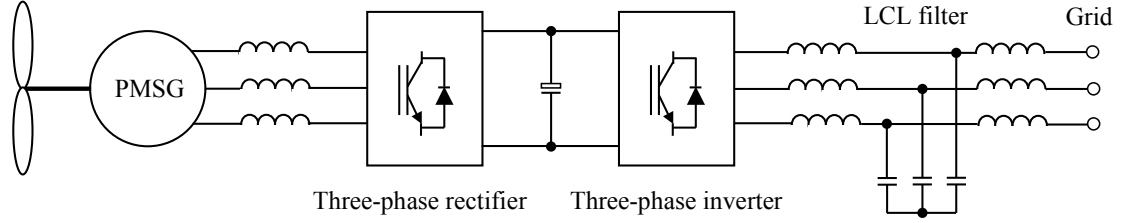


Figure 10.1: Connection of wind power generation system to the grid through back-to-back converters.

impedance. This increases the grid voltage distortion, which affects many other loads and/or other generators.

Many different control strategies have been developed for back-to-back PWM converters in wind power applications. Normally, the maximum power point tracking is achieved by controlling the rotor-side converter and the DC bus voltage is controlled by the grid-side converter [123, 124, 125, 126, 127, 128, 129]. In this case, the DC bus voltage is increased due to the continuous operation of the wind turbine and generator when grid faults happen. The grid-side converter may be out of control when the grid voltage sags happen because voltage sags reduce generator torque [130], which accelerates the rotor and causes mechanical instability unless normal voltage levels are quickly restored. As a fail-safe mechanism against equipment damage, wind turbines are designed to automatically disconnect themselves from the utility grid under these extreme conditions [131, 132]. Therefore, in some other strategies, the rotor-side converter controls the DC bus voltage and the grid-side converter controls the power of the wind turbine fed to the grid [133, 134, 135]. In both cases, the control strategies are mainly based on the vector control approach in the d-q reference frame to control the direct component and quadrature component, respectively. In this chapter, an original control strategy based on the synchronverter technology, which is to operate a converter to mimic a synchronous machine [1], is proposed for back-to-back converters in wind power applications. The rotor-side converter is run as a synchronous motor and the grid-side converter is run as a synchronous generator. As a result, the whole system behaves as a generator–motor–generator system.

## 10.1 Control of the Rotor-side Converter

As mentioned before, the rotor-side converter is used to maintain a constant DC bus voltage. Hence, it is run as a PWM rectifier. Here, this is done via operating the PWM rectifier to mimic a synchronous motor.

The output voltage and current of the wind-turbine generator are denoted as  $v_r = [v_{ra} \ v_{rb} \ v_{rc}]^T$  and  $i_r = [i_{ra} \ i_{rb} \ i_{rc}]^T$ , respectively. The proposed control strategy is shown in Figure 10.2, which includes the model of a synchronous motor as the core of the control strategy. The model of a synchronous motor is more or less the same as the model of a generator discussed above, apart from the fact that the direction of the stator current is defined as opposite. Therefore, Equations (5.1) and (5.3) should be modified accordingly as

$$v_r = e_m + R_s i_r + L_s \frac{di_r}{dt},$$

and

$$\ddot{\theta}_m = \frac{1}{J_m}(T_{me} - T_{mm} - D_{mp}\dot{\theta}_m),$$

where the mechanical torque  $T_{mm}$  is the load to the motor. Here, this is generated by the PI controller that regulates the DC bus voltage.

The strategy has two channels: one to regulate the real power and the other to regulate the reactive power. The real power channel shown in Figure 10.2 has three cascaded control loops. The inner loop is the frequency regulation loop (with the feedback gain  $D_{mp}$ ); the middle loop is a torque loop (with the feedback coming from the current  $i_r$  via the electromagnetic torque  $T_{me}$ ) and the outer loop is the DC bus voltage loop (with the feedback coming from the DC bus voltage  $V_{dc}$ ). The first two loops are part of the model of a virtual synchronous motor.

When the rotor-side converter is connected to  $v_r$ , its virtual frequency should track the frequency of  $v_r$ . This can be done via feeding the difference between the frequency  $\dot{\theta}_r$  obtained from the STA and the rectifier frequency  $\dot{\theta}_m$  to the  $D_{mp}$  block, as done in the synchronverter [1]. In this case, the constant  $D_{mp}$  represents the (imaginary) mechanical friction coefficient of the virtual motor. It is effectively the frequency droop coefficient defined as  $D_{mp} = -\frac{\Delta T}{\Delta \dot{\theta}_m}$ , which corresponds to a certain amount of change  $\Delta T$  in the torque leading to a change  $\Delta \dot{\theta}_m$  in the frequency.

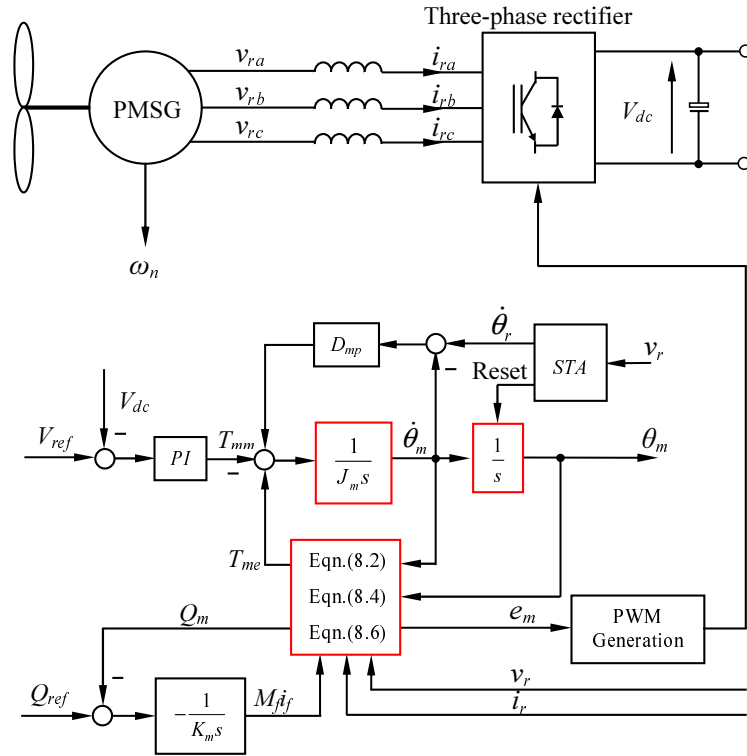


Figure 10.2: Control structure for the rotor-side converter.

The reactive power  $Q_m$  of the rotor-side converter can be controlled to track the reference  $Q_{ref}$ . The tracking error between the reference value  $Q_{ref}$  and the reactive power  $Q_m$  is fed into an integrator with a gain  $-\frac{1}{K}$  to regulate the field excitation  $M_{fif}$  so that the voltage  $e_m$  is changed. In order to obtain the unity power factor,  $Q_{ref}$  can be set as 0.

In order for the rotor-side converter, i.e., the virtual synchronous motor, to work properly, the frequency  $\dot{\theta}_m$  inside the rectifier should be the same as, or very close to, the frequency  $\dot{\theta}_r$  of  $v_r$  and the terminal voltage should be synchronised with the voltage  $v_r$ . Before the rectifier is connected to  $v_r$ , its phase  $\theta_m$  should be kept the same as that of  $v_r$  in order to minimise the settling time following the connection. The traditional phase-locked loop (PLL) in the dq frame is not fast enough for this purpose [136]. In this control strategy, the sinusoid-tracking algorithm (STA) [110] is adopted to provide the frequency signal and the phase information quickly.



The control objective for the grid-side converter is to send the maximum power generated from the wind to the grid. Normally, variable-speed wind generation systems are more attractive than fixed-speed systems due to high efficiency. However, it does not mean that the actual efficiency is always high in variable-speed generator systems. It depends on the control algorithm used to extract the output power from the wind turbine. An advanced technique will be designed to extract maximum power from the wind turbine under all working conditions. In variable-speed generation systems, the wind turbine can be operated at its maximum power operating point for various wind speeds by maintaining the tip speed ratio at the value that maximises its aerodynamic efficiency. In order to achieve this ratio, the permanent magnet synchronous generator load line should be matched very closely to the maximum power line of the wind

Table 10.1: Parameters of the system.

Parameters	Values
Air density	1.2 kg/m <sup>3</sup>
Rotor radius	1.2 m
Inertia of the PMSG	0.0065 kg·m <sup>2</sup>
Flux linkage of the PMSG	0.5 V·s
Friction factor of the PMSG	0 N·m·s
Pole pairs of the PMSG	4
Inductances of the PMSG	4 mH
Resistances of the PMSG	0.135 Ω
DC bus voltage	400 V
DC bus capacitance	5000 μF
Inductances on the inverter side	2.2 mH
Inductances on the grid side	1.1 mH
Capacitances of the LCL filter	22 μF
Grid phase voltage (rms)	110 V
Switching frequency	5 kHz

turbine.

In a variable-speed wind turbine, the power  $P_w$  that can be obtained from wind is a cubic function of the wind speed  $v_w$ , i.e.,

$$P_m = \frac{1}{2}\rho\pi R^2 v_w^3 C_p, \quad (10.1)$$

where  $\rho$  is the air density;  $R$  is the turbine radius and  $C_p = f(\lambda, \beta)$  is the power coefficient that depends on the tip speed ratio  $\lambda$  of the wind turbine and the angle of the blades  $\beta$ . The tip speed ratio is defined as

$$\lambda = \frac{\omega_n R}{v_w},$$

where  $\omega_n$  is the rotor speed of the turbine. Consequently, for different wind speeds, the optimal values of the tip speed and the pitch angle need to be followed in order to achieve the maximum  $C_p$  and therefore the maximum power output. The maximum power of the wind turbine can be calculated as

$$P_m = \frac{1}{2}\rho\pi R^2 C_{pm} \left(\frac{R\omega_n}{\lambda_{opt}}\right)^3 = K_{opt}\omega_n^3,$$

where  $K_{opt} = \frac{1}{2}\rho\pi C_{pm} \left(\frac{R^5}{\lambda_{opt}^3}\right)$ . Taking the losses into account, the grid power reference

Table 10.2: Control parameters for the rotor-side converter.

Parameters	Values	Parameters	Values
$J_m$	0.0122	$K_p$	0.8
$D_{mp}$	6.0793	$K_i$	2
$K_m$	2430.1		

Table 10.3: Control parameters for the grid-side converter.

Parameters	Values	Parameters	Values
$J$	0.0122	$K$	2430.1
$D_p$	6.0793	$D_q$	386.7615

can be chosen to be slightly smaller than  $P_m$ . Here, this is chosen as

$$P_{ref} = 0.95K_{opt}\omega_n^3. \quad (10.2)$$

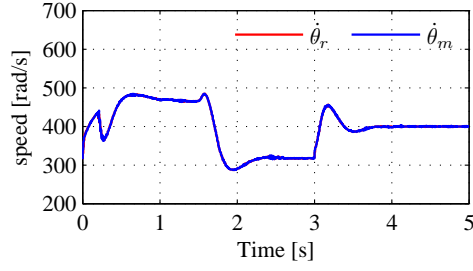
This reference can be passed to the synchronverter so that the right amount of power is fed into the grid. The proposed control strategy for the grid-side converter is shown in Figure 10.3, where the inductor current, the capacitor voltage and the grid voltage are denoted as  $i = [i_a \ i_b \ i_c]^T$ ,  $v = [v_a \ v_b \ v_c]^T$  and  $v_g = [v_{ga} \ v_{gb} \ v_{gc}]^T$ , respectively. This is very similar to the controller for the synchronverter [1], with the real power reference set as Equation (10.2). Because of the inherent capability of the synchronverter, this strategy is able to feed the real power to the grid while regulating the reactive power.

### 10.3 Simulation Results

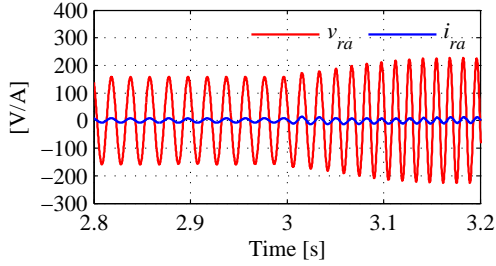
Simulations were carried out to verify the control strategy described above in Matlab 7.6/ Simulink/ SimpowerSystems. The solver used in the simulations was ode23t with a relative tolerance of  $10^{-3}$  and the sampling time was  $2 \mu s$ . The parameters of the system used in the simulations are given in Table 9.1.

The wind turbine extracts power from the wind and then converts it into mechanical power. The power coefficient  $C_p$  is calculated by using the following formula [23]:

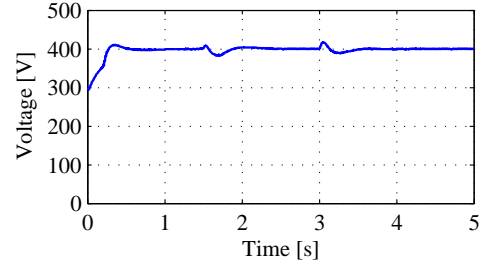
$$C_p(\lambda, \beta) = 0.22\left(\frac{116}{\beta} - 0.4 - 5\right)e^{-\frac{12.5}{\beta}}$$



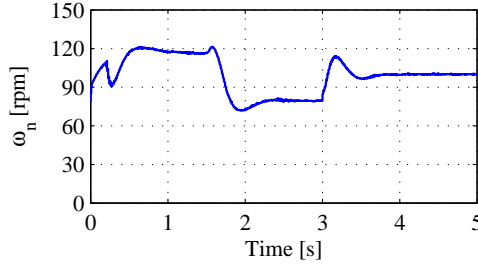
(a) Generator electric speed  $\dot{\theta}_r$  and the speed  $\dot{\theta}_m$  of the virtual synchronous machine



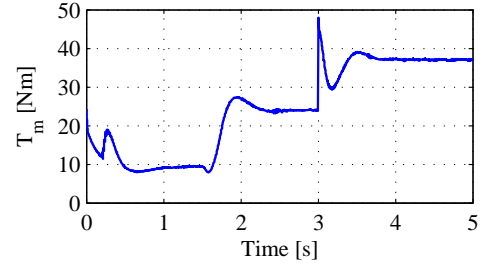
(b) Rotor-side phase voltage and current



(c) DC bus voltage



(d) Rotor speed



(e) Torque of the wind turbine

Figure 10.4: Performance of the rotor-side converter.

with

$$\beta = \frac{1}{\frac{1}{\lambda + 0.08\lambda} - \frac{0.035}{\lambda^3 + 1}}.$$

For the simulated wind turbine, the optimal tip speed ratio  $\lambda$  is 6.8 and the maximum power coefficient  $C_{pm}$  is 0.419.

### 10.3.1 Under the normal grid condition

The simulation was carried out according to the following sequence of actions:

- 1) start the system, but keep all the IGBTs off with the initial wind speed of 12m/s to establish the DC bus voltage first and then to synchronise with the grid, DC load  $R_{dc} = 150\Omega$ ;



2) start operating the IGBTs for both converters at  $t = 0.5\text{s}$  with  $V_{ref} = 400\text{V}$  and  $Q_{ref} = 0$  for the rotor-side converter and  $P_{ref} = 0$  and  $Q_{ref} = 0$  for the grid-side converter;

3) turn the circuit breaker on to connect to the grid at  $t = 0.8\text{s}$ .

4) set  $P_{ref} = 0.95K_{opt}\omega_n^3$  at  $t = 1.5\text{s}$  and disconnect DC load at the same time;

5) change the wind speed to  $15\text{m/s}$  at  $t = 3\text{s}$ .

It is worth noting that, in the real system, the grid-side converter should be turned on as soon as possible once the DC bus voltage is established. Otherwise, the wind-turbine generator works in the no-load mode. It could be damaged because the torque of the turbine is close to zero and the rotor speed might increase rapidly. In order to prevent this from happening in real applications, a DC load  $R_{dc}$  (damper) will be added onto the DC bus with a switch, which should be turned off when the grid side converter operates.

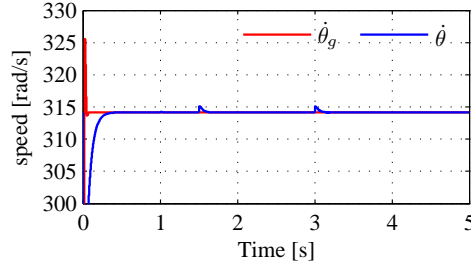
#### 10.3.1.1 Performance of the rotor-side converter

The parameters for the rotor-side converter are given in Table 10.2.

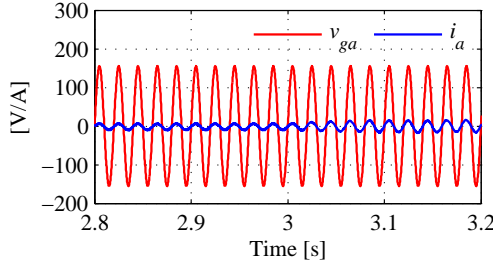
The responses of the rotor-side converter are shown in Figure 10.4. The DC bus voltage was maintained very well at  $400\text{V}$  after the system was connected to the grid. Obviously, the rotor-side converter worked under the variable-frequency-variable-amplitude mode and it well tracked the frequency of  $v_r$ , which is in proportion to the rotor speed. The current drawn by the rotor-side converter was in phase with the voltage and, hence, the reactive power  $Q_m$  was zero and the unity power factor was obtained.

#### 10.3.1.2 Performance of the grid-side converter

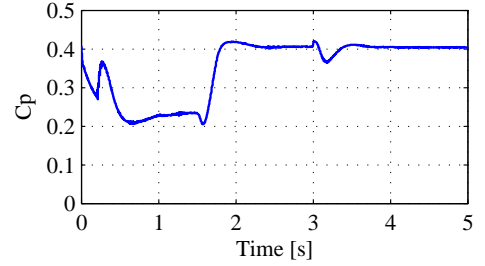
The parameters for the grid-side converter were given in Table 10.3, which were chosen to be largely the same as the ones for the rotor-side converter. The simulation results were shown in Figure 10.5. The power coefficient  $C_p$  was kept almost at maximum throughout, after connecting to the system, and the real power  $P$  tracked the reference power  $P_{ref}$  very well. Therefore, the maximum power point tracking was achieved by the grid-side converter.



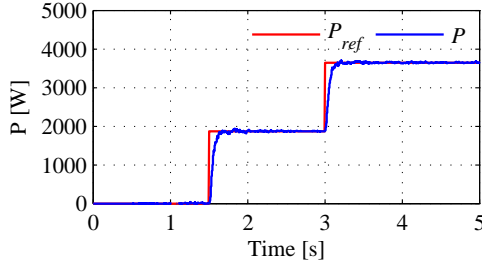
(a) Grid speed  $\dot{\theta}_g$  and the speed  $\dot{\theta}$  of the virtual synchronous machine



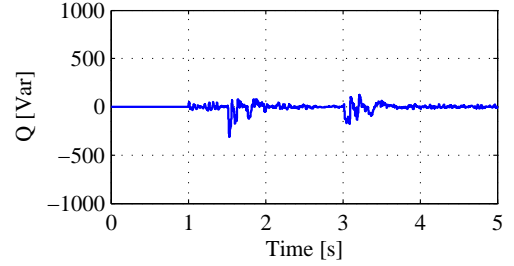
(b) Grid-side phase voltage and current



(c) Power coefficient of the wind turbine



(d) Power reference and real power



(e) Reactive power on grid-side converter

Figure 10.5: Performance of the grid-side converter.

### 10.3.2 Under grid voltage sags

Grid-voltage sags are transient dips in the grid operating voltage, ranging between 10% and 90% of the nominal value and lasting from a few milliseconds to a minute [132]. Faults resulting from voltage sags can occur on the distribution system or on the utility system. The new regulations on power grid operation require that wind turbine systems remain connected with the grid even in the situation of grid-voltage sags to help the system rapidly recover to the rated output after the fault clearance. Simulations were carried out to demonstrate the performance of the proposed control strategy in responding to voltage sags.

In the simulation, the sequence of actions was the same as in the previous case

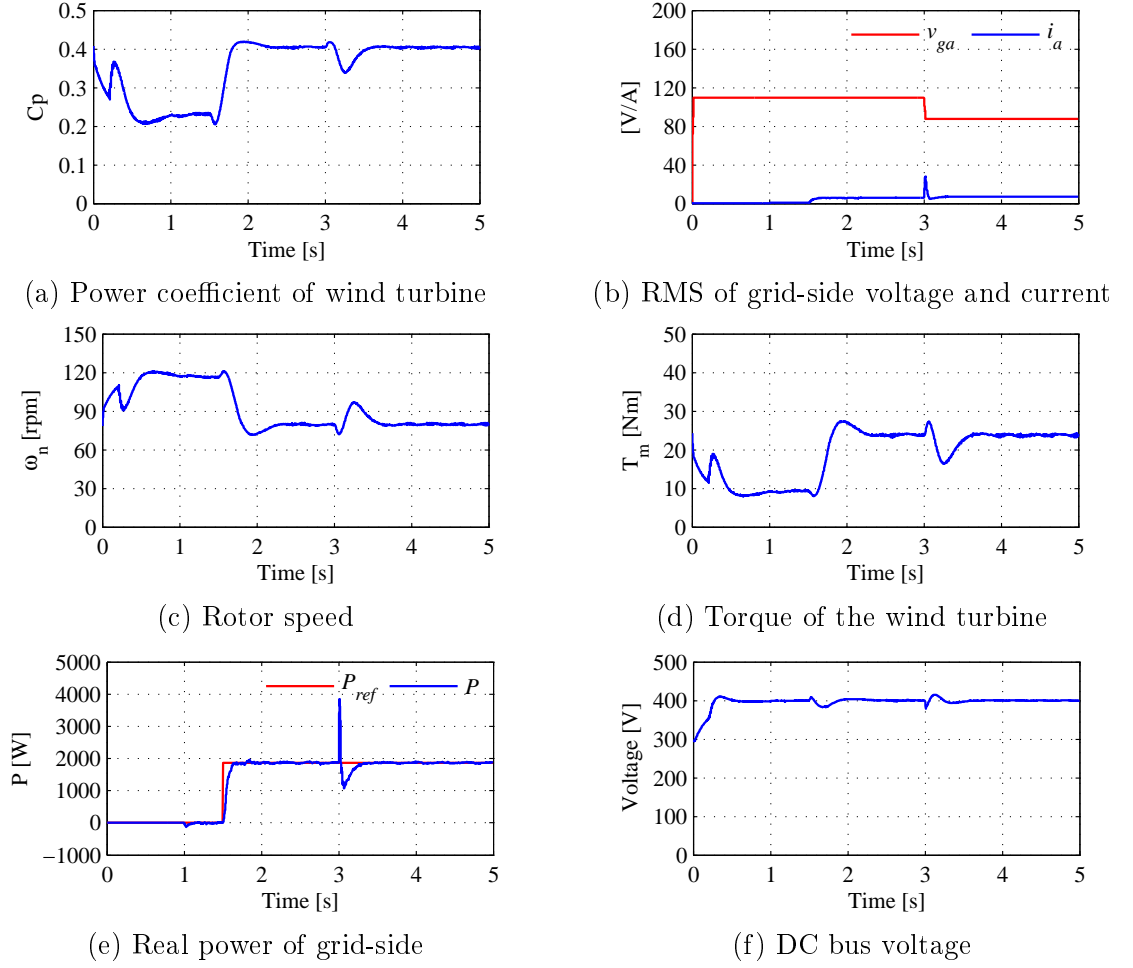


Figure 10.6: System responses during grid voltage sags.

except that the fifth action was replaced with the grid voltage drop of 20% at  $t = 3s$ .

The system responses are shown in Figure 10.6. The current of the grid side had a jump when the grid voltage dropped, but it quickly settled down at a value which was 20% higher. There was no noticeable change in the torque and the rotor speed, which meant that the wind turbine and the PMSG worked properly during the grid voltage sags. The DC bus voltage was controlled very well by the rotor-side converter and the maximum power coefficient was also maintained.

## 10.4 Conclusions

In this chapter, a synchronverter-based control strategy was proposed for back-to-back converters applied to a variable speed wind turbine with PMSG. This method is based on the DC bus voltage controlled by the generator side converter. The grid side converter controls the grid power according to the MPPT strategy. Moreover, the proposed control strategy improves the fault ride-through capability and causes the wind turbine to remain normal when the grid voltage sags. In order to validate the proposed control strategy, simulation results are provided.

## Chapter 11

# Conclusions and Further Work

### 11.1 Conclusions

Two of the most popular AC-DC-AC topologies for wind power with PMSG have been investigated in this thesis.

#### 11.1.1 Uncontrollable rectifier + boost converter + inverter

An experimental setup has been designed and built for this AC-DC-AC topology. Based on this experimental setup, a current control for maximum power point tracking without a mechanical sensor has been proposed. For constant excitation, the rotating speed of the generator is proportional to the peak output voltage and the torque of the machine is proportional to the peak output current. The output current of an uncontrollable rectifier can be controlled by a boost converter according to a current reference, which is determined by a climbing algorithm, to achieve MPPT.

An inverter is controlled according to the synchronverter technology to implement the grid-connection. It is able to send a set power to the grid and is also able to take part in the regulation of the system frequency and voltage. A controller based on synchronverters for parallel operation of inverters in the stand-alone mode has been proposed. Based on the droop method, the controller avoids the use of communication signals among the units. The control strategy consists of a frequency droop loop and a voltage droop loop which allows for the sharing of the real power and reactive power, respectively. The concept of capacitive output impedance is adopted to reduce the THD of the synchronverter's output voltage. Both simulation and experimental results have been provided.

### 11.1.2 Back-to-back converter

Synchronverter-based control strategies for three-phase rectifiers, which can possess most of the characteristics of conventional synchronous motors, have been proposed. Therefore, when PWM rectifiers are connected with the utility grid, the previous operation methods of the utility grid can still be used regardless of the particular load characteristics, and the stability of the utility grid can be improved accordingly. In the proposed schemes, the real power extracted from the source and the output voltage are the control variables, respectively, hence they can be employed in different applications. Furthermore, improved control schemes without the need of an extra synchronisation unit have been presented to reduce the computational burden of the controller.

Finally, a control strategy based on the synchronverter technology was proposed for the back-to-back PWM converter. Both converters are run as synchronverters, which are mathematically equivalent to the conventional synchronous machines. The rotor-side converter is responsible for maintaining the DC bus voltage and the grid-side converter is responsible for the Maximum Power Point Tracking.

## 11.2 Further Work

Based on the study carried out, various issues can be taken care of in further work, and are detailed below.

Firstly, synchronverter-based control strategies for three-phase rectifiers work in the simulations. However, the voltage and power used in the experiments in this work are very low. In order to validate the concept at real voltage and power ratings, the experiments should be carried out in a more realistic situations.

Secondly, the improved control strategies, which have no need of an extra synchronisation unit, have not been applied in back-to-back converters. These control strategies should work on the grid-side because of the nearly constant frequency of the utility grid. On the rotor-side, the frequency of the generator output voltage is no longer constant. Further work should focus on the parameter selection to allow three-phase rectifiers to track the generator frequency properly.

Thirdly, various strategies have been proposed to control PWM rectifiers or inverters. These strategies can achieve the same major goals, such as a high power factor and near-sinusoidal current waveforms, but they are often based on different principles, such as d-p transformation, VOC, PWM and so on. An overall comparison between them should

be given to point out advantages and disadvantages for each other so that we are able to know which strategy is most appropriate way in different situations and requirements.

Fourthly, most of experiments have been implemented in ideal conditions. But there are large numbers of extreme cases in realistic situations. If we want to apply this way into practice, many experiments and research should be done to know the fault tolerance of system in different extreme cases.

Moreover, robust control is a branch of control theory that explicitly deals with uncertainty in its approach to controller design. Robust control methods are designed to function properly so long as uncertain parameters or disturbances are within some set. Robust methods aim to achieve robust performance and/or stability in the presence of bounded modeling errors. Further research about parameters variation should be investigated. For example, because there is no delay involved in the frequency droop loop, the time constant can be made much smaller than for a real SG. It is not necessary to have a large inertia as with a physical SG, where a larger inertia means that more energy is stored mechanically. Whether a small inertia is good for overall grid stability is an open question for later research.

Finally, in this work, the prototype of the control strategy for wind power is presented, however many details could be improved in realistic situations. For example, MPPT tracking based only on the wind speed is not realistic, since it is difficult to obtain a realistic value for it. A new experimental setup for the back-to-back converter could be designed and relevant experiments carried out in realistic environments.

# References

- [1] Q.-C. Zhong and G. Weiss. Synchronverters: Inverters that mimic synchronous generators. *IEEE Trans. Ind. Electron.*, 58(4):1259–1267, Apr. 2011.
- [2] H.-J. Wagner and J. Mathur. *Introduction to wind energy systems: basics, technology and operation*. Springer-Verlag, 2009.
- [3] S. Mathew. *Wind energy : fundamentals, resource analysis and economics*. Springer-Verlag, 2006.
- [4] T. Burton. *Wind energy: handbook*. John Wiley & Sons, 2001.
- [5] S. Heier. *Grid integration of wind energy conversion systems*. John Wiley & Sons, 2006.
- [6] J.F. Manwell, J.G. McGowan, and A.L. Rogers. *Wind Energy Explained: Theory, Design and Application*. John Wiley & Sons, 2009.
- [7] D.A. Spera. *Wind turbine technology: fundamental concepts of wind turbine engineering*. ASME Press, 2009.
- [8] M. Tazil, V. Kumar, R. C. Bansal, S. Kong, Z. Y. Dong, W. Freitas, and H. D. Mathur. Three-phase doubly fed induction generators: An overview. *IET Proc. Electric Power Appl.*, 4(2):75–89, 2010.
- [9] J. Ekanayake, L. Holdsworth, and N. Jenkins. Control of DFIG wind turbines. *Power Engineer*, 17(1):28–32, Feb. 2003.
- [10] J.A. Baroudi, V. Dinavahi, and A.M. Knight. A review of power converter topologies for wind generators. In *Proc. of IEEE International Conference on Electric Machines and Drives*, pages 458–465, May 2005.



- [11] F.D. Bianchi, H.D. Battista, and R.J. Mantz. *Wind turbine control systems: principles, modelling and gain scheduling design*. Springer-Verlag, 2007.
- [12] S. Mathew and G.S. Philip. *Advances in wind energy and conversion technology*. Springer-Verlag, 2011.
- [13] T. Tanaka, T. Toumiya, and T. Suzuki. Output control by hill-climbing method for a small scale wind power generating system. *Renewable Energy*, 12(4):387–400, Jul. 1997.
- [14] M.G. Simoes, B.K. Bose, and R.J. Spiegel. Fuzzy logic based intelligent control of a variable speed cage machine wind generation system. In *Proc. of Power Electronics Specialists Conference (PESC)*, pages 389–395, 1995.
- [15] K. Tan and S. Islam. Optimum control strategies in energy conversion of pmsg wind turbine system without mechanical sensors. *IEEE Trans. Energy Convers.*, 19(2):392–399, Jun. 2004.
- [16] Quincy Wang and Liuchen Chang. An intelligent maximum power extraction algorithm for inverter-based variable speed wind turbine systems. *IEEE Trans. Power Del.*, 19(5):1242–1249, Sept. 2004.
- [17] R. Datta and V.T. Ranganathan. A method of tracking the peak power points for a variable speed wind energy conversion system. *IEEE Power Eng. Rev.*, 22(10):57–57, Oct. 2002.
- [18] E. Koutroulis and K. Kalaitzakis. Design of a maximum power tracking system for wind-energy-conversion applications. *IEEE Trans. Ind. Electron.*, 53(2):486–494, Apr. 2006.
- [19] Ying-Yi Hong, Shiue-Der Lu, and Ching-Sheng Chiou. MPPT for PM wind generator using gradient approximation. *Energy Conversion and Management*, 50(1):82–89, Aug. 2009.
- [20] M.E. Haque, K.M. Muttaqi, and M. Negnevitsky. Control of a standalone variable speed wind turbine with a permanent magnet synchronous generator. In *Proc. of the 21st Power and Energy Society General Meeting*, pages 1–9, 2008.

- [21] K. Amei, Y. Takayasu, T. Ohji, and M. Sakui. A maximum power control of wind generator system using a permanent magnet synchronous generator and a boost chopper circuit. In *Proc. of Power Conversion Conference (PCC)*, pages 1447–1452, 2002.
- [22] A.B. Kulkarni and M. Ehsani. A novel position sensor elimination technique for the interior permanent-magnet synchronous motor drive. In *Proc. of Industry Applications Society Annual Meeting*, pages 773–779, 1989.
- [23] Tao Sun, Zhe Chen, and F. Blaabjerg. Voltage recovery of grid-connected wind turbines after a short-circuit fault. In *Proc. of Industrial Electronics Society (IECON)*, pages 2723–2728, 2003.
- [24] E. Figueres, G. Garcera, J. Sandia, F. Gonzalez-Espin, and J.C. Rubio. Sensitivity study of the dynamics of three-phase photovoltaic inverters with an lcl grid filter. *IEEE Trans. Ind. Electron.*, 56(3):706–717, Mar. 2009.
- [25] S. Alepuz, S. Busquets-Monge, J. Bordonau, J. Gago, D. Gonzalez, and J. Balcells. Interfacing renewable energy sources to the utility grid using a three-level inverter. *IEEE Trans. Ind. Electron.*, 53(5):1504–1511, Oct. 2006.
- [26] J.M. Espi Huerta, J. Castello-Moreno, J.R. Fischer, and R. Garcia-Gil. A synchronous reference frame robust predictive current control for three-phase grid-connected inverters. *IEEE Trans. Ind. Electron.*, 57(3):954–962, Mar. 2010.
- [27] B. Sahan, A.N. Vergara, N. Henze, A. Engler, and P. Zacharias. A single-stage PV module integrated converter based on a low-power current-source inverter. *IEEE Trans. Ind. Electron.*, 55(7):2602–2609, Jul. 2008.
- [28] J.M. Espi, J. Castello, R. GarciŽ anda Gil, G. Garcera, and E. Figueres. An adaptive robust predictive current control for three-phase grid-connected inverters. *IEEE Trans. Ind. Electron.*, 58(8):3537–3546, Aug. 2011.
- [29] R. Kadri, J.-P. Gaubert, and G. Champenois. An improved maximum power point tracking for photovoltaic grid-connected inverter based on voltage-oriented control. *IEEE Trans. Ind. Electron.*, 58(1):66–75, Jan. 2011.

- [30] M.P. Kazmierkowski and L. Malesani. Current control techniques for three-phase voltage-source pwm converters: a survey. *IEEE Trans. Ind. Electron.*, 45(5):691–703, Oct. 1998.
- [31] Lidong Zhang, L. Harnefors, and H.-P. Nee. Power-synchronization control of grid-connected voltage-source converters. *IEEE Trans. Power Syst.*, 25(2):809–820, May 2010.
- [32] Theodore Wildi. *Electrical Machines, Drives and Power Systems*. Prentice-Hall, 6 edition, 2005.
- [33] A. Cetin and M. Ermis. VSC-Based D-STATCOM with selective harmonic elimination. *IEEE Trans. Ind. Appl.*, 45(3):1000–1015, may-jun 2009.
- [34] B. Singh, R. Saha, A. Chandra, and K. Al-Haddad. Static synchronous compensators (STATCOM): A review. *IET Proc. Power Electron.*, 2(4):297–324, Jul. 2009.
- [35] H.-P. Beck and R. Hesse. Virtual synchronous machine. In *Proc. of the 9th International Conference on Electrical Power Quality and Utilisation (EPQU)*, pages 1–6, 2007.
- [36] J. Driesen and K. Visscher. Virtual synchronous generators. In *Proc. of IEEE Power and Energy Society General Meeting*, pages 1–3, 2008.
- [37] K. Visscher and S.W.H. De Haan. Virtual synchronous machines (VSG’s) for frequency stabilisation in future grids with a significant share of decentralized generation. In *Proc. of IET-CIRED Seminar on Smart Grids for Distribution*, pages 1–4, 2008.
- [38] M. Torres and L. A. C. Lopes. Frequency control improvement in an autonomous power system: An application of virtual synchronous machines. In *Proc. of the 8th IEEE International Conference on Power Electronics and ECCE Asia (ICPE & ECCE)*, pages 2188–2195, 2011.
- [39] Y. Chen, R. Hesse, D. Turschner, and H.-P. Beck. Improving the grid power quality using virtual synchronous machines. In *Proc. of International Conference on Power Engineering, Energy and Electrical Drives (POWERENG)*, pages 1–6, 2011.

- [40] Q.-C. Zhong and G. Weiss. Static synchronous generators for distributed generation and renewable energy. In *Proc. of IEEE PES Power Systems Conference & Exhibition (PSCE)*, 2009.
- [41] R.H. Lasseter. Microgrids. In *Proc. of IEEE Power Engineering Society Winter Meeting*, pages 305–308, 2002.
- [42] Tomas Hornik. *Power quality in microgrids*. PhD thesis, University of Liverpool, Liverpool, UK, 2010.
- [43] F. Katiraei, R. Iravani, N. Hatziargyriou, and A. Dimeas. Microgrids management. *IEEE Power Energy Mag.*, 6(3):54–65, May/Jun. 2008.
- [44] C. Xiarnay, H. Asano, S. Papathanassiou, and G. Strbac. Policymaking for microgrids. *IEEE Power Energy Mag.*, 6(3):66–77, May/Jun. 2008.
- [45] H. Nikkhaioei and R.H. Lasseter. Distributed generation interface to the CERTS microgrid. *IEEE Trans. Power Del.*, 24(3):1598–1608, Jul. 2009.
- [46] Shiguo Luo, Zhihong Ye, Ray-Lee Lin, and F.C. Lee. A classification and evaluation of paralleling methods for power supply modules. In *Power Electronics Specialists Conference, 1999. PESC 99. 30th Annual IEEE*, pages 901 –908 vol.2, 1999.
- [47] C.S. Lee, S. Kim, C.B. Kim, S.C. Hong, J.S. Yoo, S.W. Kim, C.H. Kim, S.H. Woo, and S.Y. Sun. Parallel ups with a instantaneous current sharing control. In *Industrial Electronics Society, 1998. IECON '98. Proceedings of the 24th Annual Conference of the IEEE*, pages 568 –573 vol.1, Aug 1998.
- [48] Jiann-Fuh Chen and Ching-Lung Chu. Combination voltage-controlled and current-controlled pwm inverters for ups parallel operation. *Power Electronics, IEEE Transactions on*, 10:547 –558, Sept 1995.
- [49] T. Kawabata and S. Higashino. Parallel operation of voltage source inverters. *Industry Applications, IEEE Transactions on*, 24(2):281 –287, mar/apr 1988.
- [50] A.P. Martins, A.S. Carvalho, and A.S. Araujo. Design and implementation of a current controller for the parallel operation of standard upss. In *Industrial Electronics, Control, and Instrumentation, 1995., Proceedings of the 1995 IEEE*

- IECON 21st International Conference on*, volume 1, pages 584 –589 vol.1, Nov 1995.
- [51] Tsai-Fu Wu, Yu-Kai Chen, and Yong-Heh Huang. 3c strategy for inverters in parallel operation achieving an equal current distribution. *Industrial Electronics, IEEE Transactions on*, 47(2):273 –281, Apr 2000.
  - [52] J.M. Guerrero, L. Garcia de Vicuna, J. Matas, and J. Castilla, M. and Miret. Output impedance design of parallel-connected UPS inverters with wireless load-sharing control. *IEEE Trans. Ind. Electron.*, 52(4):1126–1135, May. 2005.
  - [53] J.M. Guerrero, J. Matas, Luis Garcia de Vicuna, M. Castilla, and J. Miret. Decentralized control for parallel operation of distributed generation inverters using resistive output impedance. *IEEE Trans. Ind. Electron.*, 54(2):994–1004, Nov. 2007.
  - [54] E. Barklund, N. Pogaku, M. Prodanovic, C. Hernandez-Aramburo, and T.C. Green. Energy management in autonomous microgrid using stability-constrained droop control of inverters. *IEEE Trans. Power Electron.*, 23(5):2346–2352, Sept. 2008.
  - [55] Y. Mohamed and E.F. El-Saadany. Adaptive decentralized droop controller to preserve power sharing stability of paralleled inverters in distributed generation microgrids. *IEEE Trans. Power Electron.*, 23(6):2806–2816, Nov. 2008.
  - [56] J. M. Guerrero, J. C. Vasquez, J. matas, L. Garcia de Vicuna, and M. Castilla. Hierarchical control of droop-controlled AC and DC microgrids- a general approach towards standardization. *IEEE Trans. Ind. Electron.*, 58(1):158–172, Jan. 2011.
  - [57] A. Tuladhar, H. Jin, T. Unger, and K. Mauch. Parallel operation of single phase inverter modules with no control interconnections. In *Proc. of the 12th IEEE Applied Power Electronics Conference and Exposition*, pages 94–100, 1997.
  - [58] R. Majumder, B. Chaudhuri, A. Ghosh, G. Ledwich, and F. Zare. Improvement of stability and load sharing in an autonomous microgrid using supplementary droop control loop. *IEEE Trans. Power Syst.*, 25(2):796–808, May 2010.

- [59] K. De Brabandere, B. Bolsens, J. Van den Keybus, A. Woyte, J. Driesen, and R. Belmans. A voltage and frequency droop control method for parallel inverters. *IEEE Trans. Power Electron.*, 22(4):1107–1115, Jul. 2007.
- [60] G. Diaz, C. Gonzalez-Moran, J. Gomez-Alexandre, and A. Diez. Scheduling of droop coefficients for frequency and voltage regulation in isolated microgrids. *IEEE Trans. Power Syst.*, 25(1):489–496, Feb. 2010.
- [61] M.C. Chandorkar, D.M. Divan, and R. Adapa. Control of parallel connected inverters in standalone AC supply systems. *IEEE Trans. Ind. Appl.*, 29(1):136–143, Jan./Feb. 1993.
- [62] U. Borup, F. Blaabjerg, and P.N. Enjeti. Sharing of nonlinear load in parallel-connected three-phase converters. *IEEE Trans. Ind. Appl.*, 37(6):1817–1823, Nov./Dec. 2001.
- [63] E.A.A. Coelho, P.C. Cortizo, and P.F.D. Garcia. Small-signal stability for parallel-connected inverters in stand-alone AC supply systems. *IEEE Trans. Ind. Appl.*, 38(2):533–542, Oct. 2002.
- [64] J.M. Guerrero, L.G. de Vicuna, J. Miret, J. Matas, and J. Cruz. Output impedance performance for parallel operation of UPS inverters using wireless and average current-sharing controllers. In *Proc. of the 35th IEEE Power Electronics Specialists Conference*, pages 2482–2488, 2004.
- [65] J.M. Guerrero, N. Berbel, L.G. de Vicuna, J. Matas, J. Miret, and M. Castilla. Droop control method for the parallel operation of online uninterruptible power systems using resistive output impedance. In *Proc. of the 21st IEEE Applied Power Electronics Conference and Exposition*, pages 1716–1722, 2006.
- [66] A. Tuladhar, Hua Jin, T. Unger, and K. Mauch. Control of parallel inverters in distributed AC power systems with consideration of line impedance effect. *IEEE Trans. Ind. Appl.*, 36(1):131–138, Jan./Feb. 2000.
- [67] Chien-Liang Chen, Yubin Wang, Jih-Sheng Lai, Yuang-Shung Lee, and D. Martin. Design of parallel inverters for smooth mode transfer microgrid applications. *IEEE Trans. Power Electron.*, 25(1):6–15, Feb. 2010.

- [68] T. Ackerman. *Wind Power in Power Systems*. Chichester: John Wiley & Sons, Ltd., 2005.
- [69] F. Blaabjerg, Z. Chen, and S.B. Kjaer. Power electronics as efficient interface in dispersed power generation systems. *IEEE Trans. Power Electron.*, 19(5):1184–1194, Sept. 2004.
- [70] F. Blaabjerg, F. Iov, R. Teodorescu, and Z. Chen. Power electronics in renewable energy systems. In *Proc. of the 12th International Power Electronics and Motion Control Conference (EPE-PEMC)*, pages 1–17, 2006.
- [71] G. Weiss, Q.-C. Zhong, T. Green, and J. Liang.  $H^\infty$  repetitive control of DC-AC converters in micro-grids. *IEEE Trans. Power Electron.*, 19(1):219–230, Jan. 2004.
- [72] J.M. Guerrero, J.C. Vasquez, J. Matas, M. Castilla, and L.G. de Vicuna. Control strategy for flexible microgrid based on parallel line-interactive UPS systems. *IEEE Trans. Ind. Electron.*, 56(3):726–736, Mar. 2009.
- [73] S. V. Iyer, M. N. Belur, and M. C. Chandorkar. A generalized computational method to determine stability of a multi-inverter microgrid. *IEEE Trans. Power Electron.*, 25(9):2420–2432, Sept. 2010.
- [74] T. Hornik and Q.-C. Zhong. A current control strategy for voltage-source inverters in microgrids based on  $H^\infty$  and repetitive control. *IEEE Trans. Power Electron.*, 26(3):943–952, Mar. 2011.
- [75] N. Yousefpoor, S. Fathi, N. Farokhnia, and H. Askarian Abyaneh. THD minimization applied directly on the line to line voltage of multi-level inverters. *IEEE Trans. Ind. Electron.*, 59(1):373–380, Jan. 2012.
- [76] A. V. Timbus, R. Teodorescu, F. Blaabjerg, M. Liserre, and P. Rodriguez. Linear and nonlinear control of distributed power generation systems. In *Proc. of IEEE Industry Applications Conference*, pages 1015–1023, 2006.
- [77] F. Blaabjerg, R. Teodorescu, M. Liserre, and A.V. Timbus. Overview of control and grid synchronization for distributed power generation systems. *IEEE Trans. Ind. Electron.*, 53(5):1398–1409, Oct. 2006.

- [78] Y.-Y. Tzou, S.-L. Jung, and H.-C. Yeh. Adaptive repetitive control of PWM inverters for very low THD AC-voltage regulation with unknown loads. *IEEE Trans. Power Electron.*, 14(5):973–981, Sept. 1999.
- [79] T. Hornik and Q.-C. Zhong. Voltage control of grid-connected inverters based on  $h^\infty$  and repetitive control. In *Proc. of the 8th World Congress on Intelligent Control and Automation (WCICA)*, pages 270–275, 2010.
- [80] B.A. Francis and W.M. Wonham. The internal model principle for linear multi-variable regulators. *Applied Mathematics and Optimization*, 2(2):170–194, 1975.
- [81] A. Garcia-Cerrada, O. Pinzon-Ardila, V. Feliu-Batlle, P. Roncero-Sanchez, and P. Garcia-Gonzalez. Application of a repetitive controller for a three-phase active power filter. *IEEE Trans. Power Electron.*, 22(1):237–246, Jan. 2007.
- [82] R. Costa-Castello, R. Grino, R. Cardoner, and E. Fossas. High performance control of a single-phase shunt active filter. In *Proc. of IEEE International Symposium on Industrial Electronics (ISIE)*, pages 3350–3355, 2007.
- [83] T. Hornik and Q.-C. Zhong.  $H^\infty$  repetitive voltage control of grid-connected inverters with frequency adaptive mechanism. *IET Proc. Power Electron.*, 3(6):925–935, Nov. 2010.
- [84] F. Khatounian, E. Monmasson, F. Berthereau, E. Delaleau, and J.P. Louis. Control of a doubly fed induction generator for aircraft application. In *Proc. of the 29th Annual Conference of the IEEE Industrial Electronics Society*, pages 2711–2716, 2003.
- [85] F. Khatounian, E. Monmasson, F. Berthereau, and J.P. Louis. Design of an output LC filter for a doubly fed induction generator supplying non-linear loads for aircraft applications. In *Proc. of IEEE International Symposium on Industrial Electronics (ISIE)*, pages 1093–1098, 2004.
- [86] J. Mazumdar, I. Batarseh, N. Kutkut, and O. Demirci. High frequency low cost DC-AC inverter design with fuel cell source for home applications. In *Proc. of the 37th IAS Annual Meeting and World Conference on Industrial applications of Electrical Energy*, pages 789–794, 2002.



- [87] H.W. Klessner, S.W.H. de Haan, and J.B. Woudstra. Analysis of a controllable LC-filter for compensation of specific harmonics. In *Proc. of Power Electronic Drives and Energy Systems for Industrial Growth*, pages 588–591 Vol. 2, 1998.
- [88] Timothy C.Y. Wang, Zhihong Ye, Gautam Sinha, and Xiaoming Yuan. Output filter design for a grid-interconnected three-phase inverter. In *Proc. of the 34th Annual IEEE Power Electronics Specialists Conference*, volume 2, pages 779–784, 2003.
- [89] Q.-C. Zhong and Y. Zeng. Can the output impedance of an inverter be designed capacitive? In *Proc. of the 37th Annual IEEE Conference of Industrial Electronics (IECON)*, 2011.
- [90] Q.-C. Zhong and Y. Zeng. Inverters with optimal capacitive output impedances to minimise the output voltage THD. under review.
- [91] Q.-C. Zhong, F. Blaabjerg, J.M. Guerrero, and T. Hornik. Reduction of voltage harmonics for parallel-operated inverters. In *Proc. of IEEE Energy Conversion Congress and Exposition (ECCE)*, pages 473–478, 2011.
- [92] Guoqiao Shen, Xuancai Zhu, Jun Zhang, and Dehong Xu. A new feedback method for PR current control of LCL-filter-based grid-connected inverter. *IEEE Trans. Ind. Electron.*, 57(6):2033–2041, Jun. 2010.
- [93] T. Ericksen, N. Hingorani, and Y. Khersonsky. Power electronics and future marine electrical systems. *IEEE Trans. Ind. Appl.*, 42(1):155 – 163, Feb. 2006.
- [94] J.R. Rodriguez, J.W. Dixon, J.R. Espinoza, J. Pontt, and P. Lezana. PWM regenerative rectifiers: State of the art. *IEEE Trans. Ind. Electron.*, 52(1):5–22, Feb. 2005.
- [95] M. Cichowlas, M. Malinowski, M.P. Kazmierkowski, D.L. Sobczuk, P. Rodriguez, and J. Pou. Active filtering function of three-phase PWM boost rectifier under different line voltage conditions. *IEEE Trans. Ind. Electron.*, 52(2):410–419, Apr. 2005.
- [96] J.W. Dixon and Boon-Teck Ooi. Indirect current control of a unity power factor sinusoidal current boost type three-phase rectifier. *IEEE Trans. Ind. Electron.*, 35(4):508–515, Nov. 1988.

- [97] S. Hansen, M. Malinowski, F. Blaabjerg, and M.P. Kazmierkowski. Sensorless control strategies for PWM rectifier. In *Proc. of Applied Power Electronics Conference and Exposition (APEC)*, pages 832–838, 2000.
- [98] K. Zhou and D. Wang. Digital repetitive controlled three-phase PWM rectifier. *IEEE Trans. Power Electron.*, 18(1):309–316, Jan. 2003.
- [99] J.L. Duarte, A. Van Zwam, C. Wijnands, and A. Vandenput. Reference frames fit for controlling PWM rectifiers. *IEEE Trans. Ind. Electron.*, 46(3):628–630, Jun. 1999.
- [100] M.P. Kazmierkowski and L. Malesani. Current control techniques for three-phase voltage-source PWM converters: A survey. *IEEE Trans. Ind. Electron.*, 45(5):691–703, Oct. 1998.
- [101] Dong-Choon Lee and Dae-Sik Lim. AC voltage and current sensorless control of three-phase PWM rectifiers. *IEEE Power Electron. Lett.*, 17(6):883 – 890, Nov. 2002.
- [102] C. Cecati, A. Dell’Aquila, A. Lecci, and M. Liserre. Implementation issues of a fuzzy-logic-based three-phase active rectifier employing only voltage sensors. *IEEE Trans. Ind. Electron.*, 52(2):378 – 385, Apr. 2005.
- [103] Z. Zhou, P.J. Unsworth, P.M. Holland, and P. Igic. Design and analysis of a feed-forward control scheme for a three-phase voltage source pulse width modulation rectifier using sensorless load current signal. *IET Proc. Power Electron.*, 2(4):421–430, Jul. 2009.
- [104] T. Noguchi, H. Tomiki, S. Kondo, and I. Takahashi. Direct power control of PWM converter without power-source voltage sensors. *IEEE Trans. Ind. Appl.*, 34(3):473–479, May/Jun. 1998.
- [105] M. Malinowski, M.P. Kazmierkowski, S. Hansen, F. Blaabjerg, and G.D. Marques. Virtual-flux-based direct power control of three-phase PWM rectifiers. *IEEE Trans. Ind. Appl.*, 37(4):1019–1027, Jul./Aug. 2001.
- [106] G. Escobar, A.M. Stankovic, J.M. Carrasco, E. Galvan, and R. Ortega. Analysis and design of direct power control (DPC) for a three-phase synchronous rectifier

- via output regulation subspaces. *IEEE Trans. Power Del.*, 18(3):823–830, May 2003.
- [107] M. Malinowski, M. Jasinski, and M.P. Kazmierkowski. Simple direct power control of three-phase PWM rectifier using space-vector modulation (DPC-SVM). *IEEE Trans. Ind. Electron.*, 51(2):447–454, Apr. 2004.
  - [108] B.S. Chen and G. Joos. Direct power control of active filters with averaged switching frequency regulation. *IEEE Trans. Power Del.*, 23(6):2729–2737, Nov. 2008.
  - [109] Shan Dong-liang, Song Shu-zhong, Ma Jian-wei, and Wang Xian-bo. Direct power control of PWM rectifiers based on virtual flux. In *Proc. of the International Conference on Computer Application and System Modeling (ICCASM)*, pages 613–616, 2010.
  - [110] A. K. Ziarani and A. Konrad. A method of extraction of nonstationary sinusoids. *Signal Processing*, 84(8):1323–1346, Apr. 2004.
  - [111] Z. Ma, Q.-C. Zhong, and J. Yan. Synchronverter-based control strategies for three-phase PWM rectifiers. In *Proc. of the 7th IEEE Conference on Industrial Electronics and Applications (ICIEA)*, Singapore, Jul. 2012.
  - [112] S.-K. Chung. Phase-locked loop for grid-connected three-phase power conversion systems. *IEE Proc. Electric Power Appl.*, 147(3):213–219, May 2000.
  - [113] D. Jovcic. Phase locked loop system for FACTS. *IEEE Trans. Power Syst.*, 18(3):1116–1124, Aug. 2003.
  - [114] R.M. Santos Filho, P.F. Seixas, P.C. Cortizo, L.A.B. Torres, and A.F. Souza. Comparison of three single-phase PLL algorithms for UPS applications. *IEEE Trans. Ind. Electron.*, 55(8):2923–2932, Aug. 2008.
  - [115] C.H. da Silva, R.R. Pereira, L.E.B. da Silva, G. Lambert-Torres, B.K. Bose, and S.U. Ahn. A digital PLL scheme for three-phase system using modified synchronous reference frame. *IEEE Trans. Ind. Electron.*, 57(11):3814–3821, Nov. 2010.

- [116] M. Karimi Ghartemani, A. khajehoddin, P. Jain, and A. Bakhshai. Problems of startup and phase jumps in PLL systems. *IEEE Trans. Power Electron.*, PP(99):1, Sept. 2011.
- [117] Y.F. Wang and Y.W. Li. Grid synchronization PLL based on cascaded delayed signal cancellation. *IEEE Trans. Power Electron.*, 26(7):1987–1997, Jul. 2011.
- [118] Dong Dong, D. Boroyevich, P. Mattavelli, and I. Cvetkovic. A high-performance single-phase phase-locked-loop with fast line-voltage amplitude tracking. In *Proc. of the 26th Annual IEEE Applied Power Electronics Conference and Exposition (APEC)*, pages 1622–1628, 2011.
- [119] G. Escobar, M.F. Martinez-Montejano, A.A. Valdez, P.R. Martinez, and M. Hernandez-Gomez. Fixed-reference-frame phase-locked loop for grid synchronization under unbalanced operation. *IEEE Trans. Ind. Electron.*, 58(5):1943–1951, May 2011.
- [120] Xiaoqiang Guo, Weiyang Wu, and Zhe Chen. Multiple-complex coefficient-filter-based phase-locked loop and synchronization technique for three-phase grid-interfaced converters in distributed utility networks. *IEEE Trans. Ind. Electron.*, 58(4):1194–1204, Apr. 2011.
- [121] L. Harnefors, M. Bongiorno, and S. Lundberg. Input-admittance calculation and shaping for controlled voltage-source converters. *IEEE Trans. Ind. Electron.*, 54(6):3323–3334, Dec. 2007.
- [122] D. Jovcic, L.A. Lamont, and L. Xu. VSC transmission model for analytical studies. In *Proc. of IEEE Power Engineering Society General Meeting*, volume 3, pages 1737–1742, Jul. 2003.
- [123] R. Pena, J.C. Clare, and G.M. Asher. Doubly fed induction generator using back-to-back PWM converters and its application to variable-speed wind-energy generation. *IEE Proc. Electric Power Appl.*, 143(3):231–241, May 1996.
- [124] R. Pena, J.C. Clare, and G.M. Asher. A doubly fed induction generator using back-to-back PWM converters supplying an isolated load from a variable speed wind turbine. *IEE Proc. Electric Power Appl.*, 143(5):380–387, Sept. 1996.

- [125] R. Cardenas and R. Pena. Sensorless vector control of induction machines for variable-speed wind energy applications. *IEEE Trans. Energy Convers.*, 19(1):196–205, Mar. 2004.
- [126] R. Teodorescu and F. Blaabjerg. Flexible control of small wind turbines with grid failure detection operating in stand-alone and grid-connected mode. *IEEE Trans. Power Electron.*, 19(5):1323–1332, Sept. 2004.
- [127] R.C. Portillo, M.M. Prats, J.I. Leon, J.A. Sanchez, J.M. Carrasco, E. Galvan, and L.G. Franquelo. Modeling strategy for back-to-back three-level converters applied to high-power wind turbines. *IEEE Trans. Ind. Electron.*, 53(5):1483–1491, Oct. 2006.
- [128] E.J. Bueno, S. Cobrecas, F.J. Rodriguez, A. Hernandez, and F. Espinosa. Design of a back-to-back NPC converter interface for wind turbines with squirrel-cage induction generator. *IEEE Trans. Energy Convers.*, 23(3):932–945, Sept. 2008.
- [129] M. Singh, V. Khadkikar, and A. Chandra. Grid synchronisation with harmonics and reactive power compensation capability of a permanent magnet synchronous generator-based variable speed wind energy conversion system. *IET Proc. Power Electron.*, 4(1):122–130, Jan. 2011.
- [130] O. Gomis-Bellmunt, A. Junyent-Ferre, A. Sumper, and J. Bergas-Jan. Ride-through control of a doubly fed induction generator under unbalanced voltage sags. *IEEE Trans. Energy Convers.*, 23(4):1036–1045, Dec. 2008.
- [131] M.F. McGranaghan, D.R. Mueller, and M.J. Samotyj. Voltage sags in industrial systems. *IEEE Trans. Ind. Appl.*, 29(2):397–403, Mar./Apr. 1993.
- [132] Math H. Bollen. *Understanding Power Quality Problems: Voltage Sags and Interruptions*. Wiley-IEEE Press, 2000.
- [133] Xibo Yuan, Fei Wang, D. Boroyevich, Yongdong Li, and R. Burgos. DC-link voltage control of a full power converter for wind generator operating in weak-grid systems. *IEEE Trans. Power Del.*, 24(9):2178–2192, Sept. 2009.
- [134] A.D. Hansen and G. Michalke. Multi-pole permanent magnet synchronous generator wind turbines’ grid support capability in uninterrupted operation during grid faults. *IET Proc. Renewable Power Generation*, 3(3):333–348, Sept. 2009.

- [135] Ki-Hong Kim, Yoon-Cheul Jeung, Dong-Choon Lee, and Heung-Geun Kim. Robust control of PMSG wind turbine systems with back-to-back PWM converters. In *Proc. of the 2nd Power Electronics for Distributed Generation Systems (PEDG)*, pages 433–437, 2010.
- [136] A. K. Ziarani, A. Konrad, and A. N. Sinclair. A novel time-domain method of analysis of pulsed sine wave signals. *IEEE Trans. Instrum. Meas.*, 52(3):809–814, Jun. 2003.

## Appendix A

# PCB Layout

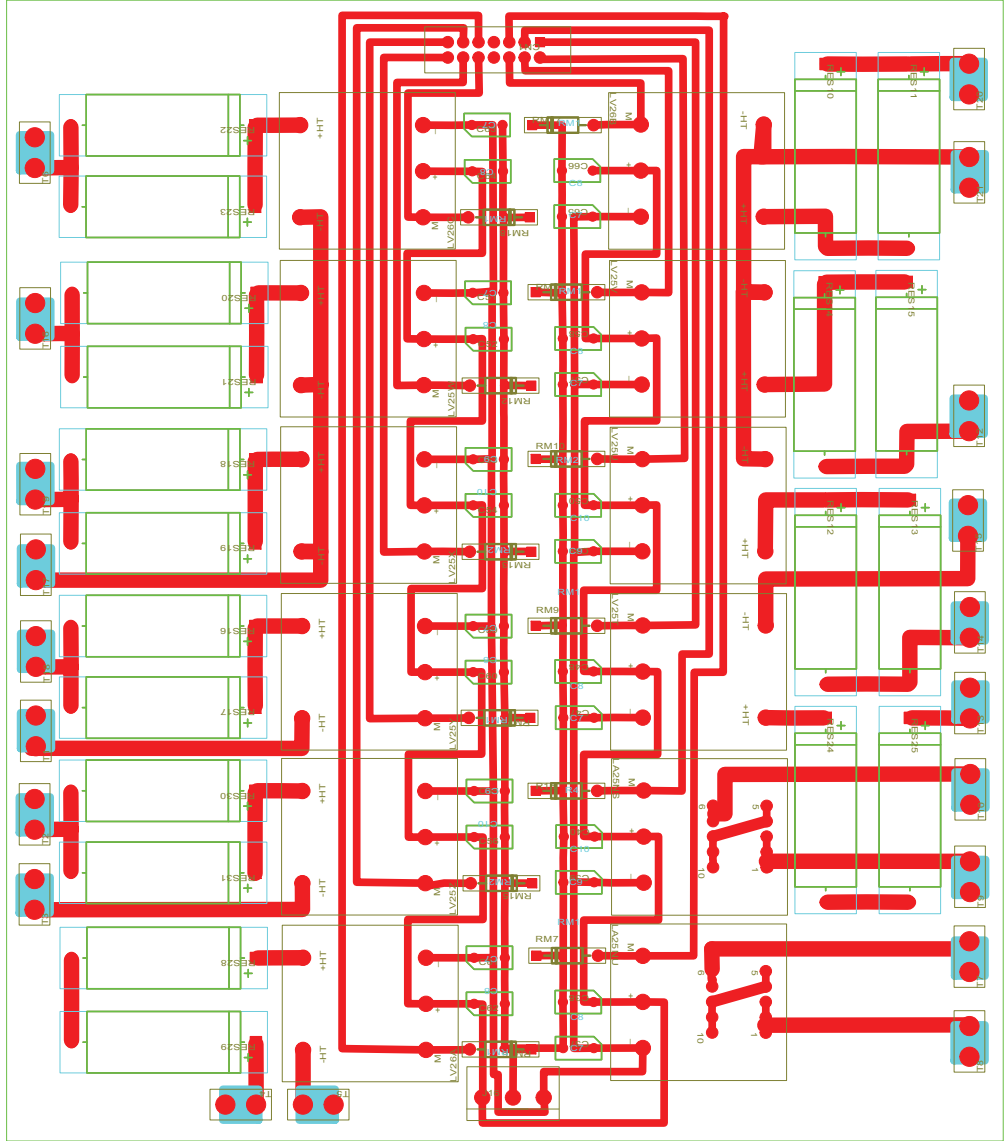


Figure A.1: The PCB layout of measurement transducers board



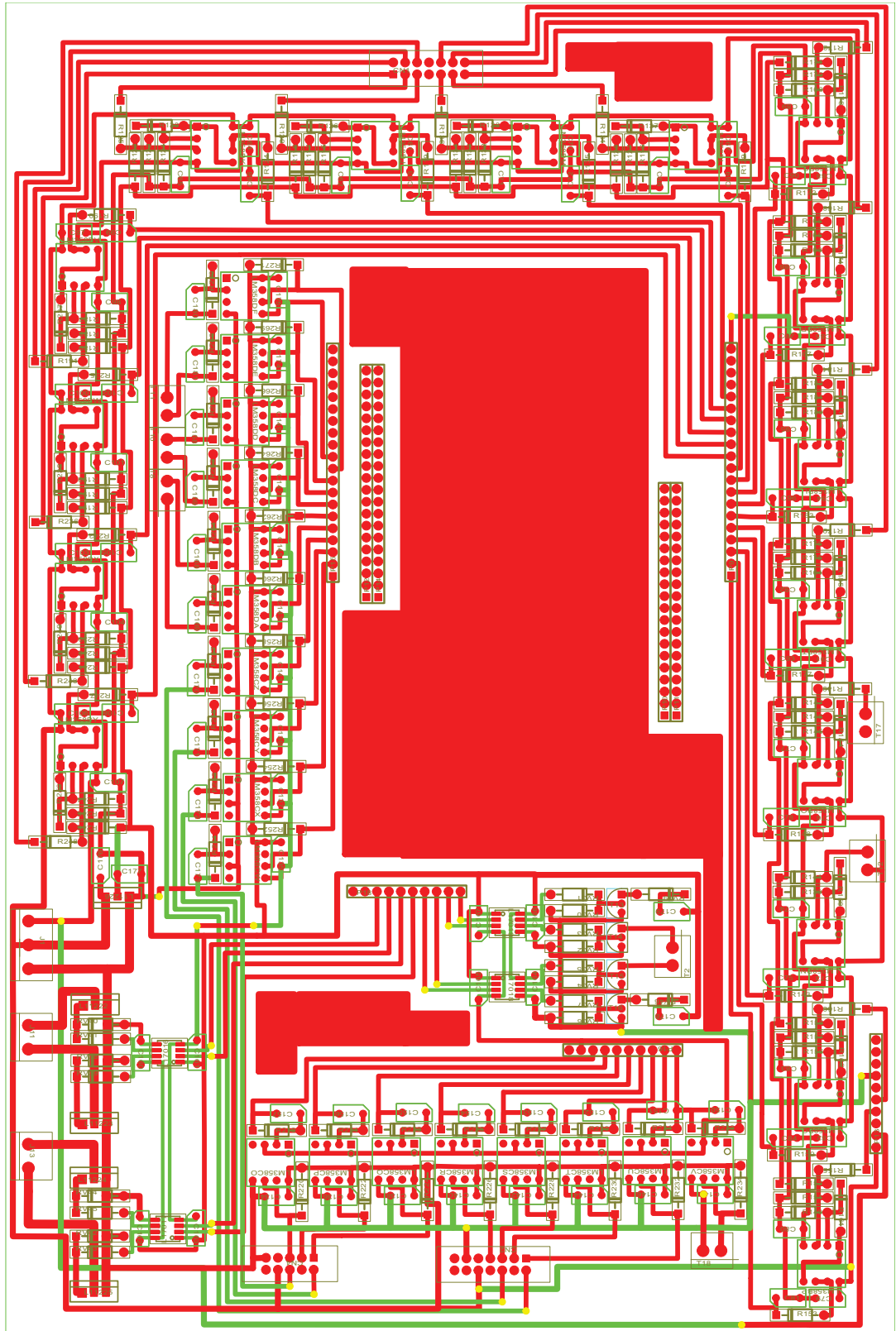
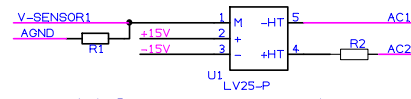


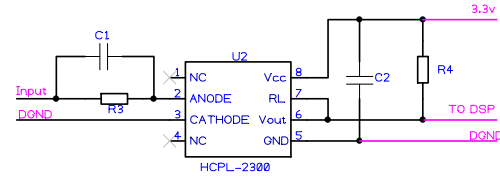
Figure A.2: The PCB layout of control board  
141

## Appendix B

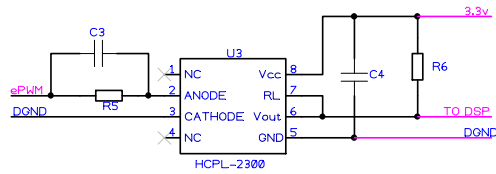
## Schematics



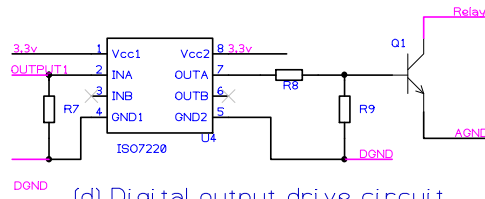
(a) Circuit of transducer



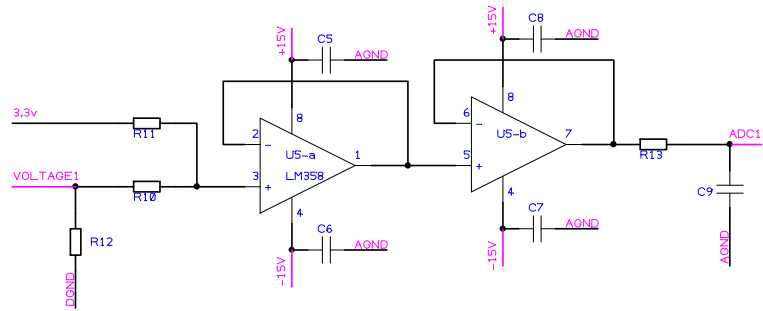
(b) Digital input drive circuit



(c) PWM drive circuit



(d) Digital output drive circuit



(e) ADC circuit

Figure B.1: Schematics

## Appendix C

# Matlab Code

DigitalInputGUI.m

```
function varargout = DigitalInputGUI(varargin)
    gui_Singleton = 1;
    gui_State = struct('gui_Name', mfilename, ...
        'gui_Singleton', gui_Singleton, ...
        'gui_OpeningFcn', @DigitalInputGUI_OpeningFcn, ...
        'gui_OutputFcn', @DigitalInputGUI_OutputFcn, ...
        'gui_LayoutFcn', [] , ...
        'gui_Callback', []);
    if nargin && ischar(varargin{1})
        gui_State.gui_Callback = str2func(varargin{1});
    end
    if nargout
        [varargout{1:nargout}] = gui_mainfcn(gui_State, varargin{:});
    else
        gui_mainfcn(gui_State, varargin{:});
    end
    function DigitalInputGUI_OpeningFcn(hObject, eventdata, handles, varargin)
        handles.output = hObject;
        guidata(hObject, handles);
        global cc;
        [cc, err] = PrepareTargetandLoad (handles);
        if err == 1
```

```

return
end
configure(cc.rtdx,1024,8);
open(cc.rtdx,'DigIn0','r');
open(cc.rtdx,'DigIn1','r');
open(cc.rtdx,'DigIn2','r');
open(cc.rtdx,'DigIn3','r');
open(cc.rtdx,'DigIn4','r');
open(cc.rtdx,'DigIn5','r');
open(cc.rtdx,'DigIn6','r');
open(cc.rtdx,'DigIn7','r');
enable(cc.rtdx,'DigIn0');
enable(cc.rtdx,'DigIn1');
enable(cc.rtdx,'DigIn2');
enable(cc.rtdx,'DigIn3');
enable(cc.rtdx,'DigIn4');
enable(cc.rtdx,'DigIn5');
enable(cc.rtdx,'DigIn6');
enable(cc.rtdx,'DigIn7');
enable(cc.rtdx);
cc.rtdx
run(cc);
r = cc.rtdx;
t0 = r.readmsg('DigIn0', 'double');
set(handles.input0, 'string', num2str(t0));
t1 = r.readmsg('DigIn1', 'double');
set(handles.input1, 'string', num2str(t1));
t2 = r.readmsg('DigIn2', 'double');
set(handles.input2, 'string', num2str(t2));
t3 = r.readmsg('DigIn3', 'double');
set(handles.input3, 'string', num2str(t3));
t4 = r.readmsg('DigIn4', 'double');
set(handles.input4, 'string', num2str(t4));
t5 = r.readmsg('DigIn5', 'double');

```

```

set(handles.input5, 'string', num2str(t5));
t6 = r.readmsg('DigIn6', 'double');
set(handles.input6, 'string', num2str(t6));
t7 = r.readmsg('DigIn7', 'double');
set(handles.input7, 'string', num2str(t7));
set(handles.figure1,'visible','on');
while(isenabled(cc.rtdx))
pause(0.5);
numMsgs0 = r.msgcount('DigIn0');
if (numMsgs0 > 0),
if (numMsgs0 > 1),
r.flush('DigIn0',numMsgs0-1);
end
t0 = r.readmsg('DigIn0', 'double');
end
set(handles.input0, 'string', num2str(t0));
numMsgs1 = r.msgcount('DigIn1');
if (numMsgs1 > 0),
if (numMsgs1 > 1),
r.flush('DigIn1',numMsgs1-1);
end
t1 = r.readmsg('DigIn1', 'double');
end
set(handles.input1, 'string', num2str(t1));
numMsgs2 = r.msgcount('DigIn2');
if (numMsgs2 > 0),
if (numMsgs2 > 1),
r.flush('DigIn2',numMsgs2-1);
end
t2 = r.readmsg('DigIn2', 'double');
end
set(handles.input2, 'string', num2str(t2));
numMsgs3 = r.msgcount('DigIn3');
if (numMsgs3 > 0),

```

```

if (numMsgs3 > 1),
r.flush('DigIn3',numMsgs3-1);
end
t3 = r.readmsg('DigIn3', 'double');
end
set(handles.input3, 'string', num2str(t3));
numMsgs4 = r.msgcount('DigIn4');
if (numMsgs4 > 0),
if (numMsgs4 > 1),
r.flush('DigIn4',numMsgs4-1);
end
t4 = r.readmsg('DigIn4', 'double');
end
set(handles.input4, 'string', num2str(t4));
numMsgs5 = r.msgcount('DigIn5');
if (numMsgs5 > 0),
if (numMsgs5 > 1),
r.flush('DigIn5',numMsgs5-1);
end
t5 = r.readmsg('DigIn5', 'double');
end
set(handles.input5, 'string', num2str(t5));
numMsgs6 = r.msgcount('DigIn6');
if (numMsgs6 > 0),
if (numMsgs6 > 1),
r.flush('DigIn6',numMsgs6-1);
end
t6 = r.readmsg('DigIn6', 'double');
end
set(handles.input6, 'string', num2str(t6));
numMsgs7 = r.msgcount('DigIn7');
if (numMsgs7 > 0),
if (numMsgs7 > 1),
r.flush('DigIn7',numMsgs7-1);

```

```

end
t7 = r.readmsg('DigIn7', 'double');
end
set(handles.input7, 'string', num2str(t7));
pause(0.5);
if ~isrunning(cc)
    Close_Callback(hObject, eventdata, handles);
end
end
if ishandle(hObject)
    guidata(hObject, handles);
end
function [cc, err] = PrepareTargetandLoad(handles)
try
    modelName = gcs;
    cc = connectToBoard(modelName);
    cc.visible(1);
    if ~cc.isrtDXcapable
        disp('Ending demo...');
    if ishandle(handles.figure1)
        close(handles.figure1)
    end
    msg = lf_message('demos:RTDXNotSupported');
    errordlg(msg, 'Error');
    err = 1;
    return
end
fullModelName = fullfile('.', [modelName '_ccslink'], modelName);
cc.cd(fullfile(pwd,[modelName '_ccslink']));
outFile = [modelName '.out'];
if exist([fullModelName '.out'])
    try
        cc.reset;pause(0.1);
        cc.load(outFile,100);
    end
end

```



```

catch
clear cc;
msg = lf_message('demos:runDemoLoadError');
errordlg(msg, 'Error');
err = 1;
return
end
else
msg = lf_message('demos:runDemoReBuildError');
errordlg(msg, 'Error' , 'modal');
err = 1;
return
end
err = 0;
catch ME
err = 1;
errordlg(ME.message, 'Error');
end
function varargout = DigitalInputGUI_OutputFcn(hObject, eventdata, handles)
varargout{1} = handles.output;
function input0_Callback(hObject, eventdata, handles)
function input0_CreateFcn(hObject, eventdata, handles)
if ispc && isequal(get(hObject,'BackgroundColor'),
get(0,'defaultUicontrolBackgroundColor'))
set(hObject,'BackgroundColor','white');
end
function input1_Callback(hObject, eventdata, handles)
function input1_CreateFcn(hObject, eventdata, handles)
if ispc && isequal(get(hObject,'BackgroundColor'),
get(0,'defaultUicontrolBackgroundColor'))
set(hObject,'BackgroundColor','white');
end
function input2_Callback(hObject, eventdata, handles)
function input2_CreateFcn(hObject, eventdata, handles)

```

```

if ispc && isequal(get(hObject,'BackgroundColor'),
get(0,'defaultUicontrolBackgroundColor'))
set(hObject,'BackgroundColor','white');
end
function input3_Callback(hObject, eventdata, handles)
function input3_CreateFcn(hObject, eventdata, handles)
if ispc && isequal(get(hObject,'BackgroundColor'),
get(0,'defaultUicontrolBackgroundColor'))
set(hObject,'BackgroundColor','white');
end
function input4_Callback(hObject, eventdata, handles)
function input4_CreateFcn(hObject, eventdata, handles)
if ispc && isequal(get(hObject,'BackgroundColor'),
get(0,'defaultUicontrolBackgroundColor'))
set(hObject,'BackgroundColor','white');
end
function input5_Callback(hObject, eventdata, handles)
function input5_CreateFcn(hObject, eventdata, handles)
if ispc && isequal(get(hObject,'BackgroundColor'),
get(0,'defaultUicontrolBackgroundColor'))
set(hObject,'BackgroundColor','white');
end
function input6_Callback(hObject, eventdata, handles)
function input6_CreateFcn(hObject, eventdata, handles)
if ispc && isequal(get(hObject,'BackgroundColor'),
get(0,'defaultUicontrolBackgroundColor'))
set(hObject,'BackgroundColor','white');
end
function input7_Callback(hObject, eventdata, handles)
function input7_CreateFcn(hObject, eventdata, handles)
if ispc && isequal(get(hObject,'BackgroundColor'),
get(0,'defaultUicontrolBackgroundColor'))
set(hObject,'BackgroundColor','white');
end

```

```

function Close_Callback(hObject, eventdata, handles)
disp('Ending demo...');
global cc;
r = cc.rtdx;
try
r.disable('DigIn0');
r.disable('DigIn1');
r.disable('DigIn2');
r.disable('DigIn3');
r.disable('DigIn4');
r.disable('DigIn5');
r.disable('DigIn6');
r.disable('DigIn7');
r.disable;
catch
end
cc.reset;
if ishandle(handles.figure1)
close(handles.figure1)
end
outputtest_all.m
function varargout = outputtest_all(varargin)
gui_Singleton = 1;
gui_State = struct('gui_Name', mfilename, ...
'gui_Singleton', gui_Singleton, ...
'gui_OpeningFcn', @outputtest_all_OpeningFcn, ...
'gui_OutputFcn', @outputtest_all_OutputFcn, ...
'gui_LayoutFcn', [] , ...
'gui_Callback', []);
if nargin && ischar(varargin{1})
gui_State.gui_Callback = str2func(varargin{1});
end
if nargin
[varargout{1:nargout}] = gui_mainfcn(gui_State, varargin{:});

```

```

else
gui_mainfcn(gui_State, varargin{:});
end
function outputtest_all_OpeningFcn(hObject, eventdata, handles, varargin)
handles.output = hObject;
guidata(hObject, handles);
global cc;
[cc, err] = PrepareTargetandLoad (handles);
if err == 1
return
end
configure(cc.rtdx,1024,8);
open(cc.rtdx,'input0','w');
open(cc.rtdx,'input1','w');
open(cc.rtdx,'input2','w');
open(cc.rtdx,'input3','w');
open(cc.rtdx,'input4','w');
open(cc.rtdx,'input5','w');
open(cc.rtdx,'input6','w');
open(cc.rtdx,'input7','w');
enable(cc.rtdx,'input0');
enable(cc.rtdx,'input1');
enable(cc.rtdx,'input2');
enable(cc.rtdx,'input3');
enable(cc.rtdx,'input4');
enable(cc.rtdx,'input5');
enable(cc.rtdx,'input6');
enable(cc.rtdx,'input7');
enable(cc.rtdx);
cc.rtdx
run(cc);
writemsg(cc.rtdx, 'input0', int16(0));
set(handles.IO12, 'string', num2str(0));
writemsg(cc.rtdx, 'input1', int16(0));

```

```

set(handles.IO13, 'string', num2str(0));
writemsg(cc.rtdx, 'input2', int16(0));
set(handles.IO14, 'string', num2str(0));
writemsg(cc.rtdx, 'input3', int16(0));
set(handles.IO15, 'string', num2str(0));
writemsg(cc.rtdx, 'input4', int16(0));
set(handles.IO16, 'string', num2str(0));
writemsg(cc.rtdx, 'input5', int16(0));
set(handles.IO17, 'string', num2str(0));
writemsg(cc.rtdx, 'input6', int16(0));
set(handles.IO18, 'string', num2str(0));
writemsg(cc.rtdx, 'input7', int16(0));
set(handles.IO19, 'string', num2str(0));
function [cc, err] = PrepareTargetandLoad(handles)
try
modelName = gcs;
cc = connectToBoard(modelName);
cc.visible(1);
if ~cc.isrtdxcapable
disp('Ending demo...');
if ishandle(handles.figure1)
close(handles.figure1)
end
msg = lf_message('demos:RTDXNotSupported');
errordlg(msg, 'Error');
err = 1;
return
end
fullModelName = fullfile('.', [modelName '_ccslink'], modelName);
cc.cd(fullfile(pwd,[modelName '_ccslink']));
outFile = [modelName '.out'];
if exist([fullModelName '.out'])
try
cc.reset;pause(0.1);

```

```

cc.load(outFile,100);
catch
clear cc;
msg = lf_message('demos:runDemoLoadError');
errordlg(msg, 'Error');
err = 1;
return
end
else
msg = lf_message('demos:runDemoReBuildError');
errordlg(msg, 'Error' , 'modal');
err = 1;
return
end
err = 0;
catch ME
err = 1;
errordlg(ME.message, 'Error');
end
function varargout = outputtest_all_OutputFcn(hObject, eventdata, handles)
varargout{1} = handles.output;
function IO12_Callback(hObject, eventdata, handles)
function IO12_CreateFcn(hObject, eventdata, handles)
if ispc && isequal(get(hObject,'BackgroundColor'),
get(0,'defaultUicontrolBackgroundColor'))
set(hObject,'BackgroundColor','white');
end
function IO13_Callback(hObject, eventdata, handles)
function IO13_CreateFcn(hObject, eventdata, handles)
if ispc && isequal(get(hObject,'BackgroundColor'),
get(0,'defaultUicontrolBackgroundColor'))
set(hObject,'BackgroundColor','white');
end
function IO14_Callback(hObject, eventdata, handles)

```

```

function IO14_CreateFcn(hObject, eventdata, handles)
if ispc && isequal(get(hObject,'BackgroundColor'),
get(0,'defaultUicontrolBackgroundColor'))
set(hObject,'BackgroundColor','white');
end
function IO15_Callback(hObject, eventdata, handles)
function IO15_CreateFcn(hObject, eventdata, handles)
if ispc && isequal(get(hObject,'BackgroundColor'),
get(0,'defaultUicontrolBackgroundColor'))
set(hObject,'BackgroundColor','white');
end
function IO16_Callback(hObject, eventdata, handles)
function IO16_CreateFcn(hObject, eventdata, handles)
if ispc && isequal(get(hObject,'BackgroundColor'),
get(0,'defaultUicontrolBackgroundColor'))
set(hObject,'BackgroundColor','white');
end
function IO17_Callback(hObject, eventdata, handles)
function IO17_CreateFcn(hObject, eventdata, handles)
if ispc && isequal(get(hObject,'BackgroundColor'),
get(0,'defaultUicontrolBackgroundColor'))
set(hObject,'BackgroundColor','white');
end
function IO18_Callback(hObject, eventdata, handles)
function IO18_CreateFcn(hObject, eventdata, handles)
if ispc && isequal(get(hObject,'BackgroundColor'),
get(0,'defaultUicontrolBackgroundColor'))
set(hObject,'BackgroundColor','white');
end
function IO19_Callback(hObject, eventdata, handles)
function IO19_CreateFcn(hObject, eventdata, handles)
if ispc && isequal(get(hObject,'BackgroundColor'),
get(0,'defaultUicontrolBackgroundColor'))
set(hObject,'BackgroundColor','white');

```

```

end
function IO12_0_Callback(hObject, eventdata, handles)
global cc;
r = cc.rtdx;
r.writemsg('input0', int16(0));
set(handles.IO12, 'string', num2str(0));
function IO13_0_Callback(hObject, eventdata, handles)
global cc;
r = cc.rtdx;
r.writemsg('input1', int16(0));
set(handles.IO13, 'string', num2str(0));
function IO14_0_Callback(hObject, eventdata, handles)
global cc;
r = cc.rtdx;
r.writemsg('input2', int16(0));
set(handles.IO14, 'string', num2str(0));
function IO15_0_Callback(hObject, eventdata, handles)
global cc;
r = cc.rtdx;
r.writemsg('input3', int16(0));
set(handles.IO15, 'string', num2str(0));
function IO16_0_Callback(hObject, eventdata, handles)
global cc;
r = cc.rtdx;
r.writemsg('input4', int16(0));
set(handles.IO16, 'string', num2str(0));
function IO17_0_Callback(hObject, eventdata, handles)
global cc;
r = cc.rtdx;
r.writemsg('input5', int16(0));
set(handles.IO17, 'string', num2str(0));
function IO18_0_Callback(hObject, eventdata, handles)
global cc;
r = cc.rtdx;

```



```

r.writemsg('input6', int16(0));
set(handles.IO18, 'string', num2str(0));
function IO19_0_Callback(hObject, eventdata, handles)
global cc;
r = cc.rtdx;
r.writemsg('input7', int16(0));
set(handles.IO19, 'string', num2str(0));
function IO12_1_Callback(hObject, eventdata, handles)
global cc;
r = cc.rtdx;
r.writemsg('input0', int16(1));
set(handles.IO12, 'string', num2str(1));
function IO13_1_Callback(hObject, eventdata, handles)
global cc;
r = cc.rtdx;
r.writemsg('input1', int16(1));
set(handles.IO13, 'string', num2str(1));
function IO14_1_Callback(hObject, eventdata, handles)
global cc;
r = cc.rtdx;
r.writemsg('input2', int16(1));
set(handles.IO14, 'string', num2str(1));
function IO15_1_Callback(hObject, eventdata, handles)
global cc;
r = cc.rtdx;
r.writemsg('input3', int16(1));
set(handles.IO15, 'string', num2str(1));
function IO16_1_Callback(hObject, eventdata, handles)
global cc;
r = cc.rtdx;
r.writemsg('input4', int16(1));
set(handles.IO16, 'string', num2str(1));
function IO17_1_Callback(hObject, eventdata, handles)
global cc;

```

```

r = cc.rtdx;
r.writemsg('input5', int16(1));
set(handles.IO17, 'string', num2str(1));
function IO18_1_Callback(hObject, eventdata, handles)
global cc;
r = cc.rtdx;
r.writemsg('input6', int16(1));
set(handles.IO18, 'string', num2str(1));
function IO19_1_Callback(hObject, eventdata, handles)
global cc;
r = cc.rtdx;
r.writemsg('input7', int16(1));
set(handles.IO19, 'string', num2str(1));
function Close_Callback(hObject, eventdata, handles)
disp('Ending demo...');
global cc;
r = cc.rtdx;
try
r.disable('input0');
r.disable('input1');
r.disable('input2');
r.disable('input3');
r.disable('input4');
r.disable('input5');
r.disable('input6');
r.disable('input7');
r.disable;
catch
end
cc.reset;
if ishandle(handles.figure1)
close(handles.figure1)
end

```